Defect related transport mechanism in the resistive switching materials $SrTiO_3$ and NbO_2

DISSERTATION

zur Erlangung des akademischen Grades

doctor rerum naturalium
(Dr. rer. nat.)

im Promotionsfach Physik
Spezialisierung: Experimentalphysik

eingereicht an der
Mathematisch-Naturwissenschaftlichen Fakultät
der Humboldt-Universität zu Berlin

von

M.Sc. Julian Stöver

Präsidentin der Humboldt-Universität zu Berlin:
Prof. Dr.-Ing. Dr. Sabine Kunst

Dekan der Mathematisch-Naturwissenschaftlichen Fakultät:
Prof. Dr. Elmar Kulke

Gutachter:	1. Prof. W. Ted Masselink
	2. Prof. Dr. Thomas Schröder
	3. Prof. Josep Fontcuberta
Tag der mündlichen Prüfung:	16.07.2021

ABSTRACT

In this work, the impact of crystal defects on the resistive switching materials $SrTiO_3$ and NbO_2 is investigated. The work is divided into two parts.

In the first part, NbO_2 (001) thin films are studied. NbO_2 is a material that exhibits an insulator-metal transition, which can be induced thermally at 1080 K, or by external electric fields at room-temperature. So far, resistivities measured for NbO_2 thin films in the insulating phase are by a factor of 200 lower than the 10 kΩ cm resistivity measured in NbO_2 single crystals. To make this material applicable for resistive switching, the resistivity in the insulating phase has to be increased to effectively block the current in the high resistive state.

Throughout the investigations presented in this work, the resistivity of NbO_2 thin films is increased to 945 Ω cm. For this, the NbO_2 is annealed at 880 °C after epitaxial growth, increasing the grain diameter by a factor of 10 to 60 nm. It is shown that conductive percolation paths along the grain boundaries are responsible for the decrease in resistivity. Temperature-dependent conductivity measurements identified defect states responsible for the reduction in resistivity from the theoretical value. At temperatures above 650 K, the intrinsic conductivity of the thin film is demonstrated and a band gap of 0.88 eV is determined. Absorption spectroscopy and spectroscopic ellipsometry are also used to determine an optical band gap of 0.76 eV at room temperature.

In the second part of this work, the influence of the Ti antisite defect on resistive switching in $SrTiO_3$ thin films grown by metal-organic vapor phase epitaxy is studied. Both stoichiometric and strontium deficient thin films are studied. It is shown via temperature-dependent permittivity measurements that crystal defects harden the soft phonon mode and polar nano regions are formed in highly strontium deficient films, which was attributed to the formation of Ti antisite defects. In addition, highly strontium deficient $SrTiO_3$ films are shown to exhibit stable resistive switching with an on-off ratio of 2×10^7 at 10 K, whereas stoichiometric thin-films do not show stable switching. A diode-like transport mechanism based on Schottky emission in the high-resistance state and dominated by defect-assisted tunneling current in the low-resistance state is identified. From this, a new model for resistive switching based on the Ti antisite defect and the induced ferroelectricity is developed. The polarization charge at the interface between the substrate and thin film creates or suppresses a space charge region, which blocks or allows current transport, respectively.

ZUSAMMENFASSUNG

In dieser Arbeit wird der Einfluss von Kristalldefekten auf das resistive Schalten der Materialien $SrTiO_3$ und NbO_2 untersucht. Die Arbeit gliedert sich in zwei Teile.
Im ersten Teil werden NbO_2 (001)-Dünnschichten untersucht. NbO_2 ist ein Material, das einen Isolator-Metall-Übergang aufweist, der thermisch bei 1080 K oder durch externe elektrische Felder bei Raumtemperatur induziert werden kann. Bisher sind die für NbO_2-Dünnschichten in der isolierenden Phase gemessenen spezifische Widerstände um einen Faktor von 200 niedriger als der in NbO_2-Einkristallen gemessene 10 kΩ cm-Widerstand. Um dieses Material für das resistive Schalten einsetzbar zu machen, muss der spezifische Widerstand in der isolierenden Phase erhöht werden, um den Strom im hochohmigen Zustand effektiv zu blockieren.
In diesr Arbeit wird der spezifische Widerstand von NbO_2-Dünnschichten auf 945 Ω cm erhöht. Dazu wird das NbO_2 nach dem epitaktischen Wachstum bei 880 °C ausgeheizt, wodurch der Korndurchmesser um einen Faktor von 10 auf 60 nm erhöht wird. Es wird gezeigt, dass leitfähige Perkolationspfade entlang der Korngrenzen für die Abnahme des spezifischen Widerstandes verantwortlich sind. Durch temperaturabhängige Leitfähigkeitsmessungen wurden Defektzustände identifiziert, die für die Verringerung des spezifischen Widerstandes gegenüber dem theoretischen Wert verantwortlich sind. Bei Temperaturen oberhalb von 650 K wird die intrinsische Leitfähigkeit der Dünnschicht nachgewiesen und eine Bandlücke von 0.88 eV bestimmt. Mittels Absorptionsspektroskopie und spektroskopischer Ellipsometrie wird zudem eine optische Bandlücke von 0.76 eV bei Raumtemperatur ermittelt.
Im zweiten Teil wird der Einfluss des Ti-Antisite Defekts auf das resistive Schalten in $SrTiO_3$ Dünnschichten untersucht, welche mit metallorganischer Dampfphasenepitaxie gezüchtet wurden. Dabei werden sowohl stoichiometrische als auch Strontium defizitäre Schichten untersucht. Es wird über temperaturabhängige Permittivitätsmessungen gezeigt, dass durch Kristalldefekte die weiche Phononenmode gestört wird und bei stark strontiumverarmten Schichten polare Nanoregionen gebildet werden, was auf die Bildung des Ti_{Sr} Defekts zurückgeführt wurde. Darüber hinaus wird gezeigt, dass stark strontiumdefiziente $SrTiO_3$-Schichten ein stabiles resistives Schalten mit einem Ein-Aus-Verhältnis von 2×10^7 bei 10 K aufweisen, während stöchiometrische Dünnschichten kein stabiles Schalten zeigen. Es wird ein diodenartiger Transportmechanismus, der im hochohmigen Zustand auf Schottkyemission beruht und ihm niederohmigen Zustand durch defektassistierten Tunnelstrom dominiert wird, identifiziert. Daraus wurde ein neues Modell für das resistive Schalten, basierend auf dem Ti_{Sr} Defekt und der induzierten Ferroelektrizität, entwickelt. Durch die Polarisationsladung an der Grenzschicht zwischen Substrat und Dünnschicht wird eine Raumladungszone erzeugt oder unterdrückt, die den Stromtransport entsprechend sperrt oder erlaubt.

CONTENTS

1 INTRODUCTION 1

2 THEORETICAL BACKGROUND 5

2.1 Electrical transport models . . . 5

2.2 Dielectricity, Polariztation and Ferroelectricity . . . 10

2.2.1 Dielectricity . . . 10

2.2.2 Ferroelectricity . . . 11

2.2.3 Relaxor and Polar Nano Regions . . . 12

2.3 Resistive switching . . . 13

3 EXPERIMENTAL METHODS 17

3.1 Resistivity and Hall-effect . . . 17

3.1.1 Room-temperature measurements . . . 17

3.1.2 Temperature dependent measurements . . . 19

3.2 Metal-Insulator-Semiconductor and Schottky devices . . . 20

3.2.1 Electrical contact preparation . . . 20

3.2.2 Current-voltage measurements . . . 21

3.2.3 Capacitance voltage measurements . . . 21

3.3 Optical Absorption Spectroscopy . . . 22

4 NIOBIUM DIOXIDE 25

4.1 Basic Properties . . . 26

4.2 Structural properties of epitaxial layers . . . 28

4.2.1 Epitaxy of $NbO_2(001)$ on MgF_2 . . . 28

4.2.2 Grain properties of annealed NbO_2 layers . . . 31

4.3 Conductivity in NbO_2 epitaxial layer . . . 34

4.3.1 Resistivity of as-grown and annealed layers on MgF_2 substrates . . . 34

4.3.2 Temperature dependent resistivity measurements . . . 36

4.3.3 Percolation model for conductivity in NbO_2 . . . 38

4.4 Optical band gap determination . . . 39

4.4.1 Spectroscopic Ellipsometry . . . 39

4.4.2 Absorption spectroscopy . . . 41

4.5 Conclusion . . . 43

5 STRONTIUM TITANATE 45

5.1 Thin films grown by metal-organic vapor phase epitaxy . . . 46

5.2 Experimental characterization of the permittivity . . . 51

5.2.1 Bulk single crystals . . . 54

5.2.2 Permittivity in thick PLD grown $SrTiO_3$ layers . . . 56

5.2.3 MOVPE grown $SrTiO_3$ thin films . . . 62

5.2.4 Summary . . . 66

5.3 Experimental characterization of resistive switching . . . 67

5.3.1 Hysteresis curves 67
5.3.2 Threshold voltage and gradual switching 70
5.3.3 Impact of Strontium deficiency 77
5.3.4 Summary 80
5.4 Resistive switching model based on the Ti_{Sr} antisite defect . . . 81
5.4.1 Established models from literature 82
5.4.2 Model of the electrical transport 88
5.4.3 Conclusion 91
6 SUMMARY AND OUTLOOK 95
7 BIBLIOGRAPHY 99

Appendix

A LIST OF FIGURES 119
B LIST OF TABLES 127
C PUBLICATIONS 129
D ACKNOWLEDGMENTS 131
E STATEMENT OF AUTHORSHIP / SELBSTSTÄNDIGKEITSERKLÄRUNG 133

1 INTRODUCTION

Storing a bit in a computer takes an incredibly small amount of energy. Using a conventional, magnetic hard-disk drive (HDD), it takes only 1.5 nJ[46,94] to store the information. Modern solid-state drives (SSD), which are storing the information as a charge, need less than 1 nJ.[48,94] However, the unbroken growth of computing infrastructure makes these tiny amounts of energy highly relevant for our environment.

The total energy consumed by data centers in the USA was 70 TW h in 2014, which was 4 % of the total consumption of electricity. 11 % of this is used for storage technology.[162] That corresponds to 33 ZB (zeta byte) of data in 2018 and is expected to grow to 175 ZB in 2025.[146] In view of climate change and the desire for more efficient technologies, it is demanded to develop new storage technologies. This would additionally lead to significant cost reduction in one very central aspect of modern economies. Such technology must show advances on many aspects. Of course the energy required for writing and reading information should be less than existing technologies. But also the read/write cycles and the data retention time are important parameter that need to be tackled by the new technologies.. The switching speed is important to cope with the ever faster computing and larger data volumes and to provide functionality for non-volatile random access memories (RAM). And finally, the compatibility with existing (CMOS) technology would be an accelerating factor for establishing new storage technology in data centers and personal computer.

Different approaches are in development to achieves these goals: data storage based on ferroelectric polarization (FeRAM[108]), a phase-change in crystalline phase (PCRAM[144]), or by switching the magnetization of a magnetic thin film (MRAM[173]). Another method is a storage based on valence change, for which dopants are moved in an insulating layer, making it either insulating or conductive (ReRAM). All of these methods have in common, that reading the status of the storage cell is not anymore based on magnetization or charge, but on measuring a current flow through the cell (and thus the resistivity).

Reading and writing data in modern HDDs is in the range of milliseconds, for SSDs in the range of microseconds. ReRAMs provides reading and writing latencies in the nanosecond range.[183] In ReRAM devices, reading and writing is done by using a low readout voltage or a higher writing voltage and storage cells can

be driven in a two terminal setup (e.g. SSD storage uses three terminal cells). This allows the usage of crossbar arrays. In such setup, each node of the crossbar is a memristive cell, which connects the word and the bit line. This reduces the complexity of the device and provides excellent scalability down to the 10 nm range for the cell size.[149] The energy used for a reading operation can be in the pico joule region.[122]

Therefore, a tremendous effort has been made to develop and investigate suitable materials for ReRAM devices. ReRAM devices show resistive switching, which is the change of resistivity state controlled by electric fields. After demonstration of resistive switching in amorphous semiconductors[40], polymers[89] and ZnSe–Ge hetero-structures,[70] $SrTiO_3$ was established as a prototype material for resistive switching.[11] The underlying mechanism was described with the formation of filaments, which are formed by a voltage pulse due to electrical breakdown. The size of the filament can be controlled by electric fields and the ion motion is supported by Joule heating up to several hundred degree Celsius. But also alternative models for resistive switching in $SrTiO_3$ were developed, e.g. an electronic mechnaism, which is based on the charging and decharging of traps. Still, some inconsistencies exist in fully describing the switching mechanism.

The "voltage-time dilemma" is one of the open questions to be solved. It formulates the requirements for a resistive switching device. On the one hand, to provide storage functionality, the retention time should be very large. On the other hand, to be competitive, the switching voltages should be very low. These requirements are contrary to each other. In the example of an electronic mechanism with trapping and detrapping of charge carriers, the lifetime of the state depends on the barrier height. If it is low, the trap can easily be switched, but also the spontaneous detrapping would easily occur and thus, the storage ability would not be given.

Using the model of conductive filaments, the switching is based on ionic movement in the thin film. The localization of the ion is usually high under ambient conditions at room-temperature, thus the retention time is very high. On the other hand, the ions will not be very mobile in electric fields, thus the requirement of low switching voltages is not given. One approach was found towards overcoming this dilemma. Joule heating will increase the filament temperature up to several hundred degree Celsius, which increases the ionic movement in the electric field. But even this idea might fail in properly describing the resistive switching in $SrTiO_3$, ironically due to the high performance of the switching mechanism. The reason for this effect is the incredibly high switching speed. The switching speed was found to be in the nanosecond range.[208]. On this time scale, electronic processes

will be more likely and the speed of the thermal heating is slower than the switching. Therefore, it is desirable to elaborate alternative models or expand the existing ones.

To address this goal, high quality crystals are needed, which are investigated for their properties, in particular defects, to be able to bring further aspects in the association with resistive switching. This project, which is part of the Leibniz GraFOx Science Campus[60], aims for the growth of $SrTiO_3$ thin films by metal-organic vapor phase epitaxy, which is a process close to thermodynamic equilibrium and thus can provide good crystalline quality, as well as enabling the possibility to control the growth precisely by adjusting parameters like pressure, temperature or precursor flows. By doing this, defects can be intentionally introduced into the thin film, e.g. by deviating from the stoichiometry of $SrTiO_3$. The crystals are then characterized by a variety of analytical methods, e.g. x-ray diffraction and transmission electron microscopy. This work has the focus on the electrical characterization of the thin films. In combination with the defect analytics and the controlled growth of $SrTiO_3$ thin films, performed by collaborators, the present work establishes a defect based, ferroelectric resistive switching model by analyzing dielectric properties and resistive switching.

To benefit from the high switching performances of a ReRAM and to be able to scale the device size down to a few nanometers, crossbar arrays have to be used as a device layout. Crossbar devices differ e.g. from a CMOS devices in such way, that no active switching element, like a transistor, is needed to access and switch a cell. A cell in a crossbar devices is the node, interconnecting the bit and the word line. However, such simple device layout would lead to current sneak paths over neighboring nodes, since no switch or transistor is blocking the current through other cells. Already an array of 10 by 10 nodes would lead to a dissipated energy of 99 %, leading to a low energy efficiency.

To reduce the sneak paths without using a transistor element, a second type of resistive switching material can be used, the threshold resistive switching device. The threshold switch is a device which is insulating below a certain switching voltage and conductive above. The conductive state is meta stable, which leads to switching back to the insulating state after reducing the voltage below the threshold. NbO_2 is a material providing this switching behavior due to its metal insulator phase transition. This phase transition can be induced by high temperatures on the one hand , on the other hand it was already shown, that also an electric field can trigger the transition from the insulating state to the conductive state.

So far, reports in literature have shown, that NbO_2 shows a low resistivity even in it's insulating phase, which is by a factor of 200[50,79,123,191] lower than the resistivity value of 10 kΩ cm shown

for NbO_2 bulk crystals.[75] Therefore, as a second part of the present work, material development were performed to reduce the residual conductivity of NbO_2 in its insulating phase by improving the epitaxial growth with pulsed laser deposition. The thin films were then characterized electrically and the band gap of the material was determined optically and electrically from this thin films.

The structure of the present work is to first introduce relevant models for the electrical and dielectric properties of the resistive switching materials. Afterwards, the principles of the main characterization methods are given. In the first results part, the investigation of NbO_2 thin films epitaxially grown on MgF_2 are discussed. The focus of this part is to show the influence of an annealing step on the resistivity of the thin films and to develop a model for the residual conduction through the films. Additionally, the band gap is determined electrically and optically, as there is still large variation of band gap values in literature reports.[2,98,125,150,197]

In the second part, thin films of $SrTiO_3$ grown by metal-organic vapor phase epitaxy are investigated. After giving an introduction of the growth and characterization performed by collaborators, the dielectric properties and the influence of defects on these properties is discussed. Afterwards, the resistive switching in these films is discussed and a defect based model is developed, unifying the dielectric and electrical measurement results.

2 THEORETICAL BACKGROUND

2.1 ELECTRICAL TRANSPORT MODELS

The introduction in the theory of transport models is mainly based on the textbooks Kittel[84] and Sze[170]. Parts which are based on other literature are marked accordingly.

Different mechanisms of charge carrier transport through an semiconductor exist and the dominant mechanism depends on the doping level, the thickness of the layer or defects, which form defect states within the band gap. The most simple is the ohmic law

$$\vec{J} = \sigma\vec{E} = nq\mu\vec{E}, \tag{2.1}$$

which is a scalar in isotropic media. The conductivity σ is dependent on the charge carriers and their mobility. In intrinsic semiconductors, the origin of conductivity is the generation and recombination of charge carriers, which in the average gives a intrinsic conductivity. The intrinsic conductivity can be derived from the law of mass action

$$n_i^2 = n_0 \cdot p_0. \tag{2.2}$$

The charge carrier concentration follows the thermal activation and thus the Boltzmann law

$$n_0 = N_C \cdot \exp\left(-\frac{E_C - E_F}{k_B T}\right) \tag{2.3}$$

$$p_0 = N_V \cdot \exp\left(-\frac{E_F - E_V}{k_B T}\right). \tag{2.4}$$

The resistivity ρ can then be calculated by

$$\rho = \frac{1}{\sigma} = \frac{1}{n_i q(\mu_e + \mu_p)} \tag{2.5}$$

In doped semiconductors, the resistivity can be derived from the charge neutrality equation

$$n_0 + N_A = p_0 + N_D. \tag{2.6}$$

In case of a n-type semiconductor, the donator concentration is exceeding the acceptor concentration ($N_D \gg N_A$) and the hole concentration is approximately zero ($p_0 \approx n_i^2/N_D \approx 0$), thus the charge neutrality equation becomes

$$n_0 = N_D - N_A. \tag{2.7}$$

J	Current density
E	Electric field
σ	Conductivity
n	Carrier concentration
μ	Carrier mobility
q	Elementary charge

n_0	Electrons concentration
p_0	Holes concentration
N_C	Density of states in conduction band
N_V	Density of states in valence band
E_x	Energy of the conduction band (C), valence band (V) or Fermi level (F)
μ_x	Electron (e) or hole (p) mobility

ρ	Resistivity
n_i	Intrinsic charge carrier concentration
N_x	Acceptor (A) or donator (D) concentration

In this case, the resistivity is

$$\rho = \frac{1}{n_0 q \mu_e}. \tag{2.8}$$

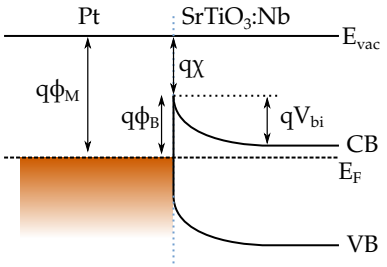

Figure 2.1: Band model of a Schottky diode for a n-type semiconductor (e.g. $SrTiO_3$). Adapted from reference [170].

So far, ideal contacts on the semiconductor sample were assumed, i.e. ohmic behavior, recombination at the contacts, and no carrier injection. Especially the interfaces have to be considered, since band bending can occur in that regions. But also tunneling currents and charge carrier emission from traps have to be considered.

In the case of a metal-semiconductor interface (figure 2.1), the difference in work function of the metal electrode ϕ_M and the electron affinity χ in the semiconductor leads to a band bending of the conduction and valence band at the interface. By applying an external field V to the interface, the barrier height ϕ_B will be $\phi_B = \phi_M - \chi + V$. The current transport through this barrier can be described using the thermionic emission model

$$J = A^{**} T^2 \exp\left(\frac{q}{k_B T}\left(\frac{V}{\eta} - \phi_B\right)\right). \tag{2.9}$$

A^{**}	Effective Richardson constant
k_B	Boltzmann constant
T	Temperature
ϕ_B	Metal-Semicondcutor barrier
η	Ideality factor
ϵ_0	Vacuum permittivity
ϵ_r	Relative permittivity

From the equation, it is obvious, that the device has a rectifying and a forward direction, thus this device is called Schottky diode. In case of $V/\eta > \phi_B$, the current increases exponentially. In the ideal case, η is 1, however, in a real device larger values can be obtained. This results in a reduced current in forward direction. Reasons for such non-ideal Schottky device can be e.g. insulating interface layers.

2.1.0.1 Schottky emission

If the interface layer is thick, the thermionic emission model is not a proper description of the device anymore, and models to describe a metal-insulator-semiconductor structure have to be used. The most simple one is the Schottky emission model.

If an electron is emitted from a metal surface, it has to overcome a potential due to an induced positive charge in the metal, which attracts the electron. The force is called image force with

$$F(x) = \frac{-q^2}{16\pi\epsilon_0\epsilon_r x^2}. \tag{2.10}$$

An externally applied electric field can lower the potential energy needed to overcome the image force, the so called image force lowering. The potential energy, after integrating the image force and the external field over the x-coordinate, is then

$$\phi = \frac{q^2}{16\pi\epsilon_0\epsilon_r x} + qEx. \tag{2.11}$$

The potential is lowered in its maximum ($d\phi/dx = 0$) by the value $\Delta\phi$, which is

$$\Delta\phi = \sqrt{\frac{qE}{4\pi\epsilon_0\epsilon_r}} \tag{2.12}$$

In the case of a metal-semiconductor interface, the external field E is the field strength at the interface. The permittivity of the dielectric can deviate from the static permittivity, if the transmission time for the charge carrier is faster than the relaxation time of the polarization in the dielectric. To calculate the current by Schottky emission through the insulating layer, the potential can be then used in the Richardson law[21,43], resulting in the Schottky emission formular

$$J = A^{**}T^2 \exp\left(\frac{q}{k_B T}\left(\sqrt{\frac{qE}{4\pi\epsilon_0\epsilon_r}} - \phi_B\right)\right). \tag{2.13}$$

2.1.0.2 Poole-Frenkel emission

Whereas the Schottky emission depends on the metal-insulator interface, the Poole-Frenkel model also considers the bulk of the material[206]. Defects in the insulator can form trap levels in the band gap. A charge carrier trapped into the defect will have to overcome the potential ϕ_T, which is the depth of the trap measured from the conduction band. Again, an external field will influence the shape of the potential, but in this case it will increase the potential on the one side, and lower it on the other. Thus, charge carrier can be emitted over a cascade of defects from the metal to the semiconductor (or vice versa). This effect only works if the fermi level is below the trap level, since otherwise the trap would already be occupied by an charge carrier.

The current law for the Poole-Frenkel emission is

$$J = nq\mu E \exp\left(\frac{q}{k_B T}\left(\sqrt{\frac{qE}{\pi\epsilon_0\epsilon_r}} - \phi_T\right)\right), \tag{2.14}$$

which is close to the current law of the Schottky emission, which makes it hard to distinguish between these two transport mechanisms. However, two factors help identifying the correct current mechanism.[206] First of all, an analysis of the pre-exponential coefficient can give a hint on effect. Poole-Frenkel emission is dependent on the charge carrier concentration and their mobility in the insulator, Schottky emission is dependent on the effective charge carrier mass in the dielectric. Secondly, as mentioned before, Poole-Frenkel is a conduction effect based on bulk defects, whereas Schottky emission is an interface effect. Thus, in an asymmetric sample structure, as it is given in metal-insulator-semiconductor devices, Poole-Frenkel will give a more symmetric current-voltage curve whereas Schottky emission will be asymmetric.

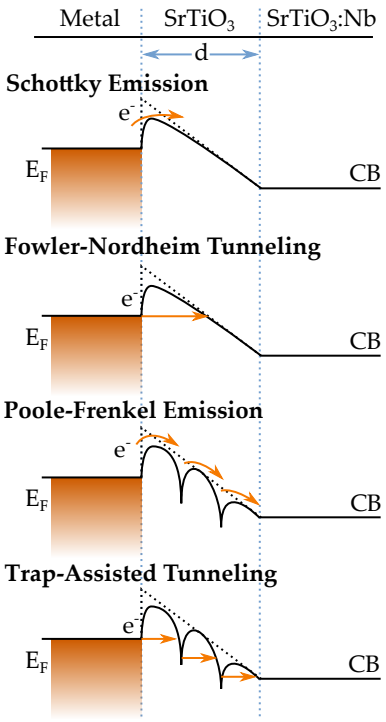

Figure 2.2: Schematic drawings of different transport mechanism which can occur in insulating thin films.

2.1.0.3 Tunneling

Until now, emission processes were discussed, which describe the thermal activation from the metal or the defect states into the conduction band. Another category of transport processes through the dielectric are tunneling processes. The transmission probability of charge carriers through the barrier can be calculated by the Wentzel–Kramers–Brillouin (WKB) approximation, which is

$$T = \exp\left(-\frac{2}{\hbar}\int_{x_0}^{x_1}\sqrt{2m(\phi(x)-E)}\,\mathrm{d}x\right) \tag{2.15}$$

T Transmission probability
m Effective charge carrier mass
E External field
ϕ Potential
x Potential coordinate
$\hbar$ Planck constant

The Fowler-Nordheim tunneling describes the process of charge carrier transmission through an triangular shaped barrier.[52] The barrier is triangular due to the applied electric field to the dielectric, which is reducing the effective barrier width for the charge carriers (figure 2.2). Since tunneling only occurs for thin barriers, Fowler-Nordheim is a transport effect only occurring for high electric fields, which gives a strong potential gradient in the dielectric and thus reducing the barrier width. The current density follows the equation

$$J = \frac{q^2}{8\pi h\phi_B}E^2\exp\left(\frac{-8\pi\sqrt{2qm^*}}{3hE}\phi_B^{3/2}\right). \tag{2.16}$$

The tunneling current is therefore dependent on the effective electron mass and the barrier height at the interface. An important difference to emission processes is, that the current-voltage measurement will be independent of temperature.

Tunneling through the dielectric can also be promoted by trap states in the thin film. In this case, the tunneling width is the average distance between the trap site and becomes[131]

$$J = A\exp\left(\frac{-8\pi\sqrt{2qm^*}}{3hE}\phi_T^{3/2}\right). \tag{2.17}$$

The trapping is dependent on the barrier height of the trap sites. Due to the reduced barrier width in trap-assisted tunneling, the effect can also occur at medium electric field strength. Since Poole-Frenkel conduction and trap-assisted tunneling are based on the charge transport between trap sites, also a combination of these mechanism was observed. The current-voltage relation is then[109]

$$\begin{aligned} J \propto E\exp\left(\frac{q}{k_BT}\left(\sqrt{\frac{qE}{\pi\epsilon_0\epsilon_r}}-\phi_{B_{PF}}\right)\right) \\ \times\exp\left(-\frac{4\sqrt{2qm}\phi_{T_{TAT}}^{3/2}}{3\hbar E}\right) \end{aligned} \tag{2.18}$$

2.1.0.4 Thermally assisted tunneling

Tunneling processes can also be thermally assisted. In this case, the charge carrier can pass the barrier at a higher potential. In case of e.g. a triangularly shaped barrier, this would reduce the effective barrier width.

The solution depends on the device structure and the conduction mechanism. Cuellar et al.[33] has calculated the thermally assisted tunneling over the Schottky barrier of a $La_{0.7}Ca_{0.3}MnO_3$/ $SrTiO_3$:Nb diode. The resulting current is

$$J \propto \frac{T^2(q(\phi_B - V) + \xi)^{1/2}}{k_B T \cosh(E_{00}/k_B T)} \times \exp\left(\frac{\xi}{k_B T} - \frac{q\phi_B + \xi}{E_0}\right) \tag{2.19}$$

ξ	Difference between E_C and E_F
E_{00}	Material constant

with

$$E_0 = E_{00} \coth\left(\frac{E_{00}}{k_B T}\right) \tag{2.20}$$

Other transport mechanism with thermally assisted tunneling can be found by solving the WKB approximation.

2.1.0.5 Other transport mechanism

The previously discussed models depend on the barrier heights of the interface or traps in the dielectric. In the case of high electric fields, also space charge limited current can occur. Following the Mott-Gurney law (an extension of Child's law for dielectric media), the current is only dependent on the permittivity and charge carrier mobility of the dielectric:

$$J = \frac{9}{8}\epsilon\mu\frac{V^2}{L^3}. \tag{2.21}$$

Several conditions for the occurrence of the space charge limited current are given, e.g. the dielectric has to have a low charge carrier concentration and not limited by traps. For dielectrics, in which traps play a role, the law can be extended to the Mark-Helfrich law[103], which is

$$J \propto \frac{V^{l+1}}{d^{2l+1}}. \tag{2.22}$$

l is a factor for the thermal activation of the traps.

Other mechanism can be hopping conduction mechanism, which play a role in amorphous semiconductors, or direct tunneling, which is important for very thin layers. Both mechanism were also reported for resistive switching, however, due to the thickness and crytallinity of the thin films, they don't play a role in the present work.

2.2 DIELECTRICITY, POLARIZTATION AND FERROELECTRICITY

In this part, an overview about dielectricity and polarization in crystals will be given. This chapter is mainly based on the textbook of Kittel[84], unless otherwise stated. The description of relaxor ferroelectrics is mainly based on a review article by Bokov et al.[13].

2.2.1 Dielectricity

$\vec{D}$	Electric displacement
$\vec{E}$	Electric field
$\vec{P}$	Polarization
χ	Susceptibility
ϵ_0	Vacuum permittivity
ϵ_r	Relative permittivity

An electric field is interacting with the free and bound charges in this field, which leads to an electric displacement field $\vec{D}$. This is defined by

$$\vec{D} = \epsilon_0 \vec{E} + \vec{P}, \tag{2.23}$$

which is the sum of the flux density of the vacuum ($\epsilon_0 \vec{E}$) and the polarization $\vec{P}$ in the field. The polarization is defined over the susceptibility χ, which is a measure of how easily the charges can be displaced, by

$$\vec{P} = \epsilon_0 \chi \vec{E} = \epsilon_0 (\epsilon_r - 1)\vec{E}. \tag{2.24}$$

Thus, equation 2.23 can be simplified to

$$\vec{D} = \epsilon_0 \epsilon_r \vec{E}. \tag{2.25}$$

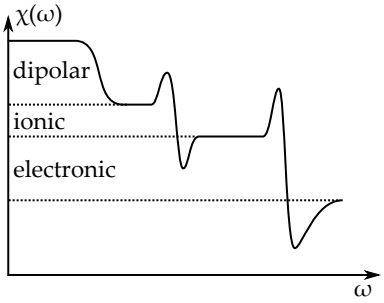

Figure 2.3: Susceptibility χ over the frequency ω. Graphic adapted from Kittel (ref. [84] p.485).

The susceptibility is generally a complex number, in which the real part describes the phase shift and the imaginary part the absorption of the electromagnetic wave. The susceptibility is the sum of several interaction mechanism of the electric field with the charges, e.g. the vibration of a crystal or molecule, or with free electrons. Each contributing mechanism is a function of the frequency of the electric field, resulting from a different relaxation time of the polarization. The contributions e.g. in a crystal can be divided in three categories, electronic, ionic and dipolar contributions. Electronic processes are fast, so the electric field can interact over a broad frequency range. Ionic contribution are slower, due to the higher mass compared to electrons. Thus, the electric field will only interact at lower frequencies, since the relaxation time is much higher. Concluding from this, in the most cases, the susceptibility has a larger value at low frequencies than at high frequencies. Therefore, the low frequency susceptibility (or permittivity) is often referred to be the static, the high frequency susceptibility as the optical one (since its in the range of visible or UV light). A schematic of the susceptibility over frequency is shown in figure 2.3.

2.2.2 Ferroelectricity

A special focus in the present work is put on the dipolar contribution of the susceptibility, like permanent dipoles. If the crystal has a permanent dipole moment, a polarization can be imprinted (or switched) by e.g. an external electric field, and the material is, in analogy to ferromagnetism, called ferroelectric. Materials with a permanent dipole moment are also piezoelectric (polarized under applying stress) and pyroelectric (spontaneously polarized) (figure 2.5). Permanent dipole moments occur in certain non-centrosymmetric symmetry point groups. A material class, which frequently shows ferroelectricity, are the ABO_3 oxides, which often have a perovskite crystal structure. Perovskites have a tetragonal crystal structure with a AO_2 and a BO sublattice, e.g $BaTiO_3$ in its distorted tetragonal phase below 120 °C.[105,188] On the other hand, cubic perovskite like ideal $SrTiO_3$ at room-temperature can't show ferroelectricity.

The permanent dipole moment is induced by an offset of the central B atom (figure 2.4) in the center of the unit cell. In the polarized crystal, the Ti is in either of the local minima of the double potential well, and the electric dipole moment is maintained even in absence of an external field. By applying an external electrical field or stress, the symmetry of the double potential well is broken an the crystal switched into the opposite polarization.

Analogously to ferromagnetics, these materials have a Curie temperature T_C, which can be connected to a structural phase transition of first-order. Above that temperature, the materials are in a paraelectric phase. To calculate the polarization in the ferroelectric, the Landau-Ginzburg theory is used. The free energy of a dielectric at a constant temperature is

$$\mathrm{d}F = \vec{E}\,\mathrm{d}\vec{P} \tag{2.26}$$

Using equation 2.24, the free-energy is

$$F = \int_0^E \epsilon_0\,(\epsilon_r - 1)\,\vec{E}\,\mathrm{d}\vec{E}\,. \tag{2.27}$$

In the Landau-Ginzburg theory, a power series expansion is used to include non-linear contributions to the polarization by

$$F(\vec{P},\vec{E}) = -\vec{E}\vec{P} + \frac{1}{2}\chi(T)\vec{P}^2 + \frac{1}{4}\eta(T)\vec{P}^4 + \cdots \tag{2.28}$$

The higher order odd terms a neglected in the case of crystals with inversion centers. To calculate the permittivity for a given field, the approach from Yamamoto et al.[205] is used. For simplicity, the calculation is performed one-dimensional, as the electric field is in the present work usually applied along the c-axis. From minimizing the free-energy

$$E = \frac{\partial F}{\partial P} = 0 = \chi(T)P + \xi(T)P^3, \tag{2.29}$$

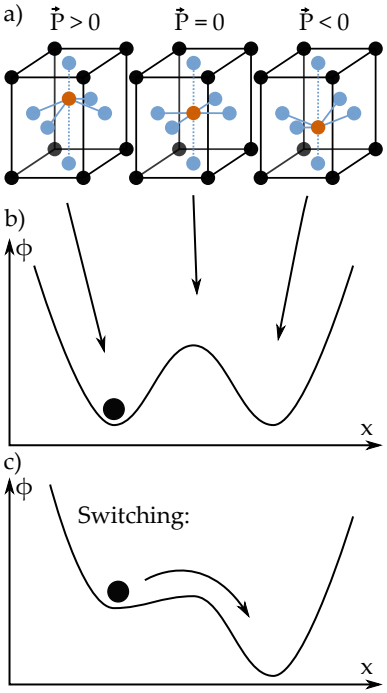

Figure 2.4: (a) Different polarizations in the perovskite structure. (b) A double potential well (ϕ) maintains the off-center position (x) of the central atom. (c) The central atom can be switched by an external force, e.g. an electric field.

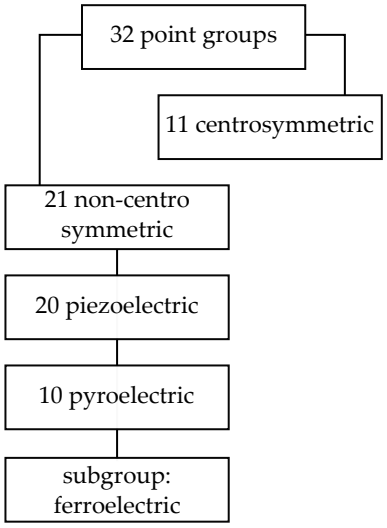

Figure 2.5: The symmetry of the crystal can influence the dielectric properties. Only non-centrosymmetric crystals can show an intrinsic ferroelectricity. Adapted from Haertling[64].

the polarization can be expressed by

$$P = \left(\frac{1}{2\xi}\right)^{1/3} \left(\left(\sqrt{a+E^2} - E\right)^{1/3} - \left(\sqrt{a+E^2} + E\right)^{1/3} \right) \quad (2.30)$$

with

$$a = \frac{4}{\xi}\left(\frac{\chi}{3}\right)^3. \quad (2.31)$$

The permittivity can be obtained from differentiating equation 2.23:

$$\epsilon(T,E) = \frac{\mathrm{d}}{\mathrm{d}E}(\epsilon_0 E + P) = \epsilon_0 \left(1 + \frac{h(E)}{\sqrt{a+E^2}}\right), \quad (2.32)$$

with

$$h(E) = \frac{1}{3\epsilon_0 (2\xi)^{1/3}} \left(\left(\sqrt{a+E^2} - E\right)^{1/3} - \left(\sqrt{a+E^2} + E\right)^{1/3} \right). \quad (2.33)$$

Yamamoto et al.[205] is using the approximation

$$\epsilon_r(T,E) \propto \frac{1}{\sqrt{a+E^2}}, \quad (2.34)$$

since they only observed a field dependence of the permittivity above $4 \times 10^5\,\mathrm{V\,m^{-1}}$. In the present work, the permittivity shows a field dependence already at lower fields, thus the approximation is not valid for the present work and was not used.

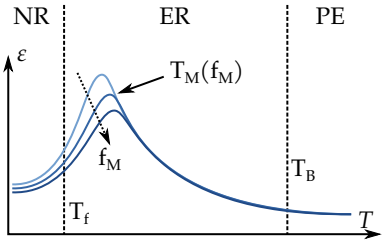

Figure 2.6: Dependency of permittivity ϵ to the temperature T in a relaxor ferroelectric. The maximum at T_M is dependent on the measurement frequency f. In the low temperature range, the PNRs are frozen, and the regions is called non-ergodic relaxor (NR). In the intermediate temperature region above T_f, the PNRs are mobile and ergodic, thus the phase is called ergodic relaxor (ER). Above the Burns temperature T_B, the dielectric phase is paraelectric (PE). Adapted from Dittmer[41].

2.2.3 Relaxor and Polar Nano Regions

Similar to domains in ferromagnetics, also ferroelectrics can have regions, in which der polarization is oriented in the same direction, but different to adjacent regions. The total polarization is then the sum of all positively and negatively oriented dipoles or regions. The domains boundaries may change and can be influenced by e.g. external electrical fields. For classical ferroelectrics, the domain size can be in the range of micro meters.

The relaxor ferroelectric is a special class of ferroelectrics. Relaxor ferroelectric domains are much smaller, in the nano range and thus called polar nano regions (PNR). The PNRs can form below a certain temperature, the Burns temperature T_B. The Burns temperature is higher than the Curie temperature, e.g. it was found for $Pb(Zr_yTi_{1-y})O_3$, that the Curie temperature is in the range of 80 °C to 155 °C and the Burns temperature is in the range of 350 °C to 410 °C.[19]. Above the Burns temperature, relaxor ferroelectric have, similar to ferroelectrics, a paraelectric state. While classical ferroelectrics loose their ferroelectric properties due to a structural phase transition (e.g. tetragonal to cubic), in relaxor ferroelectrics, no structural phase transition occurs at the dielectric phase transitions. The polar nano regions are mobile above

another characteristic temperature T_f. Below this temperature, the PNRs are frozen. The temperature range $T_f < T < T_B$ is called ergodic phase, in which the PNRs behave ergodic, which refers to the dynamics of the PNR and their stochastic behavior (figure 2.6). The maximum permittivity at T_M is dependent on the measurement frequency f_M and follows a Volger-Fulcher relation

$$f \propto \exp\left(-\frac{E_a}{T_M - T}\right), \tag{2.35}$$

due to dipolar dispersion. In the non-ergodic phase, by applying an external field, the dielectric properties can get ferroelectric, but above T_f, the material will return to its ergodic phase.

The stability of the ergodic phase depends on the correlation between the polar nano regions. Depending on temperature or density of polar nano regions, the regions can be weakly correlated and after e.g. an external excitation by an electric field, the regions will return into their initial state. In the case that the correlation is higher, due to the density of dipoles or the low temperatures, the relaxation time will drastically increase and the dipoles will keep their state. Since the PNRs can have different correlation strengths, the system will have a broad spectrum of relaxation times.

2.3 RESISTIVE SWITCHING

Resistive switching is an effect measured in electric devices, which show a changing resistivity by applying certain voltages. A resistive switching device can have two or more stable resistivity levels, which can be either persistent or meta-stable. These states are called high resistive state (HRS) and low resistive state (LRS), for the insulating and the conductive state, respectively. To switch between those states, a switching voltage is applied. The sign of the switching voltage usually defines the switching direction, e.g., a negative switching pulse changes the devices from the LRS to HRS and a positive pulse from HRS to LRS. A small readout voltage is then used to measure the current state without changing it.

Resistive switching can be classified in different categories, e.g. electrochemical switching, valence change switching or phase change switching.[193] In the following, a selection of models used to describe resistive switching will be introduced, with the focus on the materials and resistive switching meachnism discussed in the present work.

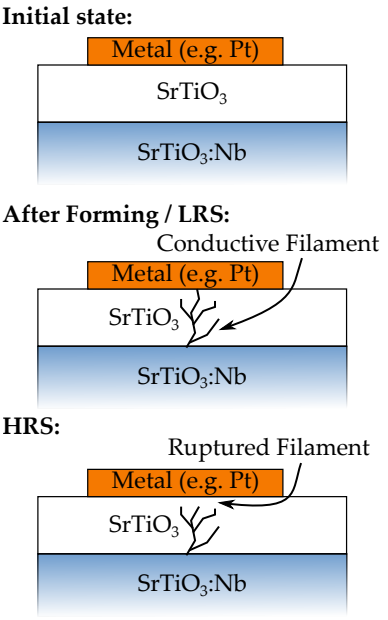

Figure 2.7: Filament model for resistive switching with its three states. A forming pulse is applied to an insulating thin film. Afterwards the layer is in the LRS. With reverse biasing the device, the filament can be ruptured again and the device is in the HRS.

Filament switching

Filament switching is a model of resistive switching, in which shallow defects, in the most cases in the form of V_O, form a conductive filament (figure 2.7). This filament is formed by a dielectric breakdown, induced by a high voltage pulse. By applying an electric field, these filaments can be then broken due to defect drift in the electric field and reformed by reversing the electric field. Current-voltage characteristics frequently show a discrete jump of several order of magnitude between the LRS and HRS. The switching voltage is hereby not a defined voltage, which is same for each switching between HRS and LRS, but can differ by several hundred millivolts, as well as the current level for each state, which can change by orders of magnitude.[71]

The origin of this model are measurements by Rossel et al.,[148] who performed electron beam-induced current (EBIC) measurements, to identify current hotspots below an electrode of a $Pt-SrZrO_3-SrRuO_3-SrTiO_3$ structure. The appearance of several conductive hotspots for the LRS and the disappearance of those by switching to the HRS were shown. Following the present work, supporting measurements were done e.g. by conductive AFM[172]. These measurements showed a highly conductive spot on the surface. An approach to directly visualize the filaments was done by Du et al.[42], who used STEM with electron energy loss spectroscopy (EELS) to detect filamentary defects in a thin film. He measured V-shaped structures with a high concentration of V_{Sr}, Ti^{3+} and V_O. The defects did not cause any lattice damage, e.g. by dislocations or other extended defects.

Fast switching speeds in the range of 40 ns to 100 ns were reported.[193,196] To explain such fast switching times, the drift mobility of the V_O must be high and it is assumed, that joule heating plays a important role in the switching process.[92]. Simulations have shown, that due to the small size of the filament and the high current densities, the filament can reach temperature of 800 K by joule heating, which supports the model to explain the fast switching.

Valence change

Another approach to explain resistive switching is the valence change model. The origin of the valence change model is the observation, that in $SrTiO_3$, Ti^{4+} is reduced to Ti^{3+}. This is originally observed in filaments by STEM, however, reports of homogeneous switching without filament formation led to adjustments of the switching model.

One property of these switching mechanism is the absence of a hard forming step. Instead, a soft-forming is performed, which

is an initial sweep to the LRS switching voltage, but not above. During this step, V_O are introduced into the layer. Afterwards, the current-voltage sweeps show an increased current and a hysteresis. The mechanism for switching is based on the electric field drift of V_O to the metal-insulator interface for the LRS, and a homogeneous redistribution of the vacancies by reversing the electric field (figure 2.8).

Due to the higher concentration of V_O near the interface, the space charge region is reduced, allowing a higher tunneling current through the Schottky barrier. In the case of the HRS, the more homogeneously distributed V_O lead to a wide space charge region and thus a smaller tunneling current through the barrier.

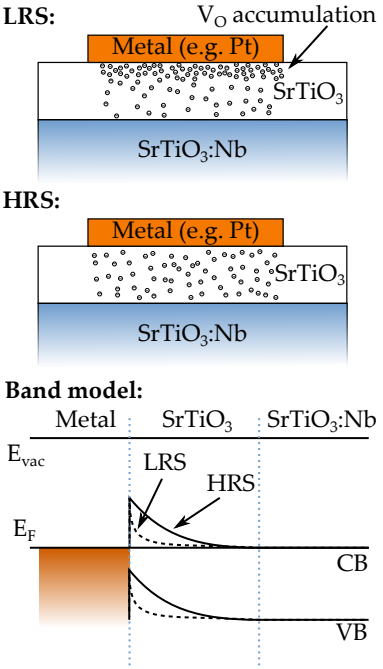

Figure 2.8: Valence change model, based on accumulation (LRS) and redistribution (HRS) of V_O by an electric field. The band model shows, that the accumulation near the metal interface leads to a reduced space charge region and thus higher transmission probability of charge carriers.

Ferroelectric tunnel junctions

Ferroelectric tunnel junctions are based on the change of resistivity due to a change of ferroelectric polarization.[57] The change in tunnel electro resistance can be manifested in different ways. One possibility, e.g. by a change of barrier height or by a change of barrier width by depletion or accumulation at the interface (figure 2.9). Another possibility is a change in the density of states, which results in a change in tunneling probability. Typically, ferroelectric tunnel junctions were developed on intrinsic ferroelectric materials like $PbTiO_3$ or $BaTiO_3$, which show stable polarization due to their non-centrosymmetric crystal structure below the Curie temperature.

There exists a critical thickness, below which no stable polarization can be achieved. The reasons are e.g. depolarization fields from the electrode.[140] Additionally, the polarization vanishes above the Curie temperature.

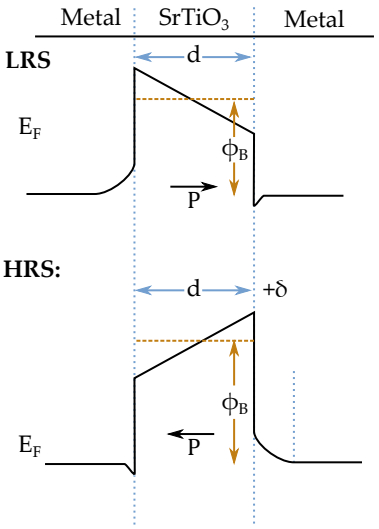

Figure 2.9: Schematic band diagram of ferroelectric tunnel junction. Adapted from Garcia et al.[58]

Metal-insulator transitions

Metal-insulator transitions (MIT) are transitions in the electronic structure of a material, accompanying a structural phase transition. The metal-insulator transition can be triggered by several mechanism, e.g. temperature or pressure, making them applicable for various switches and sensors. A way how the (MIT) can occur is the Mott transition.[112] The Mott criteria

$$n^{1/3}a \simeq 0.2 \tag{2.36}$$

defines, if a crystal is insulating (< 0.2) or metallic (> 0.2). The reason for this is the strong localization of charge carriers, which leads to the formation of a band gap in the case of too large distances of the atomic sites.

Another mechanism is the Peierls transition, which corresponds to the electron-electron correlation and is related to a

n	Charge carrier density
a	Bohr radius

structural phase transition. The structural phase transition leads to charge density waves, in which the orbitals of two atoms are dimerized. This again can lead to the formation of a band gap. Both effects can occur at the same time and was shown e.g. in VO_2. Peierls transitions are of special interest for resistive switching applications, as the dimerization e.g. in NbO_2 depends on the bond length. An external electric field can lead to an displacement of the atoms and the change of bond length can break the dimerization.[187] This state is meta stable, as without an external field, the atoms move back to their original position.

3 EXPERIMENTAL METHODS

This section describes the main measurement methods used in the present work and focuses on the explanation of the tools and setups used, as well as of the physical information, which can be obtained from these methods.

3.1 RESISTIVITY AND HALL-EFFECT

3.1.1 Room-temperature measurements

Room-temperature resistivity and Hall effect measurements were performed to investigate the electrical properties of thin films. Using Hall effect and resistivity measurements, the charge carrier concentration and the mobility can be derived.

For this, the measurement was performed in a Van-der Pauw setup. A Van-der Pauw measurement can exclude the wiring and contact resistance from the device resistivity, which are giving a series resistance contribution in a 2-point probe measurement. To achieve this, the supply of current and the measurement of voltage are performed over separate wiring (see figure 3.1). A constant current is supplied via two wires, and the voltage drop of the sample is measured between the other wires.

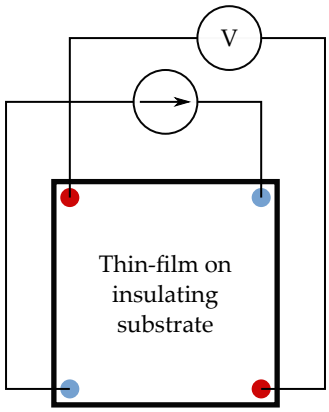

Figure 3.1: Resistivity measurement of thin films in 4-probe setup. A constant current is supplied over the blue contacts and the potential drop is measured over the red contacts. In this case, the measurement is performed in Van-der-Pauw geometry.

Generally, the calculation of the device resistivity is dependent of the sample shape and the probe geometry. However, in a Van-der-Pauw setup, the resistivity can be derived for arbitrary shaped samples and probe geometries. For this, several conditions have to be fulfilled[157]:

1. the contacts are at the circumference of the sample
2. the contacts are are sufficiently small
3. the sample is homogeneous, e.g. uniformly thick, no holes or insulating islands within the sample area

The resistance $R_{ij,kl}$ is determined by applying a constant current I_{ij} between contacts i and j and measuring the voltage V_{kl} between k and l:

$$R_{ij,kl} = \frac{V_{kl}}{I_{ij}} \tag{3.1}$$

The resistivity of the sample is then[181]

$$\rho = \frac{\pi d}{\ln(2)} \frac{R_{12,34} + R_{23,41}}{2} F \tag{3.2}$$

ρ	Resistivity
V	Voltage
R	Resistance
I	Current
d	Layer thickness
F	Correction factor

The correction factor F is a function of the ratio $R_r = R_{12,34}/R_{23,41}$ [157] with

$$\frac{R_{12,34} - R_{23,41}}{R_{12,34} + R_{23,41}} = \frac{F}{\ln(2)} \operatorname{arcosh}\left(\frac{\exp(\ln(2)/F)}{2}\right). \tag{3.3}$$

However, in case of a symmetrical sample, $R_r = 1$ and $F = 1$, so that that equation 3.2 can be simplified to

$$\rho = \frac{\pi d}{\ln(2)} R_{12,34}. \tag{3.4}$$

Additional corrections can be calculated, e.g. for contacts which are not located at the circumference of the sample or if they are not sufficiently small compared to the sample surface. In the present work, contacts were exclusively located at the corners of the sample and the size was kept small, so that these correction was neglected.

The contact preparation is an important factor in the measurement of the resistivity. Two types of contacts were used in the present work to measure the resistivity (and Hall effect) in $SrTiO_3$ and NbO_2 samples. For room-temperature measurements, an eutectic of In/Ga, which is liquid at room-temperature, were applied to the sample surfaces. The application were done by covering a needle with the eutectic and scratching with it on the dedicated contact areas. This has the advantage, that insulating surface layers can be broken and the eutectic directly contacts the thin film (without exposing it to air again) and relatively small contacts can be applied.

The second method was the deposition of titanium/gold contacts for temperature dependent measurements (chapter 3.1.2). In this case, e-beam evaporation was used to deposit 50 nm of titanium and 50 nm of gold through a shadow mask. The gold layer prevents oxidation of the titanium layer. This contacts can also be used for low and high temperature measurements.

All contacts were tested before measuring the resistivity or Hall effect for their ohmic behavior by measuring current-voltage curves in 2-point probe setup.

Hall effect measurements give information of the sample majority charge carrier concentration and mobility, as well as the type of majority charge carriers. A hall setup `Lake Shore HMS 7504` with an magnetic field strength of 0.3 T was used. By applying the magnetic field perpendicular to the sample surface, the Hall mobility can calculated by measuring the change in resistance of $R_{BC,AC}$ with and without magnetic field by

μ_H	Hall mobility
B	Magnetic field strength
q	Elementary charge
n	Charge carrier concentration

$$\mu_H = \frac{d}{B} \frac{R_{BD,AC}(0) - R_{BD,AC}(B)}{\rho}, \tag{3.5}$$

The charge carrier concentration can be then calculated by

$$n = \frac{1}{\rho \mu_H q}. \tag{3.6}$$

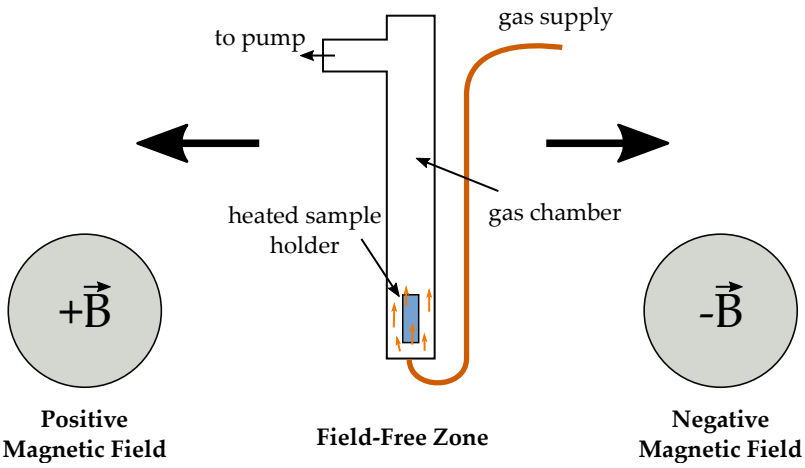

Figure 3.2: Schematic setup of the `Fraunhofer HT` 1100 K hall system for high temperature hall effect measurements in controlled atmosphere. The sample holder, placed within a gas chamber, is moved between three positions, the zero-field position and two positions between permanent magnet pairs with opposite polarity with a field strength of ± 0.5 T.

In this notation, the sign of n also gives the type of majority charge carrier, electron or holes.

3.1.2 Temperature dependent measurements

Temperature dependent resistivity measurements were performed to measure the ionization energy of defects in NbO_2 (see chapter 4.3.2). The measurement was performed in two separate systems, the first for low temperature, the second for high temperature measurements. To perform the measurements, titanium gold contacts were used.

For low temperature measurements, the sample was measured with the Hall effect measurement tool described in chapter 3.1.1. The sample was cooled down using a closed-cycle helium refrigerator to temperatures of around 20 K. For this, the sample was kept under vacuum to prevent thermal conduction. An electrical heater mounted below the sample was used to heat the sample in a temperature range of 20 K to 400 K.

The high temperature measurements were performed in a *Fraunhofer HT* 1100*K* Hall effect system (figure 3.2). The setup consist of three zones: two magnetic zones, providing a magnetic field strength of 500 mT. The magnetic zones consist of permanent magnet pairs. The field direction is opposite between the two magnetic zones. Between the magnetic zones, the third, field-free magnetic zone is located. The measurement is then performed by moving the sample between the three zones to measure the resis-

tivity without and with magnetic fields, to obtain the parameters mentioned in chapter 3.1.1.

In this setup, the sample can be heated from room-temperature up to 1100 K in different atmospheres. For this, the sample is located in a gas chamber. Annealing gases argon, oxygen, nitrogen and forming gas consisting of 96 % argon and 4 % hydrogen can be used, to investigate the oxidation and reduction behavior of samples at elevated temperatures.

The atmosphere can be controlled in two ways. Prior to growth, the chamber is filled with the annealing gas and then sealed. This leads to an increase of pressure with heating the sample. The second way is to not seal the chamber, but pumping it during the whole process, and simultaneously supply the annealing gas to the chamber. For this, an gas inlet is directly placed next to the sample. This measurement mode provides stable annealing conditions, however, due to the continuous flow of cold gas into the chamber, the maximum temperature is reduced.

3.2 METAL–INSULATOR–SEMICONDUCTOR AND SCHOTTKY DEVICES

For investigating the resistive switching and the dielectric properties, two kind of sample structures, metal-insulator-semiconductor devices and metal-semiconductor Schottky diode were used. In the following, the preparation of top electrodes, which can influence the device properties, will be explained as well as the measurements modes for electric and dielectric will be introduced.

3.2.1 Electrical contact preparation

For electrical top contact preparation, e-beam evaporation was used. The contacts were deposited through shadow masks, which are available in different geometries. The most commonly used masks are

- Circular contacts with diameters of 150 µm, 200 µm and 300 µm, used for capacitance-voltage and current-voltage measurements in $SrTiO_3$. The small contact size is needed due to the high capacitance of these devices, resulting from the high relative permittivity of $SrTiO_3$
- Clamping holders for concentrically aligned front and back side contacts, used in plate capacitor structures (see chapter 5.2.1)
- Shadow masks for corner contacts used in temperature-dependent resistivity measurements (see chapter 4.3.2).

Together with the shadow mask, the samples were introduced into the vacuum chamber, which was pumped down to a pressure of 3×10^{-6} mbar over night to reduced the residual water vapor pressure. The metals were stored in carbon crucibles and heated by a electron beam with a current of around 60 mA to 200 mA, depending on the metal. During heating and degassing phase of the metal, a sample shutter prevents deposition of the metal. With opening the shutter, the deposition starts and the deposition rate was measured by a oscillating quartz. The shutter is closed automatically with reaching the dedicated sample thickness, measured by the oscillating quartz.

For the different purposes of measurement, different metal layer structures were used: Titanium / gold contacts with a thickness of 50 nm were used for ohmic contacts on $SrTiO_3$ and NbO_2. Platinum was used for Schottky contacts and to contact metal-$SrTiO_3$-$SrTiO_3$:Nb structures. An electrode thickness of around 50 nm to 100 nm was used. During the experiments, a low stability of the platinum contacts were recognized. To improve mechanical stability, the contacts used for MOVPE grown samples consists of 20 nm platinum, protected by a 30 nm nickel layer.

Ohmic backside contacts were prepared in two ways. For room-temperature and low-temperature measurements, a thin layer of liquid In/Ga eutectic was applied to the backside. Silver glue was used to glue the sample on the sample holder for low temperature measurements.

3.2.2 Current-voltage measurements

$SrTiO_3$ thin films were investigated for their transport and resistive switching properties by 2-point probe measurements. The electrical contact preparation was described in the previous chapter. A `Keithley 237 source measure unit` was used to measure current-voltage curves. The measurements were performed in the dark to prevent photo conduction. To measure temperature dependence, a `Janis CCS-400H` closed-cycle refrigerator was used for cooling and heating the sample in a temperature range of 4 K to 800 K.

For special measurement modes, e.g. recording hysteresis curves or performing pulsed measurements, the electrometer was controlled by a self-made control software, based on `Python`.

3.2.3 Capacitance voltage measurements

Capacitance voltage measurements were used to characterized the dielectric properties of insulating $SrTiO_3$ thin films and substrates, as well as characterizing Schottky diodes. In case of in-

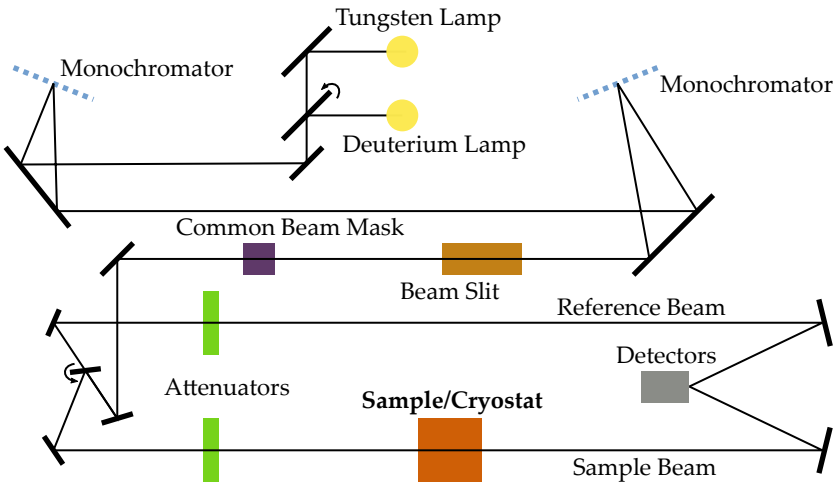

Figure 3.3: Schematic setup of the `Perkin-Elmer Lambda 1050` for optical absorption spectroscopy.

ϵ_r	Relative permittivity
ϵ :	Vacuum permittivity
C	Capacitance
d	Layer or sample thickness
A	Contact area
N_D	Donor concentration
V_{Bi}	Built-in voltage
V	Applied voltage
k_B	Boltzmann constant
T	Temperature
q	Elementary charge

sulating thin films, the permittivity can estimated over the plate capacitor equation

$$\epsilon_r = \frac{Cd}{\epsilon_0 A}. \tag{3.7}$$

Measuring capacitance voltage curves of Schottky diodes can give information about the acceptor and donator concentration as well as the permittivity value. The capacitance results then from

$$C = \sqrt{\frac{q\epsilon_0\epsilon_r N_D}{2\left(V_{\text{bi}} - V - \frac{k_B T}{q}\right)}} A. \tag{3.8}$$

The measurements were performed by either using a `PhysTech FT 1030` system. The measurement frequency is 1 MHz and the excitation voltage was 100 mV. Temperature dependent measurements were done using a `Janis CCS-400H` closed-cycle refrigerator with an operating temperature range of 4 K to 800 K.

3.3 OPTICAL ABSORPTION SPECTROSCOPY

Optical absorption spectroscopy was performed by using a `Perkin-Elmer Lambda1050` double beam, double monochromator spectrophotometer. The setup is shown in figure 3.3 The device is equipped with two light sources, a deuterium and a tungsten lamp, as well as with three detector units, covering a broad wavelength range of 175 nm to 3300 nm. The light is monochromized by two monochromators. The width of the beam slit influences the light intensity and resolution of the probing beam. The common beam mask is set to control the height of the beam, so that only the sample is illuminated. A reference beam is used for

intensity corrections, whereas the sample beam illuminates the sample. Both beams can be controlled in intensity by using attenuators. A `Oxford Instruments` liquid helium cryostat can be used to cool the sample down to 4 K.

Prior to a measurement, 0 % and 100 % intensity background reference spectra are recorded. For this, the spectra are recorded without the sample in the beam, but e.g. with the cryostat or empty sample holder, which can cause extra absorptions or stray light at e.g. windows.

The sample is characterized by measuring the transmission spectrum. Using this method, the absorption edge can be measured, which gives information about the size and the type, indirect or direct, of the band gap. From the transmittance T, the absorption coefficient α can be determined by

$$\alpha(\lambda) = -\frac{\ln\left(T(\lambda)\right)}{d} \tag{3.9}$$

with the sample thickness d. The band gap and the type of band gap can be determined by using Tauc plots. In case of a direct band gap, the absorption edge is linear for $(\alpha E_{\text{Photon}})^2$ over the photon energy. In case of a indirect semiconductor, the absorption edge is linear for $(\alpha E_{\text{Photon}})^{1/2}$ over the photon energy. For reduce light scattering, all samples were polished with chemical-mechanical polishing by the crystal preparation group of the IKZ.

4 NIOBIUM DIOXIDE

NbO_2 has recently gained interest, as it, similar to materials like VO_2[167], undergoes a metal-insulator transition. It's huge advantage is the high temperature of around 1080 K[2,75,161] of its Mott-Peierls like phase transition[49,124,187], which makes it a competitive material to other materials with a near or sub room-temperature phase transition.[135,167] Even though materials with an insulator-metal transition can be interesting for temperature related operations (like thermal switching[81]), the strength of NbO_2 is in the field-driven phase transition of the material[55,82,163]. Using NbO_2 for electrical devices, the high temperature of the phase transition can efficiently prevent unwanted thermal switching due to joule heating of the device, as it would be a problem for room-temperature transition temperatures. The possibility to switch between the two phases by an external electric field opens the possibility to use NbO_2 in resistive switching materials.

Unlike other resistive switching materials like $SrTiO_3$ or Nb_2O_5, it does not persist its state after turning off the bias and thus is so called "threshold switching" material[55,82,163]. Only by applying a voltage above a certain voltage U_T, the device gets conductive, after removing electric field it will switch back to its semiconducting/insulating state. NbO_2 is therefore not necessarily suitable as a storage material, but can be used in combination with such a material. One useful field of application would be the *selector device*.[118]

Memristors can only fully develop their advantages if they are operated in a crossbar array, without the use of additional transistors to select the active cell, in order to exploit the fast switching times and high energy efficiency. However, crossbar arrays allow the occurrence of parasitic ("sneak") paths (figure 4.1(a)). In a device with a crossbar layout of 100 × 100 cells, only 1 % of the energy used for reading the status of a selected cell, 98 % of the energy is dissipated by sneak paths.[93]

By using a selector device like NbO_2, the active transistor element can be saved, which reduces complexity of the structure and might increase readout and writing speed.[83] The selector device, directly stacked on the memristive storage cell (figure 4.1(b-c)), would only allow access to the cell, if the voltage is above a certain threshold.[118] If parasitic current path occur, the selector device would efficiently block these currents, since always as cascade of cells are needed for the parasitic current paths. However, at each selector cell, the voltage drops by U_T/n, with n as the number of

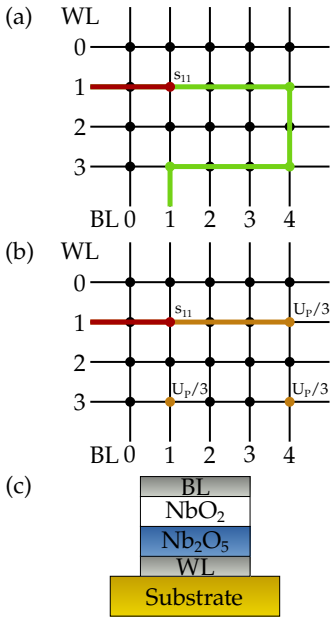

Figure 4.1: (a) ReRAM crossbar array without selector device. The dots represent cells s_{ij}. To probe the state of cell s_{11}, a voltage U_P is applied on WL1 and the current is probed on BL1. The state of cell s_{11} is 0 (red), but since the current can pass through the parasitic path $s_{14} - s_{34} - s_{31}$, a state of 1 (green) is measured. (b) In this device design, each cell has a NbO_2 selector layer integrated. If the probe voltage $U_P \sim U_T$ of the NbO_2 layer, the parasitic path is effectively blocked, since the voltage is dropping by $U_P/3$ ($n = 3$) and $U_P/3 < U_T$, thus the NbO_2 layer is in its insulating phase. (c) Stacked structure with selector layer (NbO_2) and resistive switching layer (Nb_2O_5) suggested by Nandi et al.[118]

cells in the parasitic path, so in each parasitic cell the external field would not be sufficient to open the selector device (figure 4.1(b)). Consequently, only the shortest path with a single cell ($n = 1$) would provide enough field strength to open the selector and enabling cell access.

So far, NbO_2 thin films with low resistivities of 0.4 Ω cm to 54 Ω cm[50,79,123,191] at room-temperature were reported in literature, compared to the bulk value of 10 kΩ cm.[75] This hinders the material of being used as a selector, as it significantly lowers the on-off ratio and does not effectively block the current in off-state.

This chapter focuses on the epitaxial growth of NbO_2 layers and their structural, optical and electrical properties. A key result is, that by annealing the epitaxial layer above the phase transition temperature, the resistivity of thin films is increased by almost two orders of magnitude. A model for the residual conduction mechanism is developed and a precise value for the optical and electrical band gap was measured. In the first chapter, the basic properties will be discussed, followed by the description of the epitaxial growth of NbO_2 by pulsed-laser deposition. In the following section, the electrical properties of the layers will be discussed and in the final part, the determination of the band gap will be presented.

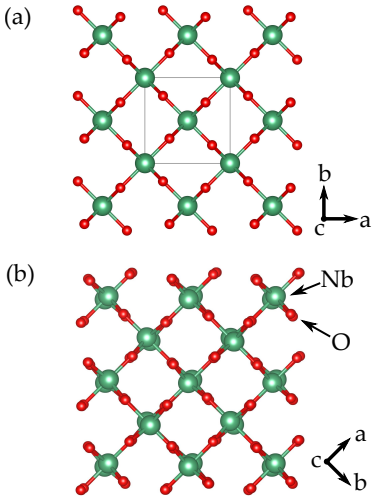

Figure 4.2: Crystal structure of NbO_2. (a) Above 1080 K, NbO_2 is in its metallic (tetragonal) rutile phase. (b) Below that phase transition, NbO_2 is in a distorted body-centered tetragonal phase. Since this phase deviates just slightly from the rutile structure by a shift of the Nb-atoms, it is also commonly referred as the distorted rutile phase.[138] The shift of the Nb-atoms leads a the formation of a band gap and thus the semiconducting/insulating phase. Created with [110].

4.1 BASIC PROPERTIES

Niobium dioxide is one of three stable phases at ambient conditions among niobium monoxide and niobium pentoxide. Niobium dioxide was first investigated for its metal-insulator transition in 1966. Janninck and Whitmore found, that above 830 °C[2,75] the resistivity of the layer drops by several orders of magnitude and retain its value. This is the typical temperature dependence for metals at high temperatures. This was also observed in the related material vanadium dioxide, which was intensively investigated for its metal-insulator transition[22,77,115,139,167].

In NbO_2, the transition is of Mott-Peierls type (see. chapter 2.3), meaning a corresponding structural and electrical transition[49,187]. The structural transition is hereby quite small, but the effect is huge[124,187]. Starting from the high-temperature phase, NbO_2 is in a (tetragonal) rutile structure (space group $P4_2/mm$[25]), with the lattice parameter $a = 4.8463$ Å and $c = 3.0315$ Å.[14] Going below to the transition temperature, the structure gets distorted[138] and is now in a distored body-centered tetragonal phase (space group $I4_1/a$[25]), having a significantly larger unit cell with $a = 13.7020$ Å and $c = 5.9850$ Å[14] (see table 4.1 and figure 4.2). Even though the unit cell is much bigger now, only a small break in symmetry occurs by a shift of the

Nb atoms, with a changing Nb-Nb bond length from 2.82 Å to 2.74 Å.[187] The result is a dimerization of Nb-Nb d-orbitals, which leads to the formation of a band gap.[125,187] The band gap is sensitive on the Nb-Nb bond length, which was shown by Wahila et al.[187]

The sensitivity on the bond length can be beneficial and challenging at the same time. Beneficial, because it makes switching easy. First models for the resistive switching behavior were based on joule heating and conductive filaments.[55,117,165] By applying an electric field to the device, filaments form and lead to an conductive channel. Due to the nanoscopic character of the filaments, the current density is high, leading to a high filament temperature of several hundred degrees and thus switching to the metallic phase. By turning off the electric field, the temperature in the filament drops and the device is switching to the semiconducting phase. Beside it is not clear, how the filament is formed and no direct proof of the filament was shown so far, another problem occurred for this model. Rana et al.[142] made experiments with terahertz radiation to locally induce electric fields within the material to demonstrate the resistive switching. The local heating by the radiation was hereby below the metal-insulator transition temperature. Thus, they demonstrated the switching by inducing an electric field, which causes atomic displacement. Since the displacement only needs to be in the sub-angstrom region, it can easily be induced by an electric field.

However, the sensitivity of the band gap on the displacement of the Nb atoms is also challenging, since it makes it necessary to grow high quality material. Defects can lead to repulsion forces or dangling bonds, foreign atoms in the crystal would not form a dimer with the Nb d-orbital. Especially extended defects like grain boundaries might lead to conductive paths. This sensitivity on the structural quality might explain the spread in resistivity and optical band gap. Whereas for bulk crystals a high intrinsic resistivity was shown, thin films can have resistivity values several magnitudes below.[50,79,116,123,191] The optical band gap values spread from 0.28 eV to 1.16 eV.[2,98,125,150,197] If we consider the mechanism for the band gap formations, the spread in data can be explained by lack of structural quality and thus a collapse of the band gap (e.g. by reduced dimer bond length) in the low temperature phase. This directly influences the device performance of resistive switching devices. If the low temperature resistivity is only in the range of mΩ cm, then the on-off ratio is reduced. Furthermore, it is also problematic for the application as a selector device, since a low (absolute value of the) resistivity would not prevent parasitic conduction paths in memristive crossbar arrays.

Further information about the NbO_2 and related niobates can be found e.g. in the review article by Nico et al. in reference [121].

4.2 STRUCTURAL PROPERTIES OF EPITAXIAL LAYERS

4.2.1 Epitaxy of NbO_2(001) on MgF_2

Niobium dioxide is not available as a substrate material, which makes it necessary to use hetero-epitaxy with foreign substrates for the deposition of epitaxial layers. The choice of substrate was hereby not trivial. A substrate matching the following parameters are preferable for hetero-epitaxy:

- crystal structure and/or surface reconstruction
- lattice parameter
- thermal expansion coefficient

The epitaxial growth of oxide semiconductors require additional considerations. A typical problem occurring in the epitaxy of oxide materials is the diffusion of oxygen vacancies[45,158]. In particular, their formation is promoted during growth by pulsed laser deposition (PLD) due to the low oxygen partial pressure inherent to the vacuum atmosphere of this process.[51] But oxygen vacancies may also be formed during annealing under non-oxidizing atmospheres. Interdiffusion of oxygen between substrate and epitaxial layers can then easily occur at elevated temperature, e.g. growth, cooling or heating.[17]

Another requirement is the conductivity of the substrate. Substrates like $SrTiO_3$ or TiO_2 can provide n-type conductivity by the presence of oxygen vacancies.[76] However, oxygen vacancies in the substrates can also induce n-type conductivity in the epitaxial NbO_2 layer by inter-diffusion and thus, oxygen vacancy poor substrates are preferable. In fact, we performed experiments on several oxide based substrates, e.g. TiO_2, $LaAlO_3$ and $SrTiO_3$, and the interdiffusion was omnipresent. Even unintentionally oxygen reduced substrates show a strong formation and interdiffusion of the vacancies into the epitaxial layer due to the high growth temperature and high-vacuum atmosphere. In case of requiring a conductive substrate, thus an intentionally doped substrate (ideally with a high V_O formation energy or a deep-level V_O) is needed, which is further limiting the number of possible substrates. Additionally, a wide band gap material with a transparency in the UV, visible and infrared spectrum would provide the opportunity of optical absorption experiments of the NbO_2 thin film.

As a result of the above described constraints, MgF_2 was finally chosen as the substrate crystal. The absence of oxygen in the material is a strong advantage for this material. With a band gap of above 11 eV,[160,177] MgF_2 is transparent from the deep ultra-violet

parameter	NbO_2		MgF_2 [143,184]
	$T < 1080\,K$ [14,151]	$T > 1080\,K$ [14]	
a	4.8463 Å	13.7020 Å	4.628 Å
c	3.0315 Å	5.9850 Å	3.0345 Å
α	$2.5 \times 10^{-6}\,K^{-1}$		$13.4 \times 10^{-6}\,K^{-1}$

Table 4.1: Structural parameter for NbO_2 and the substrate material MgF_2. a and c are the lattice parameter in the tetragonal crystal structure, α is the thermal expansion coefficient at 300 K

to the infrared spectrum of light and allows transmission spectroscopy for the measurement of optical properties of NbO_2. And finally, like NbO_2 in its high temperature phase, MgF_2 crystallizes also in a tetragonal crystal with the space group $P4_2/mnm$.[184]

There are several disadvantages to use MgF_2 as a substrate material for hetero-epitaxy of NbO_2. The lattice mismatch, calculated by $(a_{NbO_2} - a_{MgF_2})/a_{NbO_2}$ is according to the structural parameter in table 4.1 4.5 % between the substrate and the epitaxial layer, which will lead to a relaxation of the layer after a few nanometer. The difference in thermal expansions coefficient (see table 4.1) will lead to an additional residual strain, after cooling the sample from the high growth temperature to room-temperautre. Furthermore, MgF_2 is insulating and no n-type substrate is commercially available. Experiments also have shown, that the substrate preparation is difficult and occasionally, a delamination of layers occurred. Electron radiation is easily damaging the MgF_2 crystal, preventing transmission electron microscopy experiments. Nonetheless, due to the similar crystal structure and the absence of oxygen, MgF_2 was chosen for the substrate material.

The epitaxial growth by pulsed-laser deposition, described in the following part, was performed and developed by Jos E. Boschker, as well as the measurement of the structural data by x-ray diffraction. The residual strain analysis was performed by myself. The data in this section were published in Ref. [169]. A schematic drawing of the PLD setup is shown in figure 4.4. A commercially purchased ceramic target of Nb_2O_5 with a purity of 99.9985 % was placed at a distance of 60 mm below the substrate. The substrate is glued with silver glue on a sample holder and hanging with the epitaxial surface upside down, facing the Nb_2O_5 target. The substrate holder is heated by an resistive backside heater. The setup is placed inside a high-vacuum chamber at a background pressure of 1×10^{-6} mbar. Through a window, the target is irradiated by a KrF laser with a wavelength of 248 nm. An aperture is used to cut off the flanks of the Gaussian laser beam, to achieve a homogeneous, flat-top like laser profile for

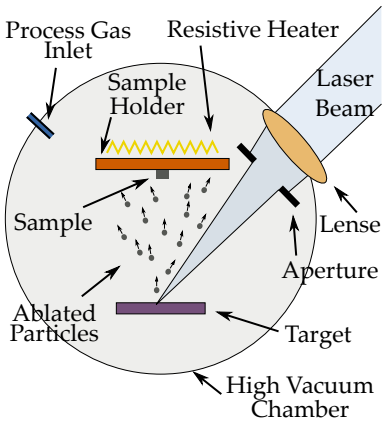

Figure 4.4: Schematic drawing of a high vacuum PLD chamber. A laser beam is focused through an aperture on a sintered, ceramic target and ablating molecules or molecule clusters from it. A process gas can be added to the growth atmosphere. The sample, attached to a rotating sample holder, is backside heated by a resistive heater.

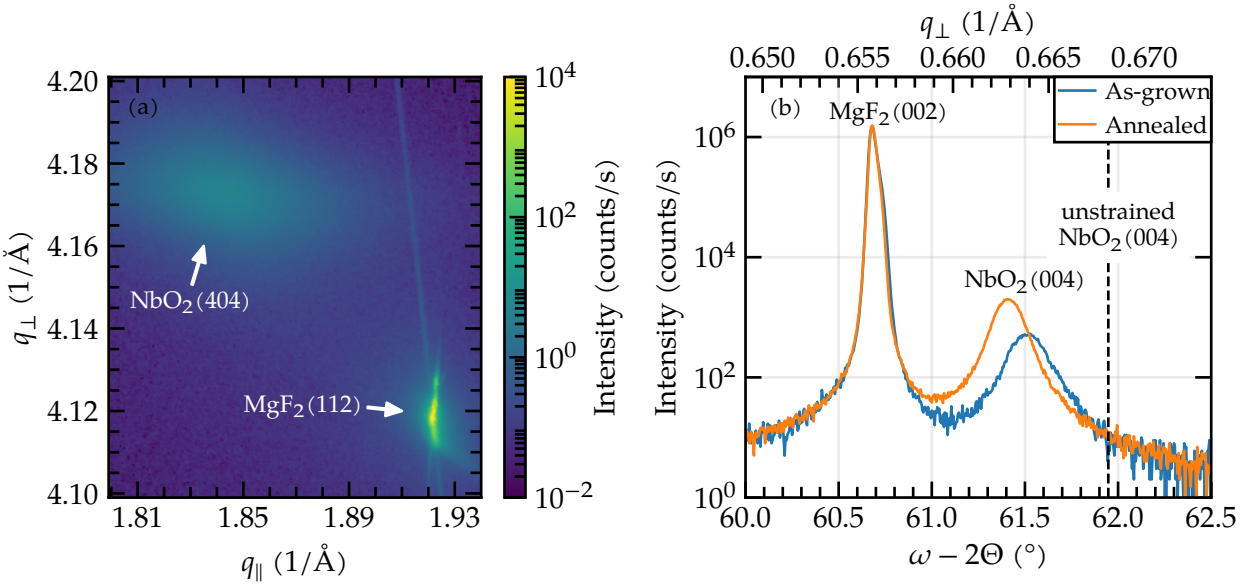

Figure 4.3: (a) The reciprocal space map around the NbO_2 (404) reflection of an as-grown sample reveals the relaxation of the layers. $q_\perp$ and $q_\parallel$ are the reciprocal lattice parameter out-of-plane and in-plane, respectively. (b) X-ray diffraction patterns around the MgF_2 (002) diffraction peak for as-grown and annealed NbO_2 samples, proving that a c-plane NbO_2 film was grown on the c-plane MgF_2 substrate. The dashed linemarks the position of the (004) diffraction peak of unstrained NbO_2. (published in reference [169])

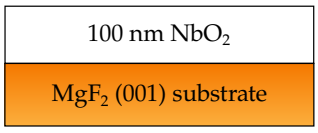

Figure 4.5: Epitaxial thin film growth with PLD of NbO_2 on MgF_2 (001) substrates.

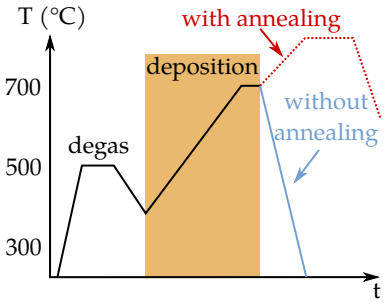

Figure 4.6: Temperature profile of NbO_2 thin film deposition with and without post-growth annealing step.

homogeneous irradiation of the target. The laser fluency is regularly checked with a flux meter and regulated by a gray filter. For this experiment, the laser fluency was set to $2\,J\,cm^{-2}$ with a pulse energy of 65 mJ/pulse. Further description of pulse laser deposition can be found in literature, e.g. in the textbook of Robert Eason.[44]

For surface preparation, the MgF_2 substrate was degassed for 1 h at 1×10^{-6} mbar and 500 °C. The substrate temperature was then decreased to 350 °C, at which the initial growth was started. The lower temperature for nucleation was chosen to prevent surface degradation. However, to improve the layer quality, the substrate temperature was increased during the deposition. Directly after starting the nucleation, the temperature was increased by a heating rate of $5\,°C\,min^{-1}$ to $10\,°C\,min^{-1}$. The final growth temperature was, depending on the sample, between 500 °C to 700 °C (figure 4.6).

The influence of a post-growth annealing step on the layer properties was investigated. For this, as-grown samples, which were cooled down at background pressure, were compared to post-growth annealed samples. The latter was heated to the annealing temperature of 880 °C directly after deposition, prior to cooldown. The annealing temperature was kept for one hour, before the sample was cooled down to room temperature at background pressure. The orientation of the NbO_2 thin film on MgF_2

	As-grown	Annealed
S_{in}	0.544 %	0.958 %
S_{out}	−0.536 %	−0.944 %
calculated $q_\perp$	0.6648 Å	0.6621 Å
measured $q_\perp$	0.6640 Å	0.6629 Å

Table 4.2: Calculated thermal strain S for NbO_2 (001) grown on MgF_2 (001) and the corresponding calculated and measured reciprocal vertical lattice parameter $q_\perp$.

(001) is (001), as it was confirmed by $\omega - 2\Theta$ x-ray diffraction scans around the MgF_2 (002) reflex (figure 4.3(b)). Reciprocal space maps around the MgF_2 (112) have shown the plastically relaxation of the thin films (figure 4.3(a)). Nevertheless, the NbO_2 (004) reflex is still shifted from the bulk lattice parameter of NbO_2, and a difference in residual strain is visible between as-grown and annealed layer. The origin of the can mainly be attributed to difference of thermal expansion coefficient between substrate and layer (table 4.1). To calculate the thermal in-plane strain S_{in}, the relation

$$S_{in} = \Delta T \cdot \left(\alpha_{MgF_2} - \alpha_{NbO_2}\right),$$

S_{in}	In-plane strain
ΔT	Temperature difference
α	Thermal expansion coefficient

can be used. The resulting in-plane strain is $S_{in,\triangle T=500K} = 0.544\,\%$ for the as-grown, and $S_{in,\triangle T=880K} = 0.958\,\%$ for the post-growth annealed NbO_2 layer. To be able to compare the thermal strain with the shift of the x-ray diffraction peak in figure 4.3(a), the out-of-plane thermal strain has to be calculated using the Poisson ratio

$$S_{out} = -\frac{2\nu}{1-\nu} \cdot S_{in}.$$

S_{in}	In plane strain
S_{out}	Out of plane strain
ν	Poisson number

ν is the Poisson number, which is not yet known for NbO_2. A rough estimate of 0.33[3,36] for the Poisson number gives an out of plane stress of $S_{out,\Delta T=500K} = -0.536\,\%$ for the as-grown and $S_{out,\Delta T=880K} = -0.944\,\%$ for the annealed layer. This stress conrresponds to a NbO_2(004) reciprocal lattice parameter of $q_{\perp,\Delta T=500K} = 0.6648/\text{Å}$ for the as-grown and $q_{\perp,\Delta T=500K} = 0.6621/\text{Å}$ for the annealed NbO_2 thin film, which are in good agreement with the measured values of $q_{\perp,as-grown} = 0.6640/\text{Å}$ for the as-grown and $q_{\perp,annealed} = 0.6629/\text{Å}$.

4.2.2 Grain properties of annealed NbO_2 layers

The as-grown and post-growth annealed layers were investigated for their surface morphologies and grain structure. The measurement by atomic force microscopy and x-ray diffraction were per-

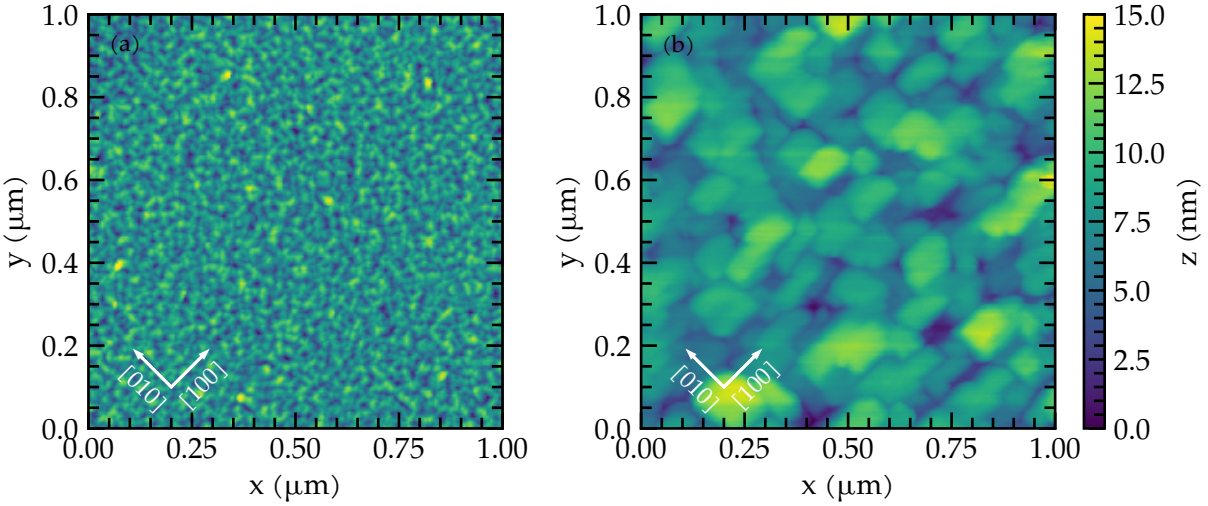

Figure 4.7: Atomic force micrographs showing the topography of $NbO_2(001)$ on $MgF_2(001)$. (a) shows an unannealed epitaxial layer of 100 nm thickness. The surface contain grains/islands of small size. In contrast, (b) shows an increased grain size after annealing for 1 h at 880 °C. (published in ref. [169])

formed by Jos E. Boschker, the analysis of the provided data were performed by myself. The data in this section was published in reference [169].

Figure 4.7 shows the atomic force micrographs of an as-grown (a) and an post-growth annealed (b) thin film. The roughness value for the as-grown layer is 2.03 nm and for the post-growth annealed layer 2.1 nm. Grains dominating both surface morphologies. The grains of the post-growth annealed sample have a flat top (RMS of the grain top surface: 0.75 nm), however, the height of the grains differs by up to 15 nm, giving the high roughness of the layer. The grains are strongly enlarged for the post-growth annealed epitaxial layer up to 60 nm compared to the as-grown layer grain size in the sub-10 nm range. The grain edges of the post-growth annealed sample show a tentative orientation along the [100] and [010] direction of the MgF_2 substrate crystal. All post-growth annealed samples show an increased grain size compared to the as-grown samples, however, no direct correlation between the growth condition and the grain size was found, which can caused by several reasons:

The growth might be sensitive on the nucleation of the epitaxial layer. Especially the nucleation density, which can be influence by the surface condition of the substrate, the substrate temperature or the target condition, might be hard to control. The substrate is glued with silver paste to the substrate holder. Small inhomogeneities in the silver glue can influence the heat transport between the sample holder and the substrate, giving a different growth or annealing temperature. Also, the growth can be influ-

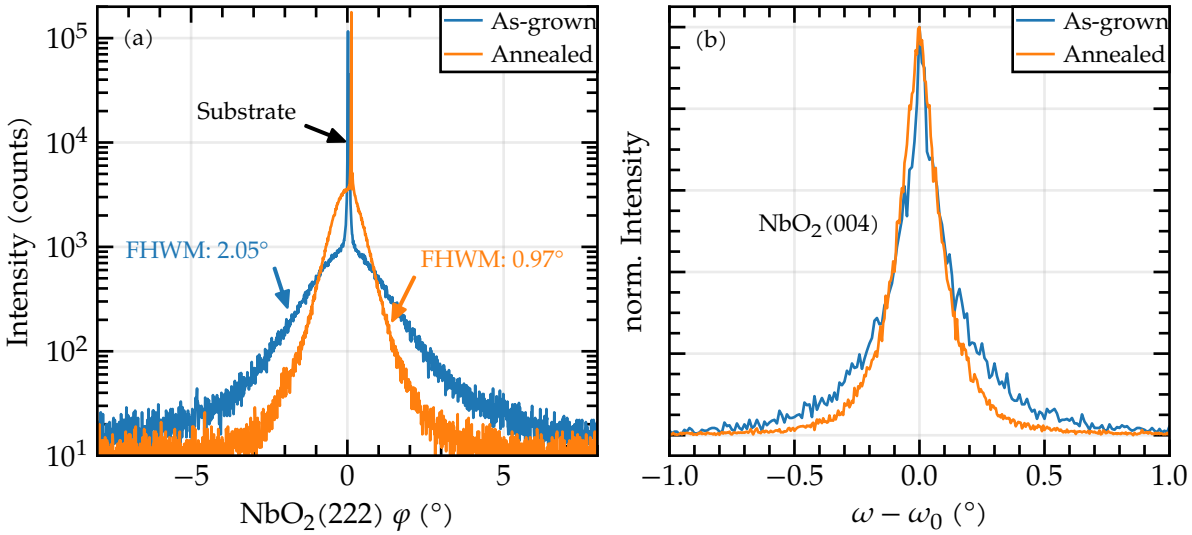

Figure 4.8: (a) Azimuthal φ-scan of the NbO_2 (222) reflex as an measurement of the in-plane misalignment of grains. The peak of the post-growth annealed sample is sharper compared to the as-grown layer, indicating smaller misalignment between the grains. (b) The rocking curves of the as-grown and post-growth annealed sample do not show a significant difference. (published in reference [169])

enced by residual gases in the vacuum, a fluctuation of the laser fluency or differences in the target composition or surface. We could not finally answer the question, which growth parameter influence the size of the grains. However, for all post-growth annealed samples, a significant increased grain size was measured.

In order to further investigate the orientation of the grains, azimuthal φ-scans around the NbO_2(222) reflex were performed. The full-width half maximum (FWHM) gives a measure for the misalignment of the grains to each other. If the orientation of the grains is not well aligned, the peak in the φ-scan will be broadened. Consequently, a well aligned grain layer will result in a sharper peak. In figure 4.8(a), azimuthal φ-scans of as-grown and annealed layers are shown. The sharp and strong peak located at 0° can be assigned to the single-crystalline MgF_2 substrate. The broad and weak feature in the vicinity of the substrate peak originates from the NbO_2 thin film. The as-grown sample shows a broad intensity profile indicating high mosaicity and small grain size. In contrast, the annealed sample shows a reduced peak width, indicating a reduced mosaicity and larger grain sizes. The rocking curves in figure 4.8(b) can give a hint for crystalline quality by estimating the dislocation density σ by[69,90]

$$\sigma \propto \frac{FWHM^2}{b^2}.$$

σ	Dislocation density
$FWHM$	Full with half maximum of rocking curve
b	Burgers vector

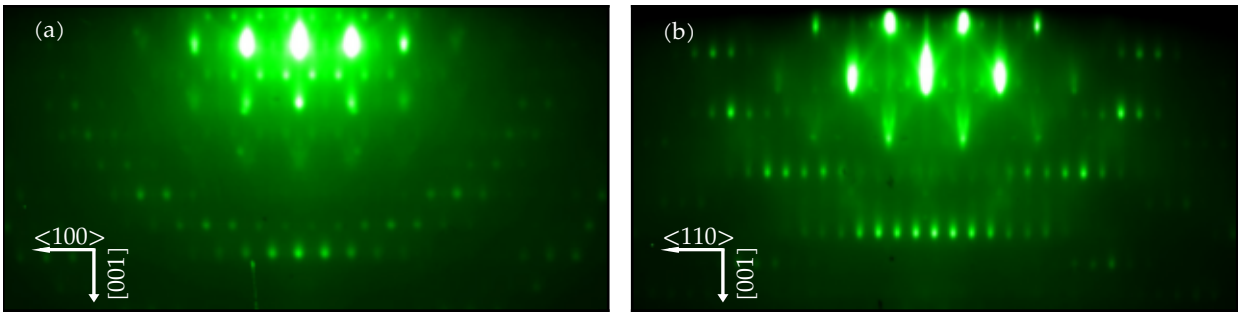

Figure 4.9: RHEED image of an post-growth annealed sample after cooldown for the <100> (a) and <110> (b) direction. Spotty RHEED transmission spots are visible as well as elongated surface diffraction spots. This is in agreement with an terraced 3D surface with transmission through the grains.

Since the *FWHM* of the as-grown and annealed layers are similar, no influences of the grain size on the dislocation density can be assumed.

Reflection high energy electron diffraction (RHEED) measurements were carried out to further confirm the orientation of the post-growth annealed epitaxial layer (figure 4.9). The RHEED pattern consist of spotty transmission spots. The central spots are elongated along the [001] direction, which is an agreement with a terraced 3D surface. This is in good agreement with the flat top grain surface measured by AFM. The pattern also proves a unidirectional in-plane orientation, as the pattern is consistent with a single-crystalline tetragonal layer.

4.3 CONDUCTIVITY IN NBO_2 EPITAXIAL LAYER

4.3.1 Resistivity of as-grown and annealed layers on MgF_2 substrates

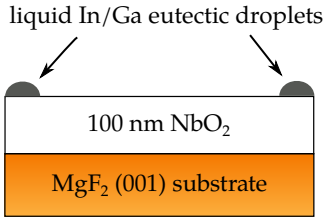

Figure 4.10: PLD-grown layers NbO_2 on MgF_2 substrates for Hall effect and resistivity measurements.

NbO_2 was grown on MgF_2. The following part was published in reference [169]. The growth process and the structural analysis can be found in chapter 4.2.

In table 4.3, the electrical properties for different epitaxial layers grown on MgF_2 are presented. No Hall effect could be measured. Hall-effect measurements require a homogeneous layer. Taking into account, that the AFM micrographs in figure 4.7 show a grainy surface morphology, it is expected that strong electron scattering at grain boundaries occur. Additionally, the requirement of a homogeneous layer is not given. Thus, further improvements of the epitaxial layers are required to determine the electron mobility and charge carrier concentration in the NbO_2 layers.

It is still possible to use the electrical measurement to optimize the epitaxial layer. From bulk crystals, a intrinsic resistivity of $10\,k\Omega\,cm$ was measured for NbO_2.[75] In contrast, epitaxial layers

Sample	T (°C)	P (mbar)	F (mJ cm^{-2})	ρ (Ω cm)	Notes
as-grown	400	0.1	70	1.1	
	500	0.02	70	0.098	
		0.1	73	0.122	
	600		65	53.7	
annealed	500	0.1	65	525	
	600			945	
	700			779	

Table 4.3: Influence of the growth parameter temperature T, pressure p and laser pulse energy P on the growth of as-grown and annealed samples. All growth processes started with the nucleation at $T = 350\,°C$ with a continuous temperature ramp to the final growth temperature T to prevent substrate degradation. All layers were around 100 nm thick by using 18 000 pulses.

reported in literature have a substantially reduced resistivity. The values range from $0.4\,\Omega$ cm to $54\,\Omega$ cm[50,79,123,191]. The origin for this additional conductivity can be caused by

- extrinsic or intrinsic donor-like point defects
- conduction paths along extended defect
- a break of dimerization in NbO_2.

In table 4.3, the resistivity values for as-grown and post-growth annealed layers are compared. Annealed thin films generally show an increased resistivity of the post-growth annealed samples over the as-grown samples. This is universal for all post-growth annealed thin films. The highest resistivity measured was $945\,\Omega$ cm it reaches 10 % of the bulk resistivity reported in literature. A significant improvement of the layer resistivity is reached, which is an important step to use the material as selector devices, since a high-resistive, normally-off state is required for sufficient current blocking.[50,79,123,191]

To investigate the influence of the post-growth annealing step, the grains size was analyzed. The grain size was determined with Gwyddion.[119] The grains were masked by the integrated watershed[12] segmentation tool. The grain area were then transformed into a circular equivalent surface area by $A = \pi d^2/4$, with A the average grain surface area, giving the equivalent grain diameter d. The equivalent grain diameter is in the following called mean grain size.

As described in section 4.2.2, there was no direct correlation between the growth parameter and the the grain size observed, pos-

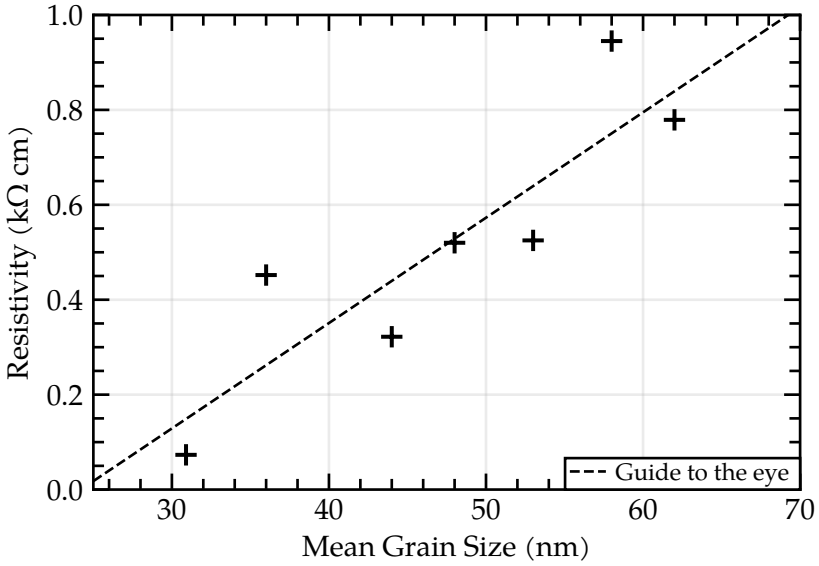

Figure 4.11: The mean grain size over the resistivity of post-growth annealed NbO_2 epitaxial layers. The grain size were determined from the AFM images. Samples having large grains also show an increased resistivity. (published in reference [169])

sibly due to sensitivity in nucleation or differences in growth temperatures. However, the thin film resistivity is correlating with the mean grain size (figure 4.11). The larger the grains, the higher the resistivity. Since there is no big difference in e.g. $\omega - 2\theta$ peak width (indicating a similar dislocation density), one explanation might be the conduction along the grain edges.

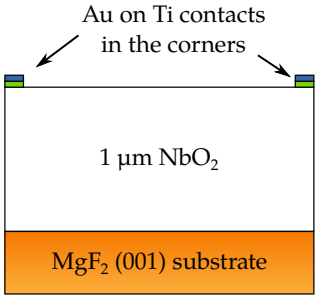

Figure 4.12: NbO_2 on MgF_2 substrates for temperature-dependent resistivity measurements.

4.3.2 Temperature dependent resistivity measurements

To obtain further information about the electrical properties of the annealed NbO_2 layer, a 1000 nm thick sample were measured in a temperature range of 165 K to 870 K. The results were published in reference [169].

In contrast to the previously discussed samples with liquid In-/Ga contacts, solid, ohmic metal contacts were deposited in order to have stable contacts over the full temperature range. 50 nm titanium, followed by 50 nm gold was deposited by electron beam evaporation through a shadow mask at the corners of the samples. The contact size was around 500 µm. The sample thickness were increased to 1000 nm to raise the upper limit of resistivity measurement to $1 \times 10^6\,\Omega\,\mathrm{cm}$, since the sample resistance is rapidly exceeding $1 \times 10^{10}\,\Omega$ at low temperatures, which is no longer accessible for a reliable measurement.

At room-temperature, the layer has a resistivity of $550\,\Omega\,\mathrm{cm}$, similar to the resistivity of the 100 nm thick sample discussed in the structural analysis part in chapter 4.2.2, indicating a thickness

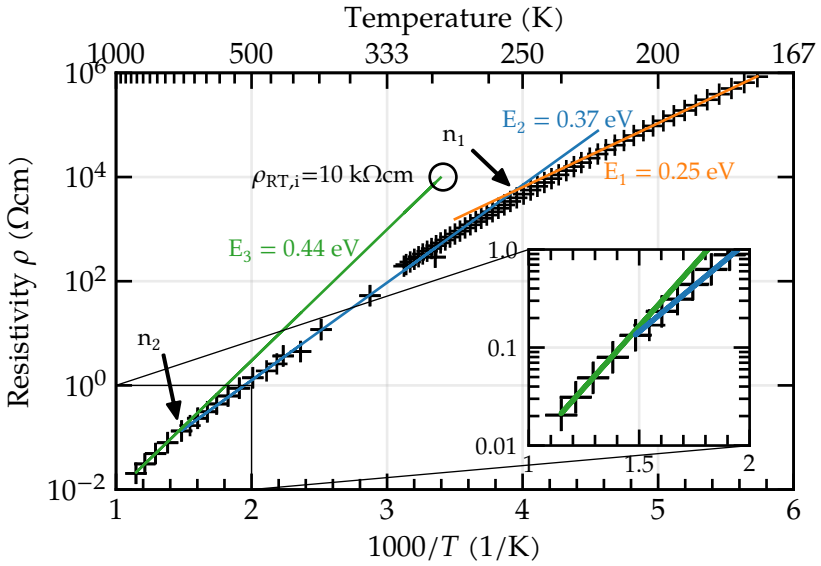

Figure 4.13: Arrhenius plot of the resistivity over the temperature. Three slopes were identified and linearly interpolated, the inset shows the magnified high temperature region. Using $\rho \propto \exp(E_i/k_BT)$, activation energies was calculated from the slopes. The high temperature slope were extrapolated to the room-temperature resistivity value. (published in ref. [169])

independent resistivity of the thin films. The sample was measured in Van-der-Pauw geometry (see chapter 3.1). Below room-temperature, the sample were measured in a DC *LakeShore Hall System* and cooled down in a closed-cycle He-refrigerator.

Above room-temperature, an AC *Fraunhofer Hall 1100K* setup was used to measure the resistivity of the sample. The sample was heated in a sealed gas chamber containing a nitrogen atmosphere with a base pressure of 700 mbar, which increased to 950 mbar at 870 K. The measurement was performed during heating and cooling of the sample. No hysteresis were found, indicating a stable sample. However, in a further heating cycle, to reach the metal-insulator transition temperature at 1060 K, a delamination of the epitaxial layer at high temperature were observed, thus, no data above 870 K is shown in the present work.

In figure 4.13, the temperature dependence of the resistivity is shown in an Arrhenius plot. At low temperatures, the resistivity is rapidly increasing to the maximum value of $10^6\,\Omega\,\mathrm{cm}$. A exponential decrease of the resistivity up to a temperature of around 250 K is visible. A second slope is visible over the temperature range of 300 K to around 650 K. An additional slope is visible above that temperature. For better visibility, the high tempera-

ρ	Resistivity
E_i	Activation energy
k_B	Boltzmann constant
T	Temperature

ture area is magnified in the inset. The graph shows thermally activated behavior over the whole temperature range. Using

$$\rho \propto \exp\left(\frac{E_i}{k_\mathrm{B}T}\right), \tag{4.1}$$

the activation energy can be calculated for each slope. The low temperature slope gives an value of $E_1 = 0.25\,\mathrm{eV}$, the mid-range temperature $E_2 = 0.37\,\mathrm{eV}$, and the high-temperature slope $E_3 = 0.44\,\mathrm{eV}$.

The activation energies $E_1 = 0.25\,\mathrm{eV}$ and $E_2 = 0.37\,\mathrm{eV}$ are interpreted as deep levels originating from defects or impurities in the semiconducting phase inside the grains. The intercepts of the Arrhenius lines can be used to perform an order-of-magnitude estimation of the defect concentration using $n = (e\mu\rho)^{-1}$ assuming a typically low carrier mobility in oxide materials of $\mu = 5\,\mathrm{cm}^2/(\mathrm{V\,s})$. The intercepts are at 250 K and 650 K. The estimated defect concentrations are $n_1 \approx 1\times10^{14}\,\mathrm{cm}^{-3}$ and $n_2 \approx 1\times10^{18}\,\mathrm{cm}^{-3}$ for E_1 and E_2, respectively.

The high-temperature resistivity decline is associated with an activation energy $E_3 = 0.44\,\mathrm{eV}$ (inset in figure 4.13). By extrapolating the high-temperature resistivity to room temperature, a resistivity of $\rho_{\mathrm{RT,i}} = 10\,\mathrm{k\Omega\,cm}$ is obtained, which is close to the reported intrinsic value by Janninck et al.[75] Thus, it is attributed to the thermal activation of intrinsic conductivity in the semiconductor and a band gap energy of twice the E_3 value can be estimated: $E_G = 0.88\,\mathrm{eV}$.

4.3.3 Percolation model for conductivity in NbO_2

The annealing step above the phase-transition temperature has significant influence on the structural and electrical data. Janninck et al. and Schäfer et al.[74,154] observed a change of stoichiometry to slightly oxygen-rich, single-phase $NbO_{2.006}$ after annealing the sample above the phase-transition temperature. Oxidation with residual oxygen in the PLD chamber could explain the strong increase of the room-temperature resistivity by reducing the number of oxygen vacancies. Another explanation, taking the increased grain size into account, is a percolation like conductivity along the grain boundaries. The low-temperature semiconducting phase is formed by the dimerization of Nb-Nb d-orbitals. A break in symmetry, like it occurs at grain boundaries, could prevent the formation of the dimers and thus leading to a highly conductive phase at the grain boundaries. In fact, only a small increase of around 0.07 Å in the Nb-Nb bond could already prevent the formation of a band gap.[187] In this case, two current paths act in parallel: One along conductive (metallic) grain boundaries, the other one through the semiconducting grains. This explains

the large difference of resistivity between the as-grown samples with small grains and the annealed ones with large grains and thus less conductive grain boundaries. Additionally, a correlation between grain size and resistivity was observed (figure 4.11). Hence, this model can explain the conduction mechanism in the samples.

This indicates, that due to annealing of the thin films and the resulting increase of grain size, the percolation conductivity along the grain boundaries can be neglected, as it would otherwise reduce resistivity and the extrapolated room-temperature value of the thermally activated conductivity would not match the reported bulk resistivity value. The band gap value is higher than the derived value corresponding to optical measurements because the activation energy E_3 may contain a (small) energy portion due to the usually decreasing mobility with increasing temperature. To avoid the latter problem, Hall effect measurements for additional determination of the carrier concentration and, in turn, the mobility would have been necessary. However, reliable Hall voltage measurements were not possible most probably because of the grain structure of the films. Nevertheless, band gap values determined from $\rho(T)$ and optical data are in reasonable agreement.

4.4 OPTICAL BAND GAP DETERMINATION

4.4.1 Spectroscopic Ellipsometry

The content of this section was published in reference [169]. The measurement was performed by Saud bin Anooz and Peter Petrik. The calculation of the dielectric function was done by Saud bin Anooz. Further analysis was performed by myself.

A Woollam M-2000DI rotating compensator ellipsometer with a spectral range of 0.73 eV to 6.48 eV was used to determine the complex dielectric function and the optical band gap within the isotropic NbO_2(001) plane. The complex reflectance ratio R of the light polarized parallel to the plane of incidence (r_p) and the perpendicularly polarized wave (r_s) is measured. It can be expressed by the amplitude ψ and the phase difference Δ with[7]

$$R = r_p/r_s = \tan(\psi)e^{i\Delta} \tag{4.2}$$

R	complex reflectance ratio
r_p	parallel polarized reflectance
r_s	perpendicularly polarized reflectance
ψ	amplitude
Δ	phase

A large angle of incidence of 70° was used for SE (see figure 4.15), providing an electric field primarily aligned in the (001) plane of the thin film, which is optically isotropic in the tetragonal crystal structure. The isotropy of the dielectric function was confirmed by rotating the sample around the [001] axis. For the evaluation of the spectroscopic ellipsometry (SE) data, a model

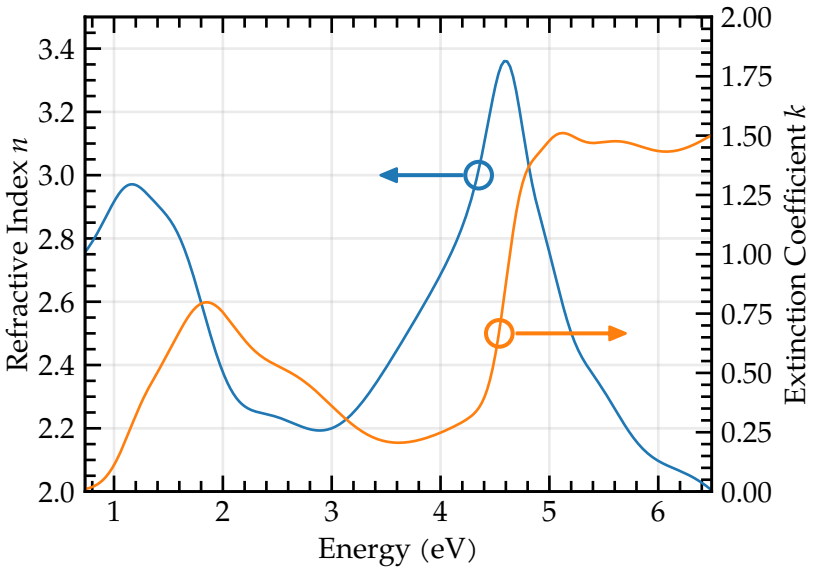

Figure 4.14: The refractive and the extinction indices of post-growth annealed NbO_2 epitaxial layers. (published in ref. [169])

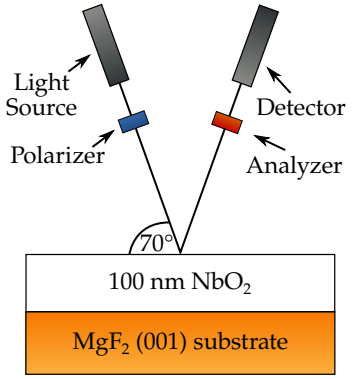

Figure 4.15: Schematic drawing of spectroscopic ellipsometry. Polarized light is reflected at the NbO_2/MgF_2 stack, which causes a change in polarization. This is analyzed by the rotating the analyzer and detecting the light intensity.

consisting of a four-component stack composed of air/surface roughness/NbO_2 thin film/MgF_2 substrate was used. The optical properties of the surface roughness layer are analyzed by a Bruggeman effective medium approximation[18] consisting of a 50 % bulk film 50 % void mixture. The amplitude ψ and phase difference Δ were fitted over the spectral range using optical dispersion models based on Gaussian type oscillators. The refractive index n and extinction coefficient k were calculated for the dielectric function of tetragonal NbO_2(001) (figure 4.14) from SE data. The features of the spectrum are similar to the ones reported by O'Hara et al.[125] The extinction coefficient was then used to analyze the absorption edge of NbO_2 using

$$\alpha = 4\pi E_{\mathrm{Ph}} k/hc \tag{4.3}$$

where α is the absorption coefficient, E_{Ph} the photon energy, c the speed of light, and h the Planck constant (see figure 4.16(b)). Using spherical parabolic band approximation at the conduction band minimum and the valence band maximum, the absorption is proportional to

$$\alpha \propto (E_{\mathrm{Ph}} - E_{\mathrm{G}} \pm E_{\mathrm{Phonon}})^2 \tag{4.4}$$

for an indirect band gap transition[207]. The band gap transition is accompanied by a momentum conserving phonon absorption or emission. By extrapolating the linear part of the plot $\alpha^{0.5}$ over the photon energy, the intercept with the x-axis gives an energy of $E_{\mathrm{Ph}} = 0.77$ eV at room-temperature.

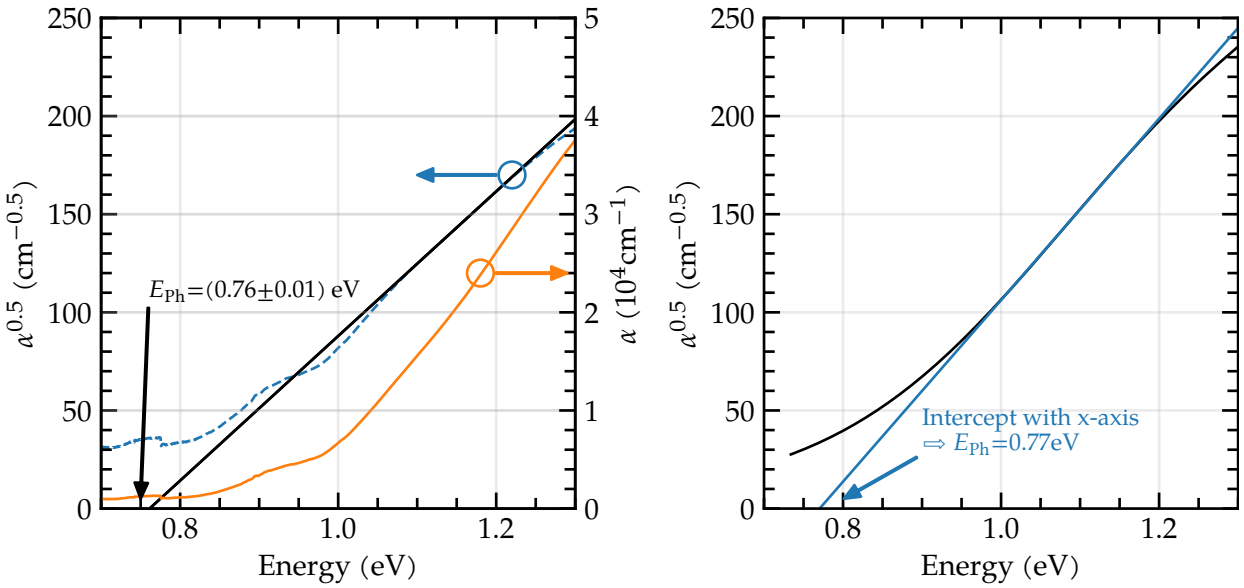

Figure 4.16: Determination of the optical band gap (a) transmission spectroscopy and (b) spectroscopic ellipsometry. In case of indirect allowed optical transitions, the band gap is absorption coefficient is proportional to the square root of the photon energy. The intercept with the x-axis give the photon energy of the transition. (published in ref. [169])

4.4.2 Absorption spectroscopy

The results from this section were published in reference [169].

Transmission spectra for NbO_2(001) deposited on MgF_2(001) substrates were measured in a double beam, double monochromator spectrophotometer (PerkinElmer Lambda 1050). The transmission spectrum was recorded in an wavelength range of 830 nm to 2500 nm respective 1.5 eV to 0.5 eV. For instrument calibration, 100 % and 0 % reference spectra were recorded. For the 100 % reference, a bare, backside polished MgF_2 substrate was put into the light beam. An internal shutter was used to block the beam for the 0 % reference spectrum. All reference and sample substrates were backside polished to suppress surface light scattering for high resolution spectra. The epitaxial layer was 1000 nm thick to provide a sufficient absorption. The incident beam was along the [001] axis corresponding to a light polarization with the electric field vector perpendicular to [001], and thus again, the absorption coefficient was measured within the isotropic (001) plane. The isotropy was checked by rotating the polarized incident wave vector and recording the corresponding

transmission spectra. No significant deviation of the spectra were measured for different polarization.

α	Absorption coefficient
d	Layer thickness
R_{ij}	Interface reflectivity i,j
T	Transmission intensity
n	Refractive index

$$\alpha = -\frac{1}{d}\ln\left(\frac{\sqrt{1-R_{01}^2(1-R_{12})^2+4T^2R_{01}R_{12}}}{2TR_{01}R_{12}} - \frac{(1-R_{01})(1-R_{12})}{2TR_{01}R_{12}}\right) \tag{4.5}$$

The reflectivity R_{ij} at an interface of the layer stack can be calculated from the refractive indices n_i with

$$R_{ij} = \frac{\left(n_i - n_j\right)^2}{\left(n_i + n_j\right)^2},$$

where $i,j = 0,1,2$ are the indices for air ($n_0 \approx 1$), the NbO_2 layer, and the MgF_2 substrate, respectively. Spectroscopic ellipsometry was used to determine the wavelength dependent refractive index for NbO_2 (see chapter 4.4.1) and MgF_2.

The absorption spectra of $NbO_2(001)$ at room temperature are shown in figure 4.14(a). The absorption coefficient could be measured up to $5 \times 10^4\,\mathrm{cm}^{-1}$. The same evaluation procedure as used for SE data was applied to determine

$$E_{\mathrm{Ph}} = E_{\mathrm{G}} \pm E_{\mathrm{Phonon}} \tag{4.6}$$

from the graph shown in figure 4.16(a). An energy of $E_{\mathrm{Ph}} = (0.76 \pm 0.01)\,\mathrm{eV}$ at room temperature was determined, which is in good agreement with the SE data.

The absorption coefficient was measured at low temperature down to 4 K. For this, a sample and a reference substrate were placed in a Oxford Instruments OptistatCF helium cryostat and cooled to 4 K. A resistance heater was used to set temperatures between 4 K to 300 K. Between each measurement, reference spectra for 100 % and 0 % calibration by measuring the reference sample or by blocking the beam was recorded, to avoid signal contributions by a temperature dependence of the absorption of the substrate or the cryostat windows. The spectral dependence of the absorption coefficient measured for temperatures between 4 K and 300 K is shown in figure 4.17. In the low temperature region, an energy $E_{\mathrm{Ph}} = (0.89 \pm 0.02)\,\mathrm{eV}$ is obtained which becomes temperature dependent above 80 K.

Density functional calculations as well as other experimental work indicate an indirect band gap of NbO_2,[125,195] which is confirmed by the $\alpha^{0.5} \propto E$ relation measured in the present work. By assuming this, the spectral temperature dependence of the absorption coefficient can be described by a single oscillator model[126,130]. Using this model, the reduction of the band

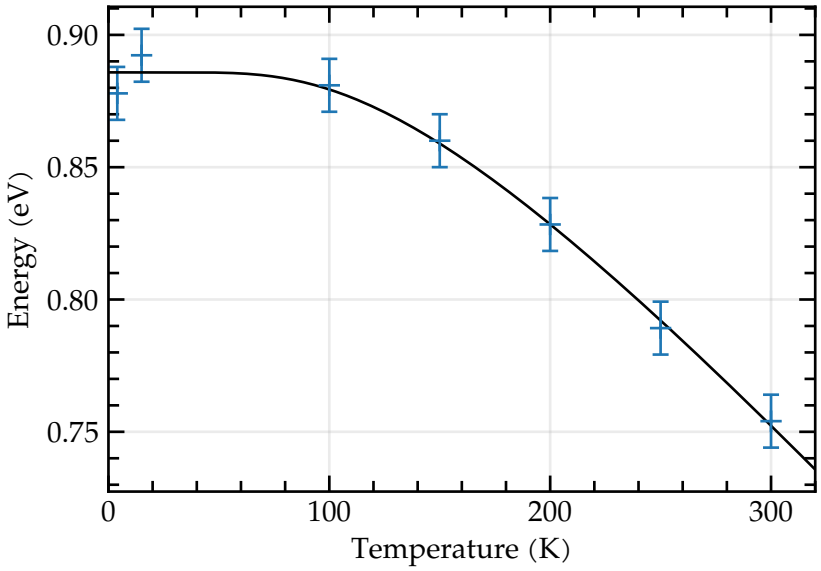

Figure 4.17: Using the method from figure 4.16, temperature dependent measurements of the optical band gap were performed. The fitted line (published in ref. [169])

gap with increasing temperatures can be reduced to an average phonon energy and a electron-phonon coupling parameter[126,130]:

$$E_{\mathrm{Ph}}(T) = E_{\mathrm{Ph}}(0\,\mathrm{K}) - S\langle\hbar\omega\rangle\coth\left(\frac{\hbar\omega}{2k_BT}\right), \tag{4.7}$$

T	Temperature
E_{Ph}	Photon energy
S	e⁻-Phonon coupling parameter
$\langle\hbar\omega\rangle$	Average phonon energy
k_B	Boltzmann constant

This gives an average phonon energy of $\langle\hbar\omega\rangle = (36 \pm 6)$ meV. In the energies determined in figure 4.17, the momentum conserving phonon has to be considered in calculating the band gap value. Since at low temperature, phonon emission is more likely than absorption, the energy has to be subtracted from the photon energy, so that we can calculate the 0 K optical band gap with $E_{\mathrm{G}} = E_{\mathrm{Ph}} - E_{\mathrm{Phonon}} = (0.85 \pm 0.03)$ eV. The coupling constant S, a measure for the electron-phonon coupling, is 5.6 ± 0.1.

The determination of the optical band gap at room temperature is more difficult, since both processes, phonon absorption, and emission can occur. We calculated an optical band gap for both, the SE and the absorption spectroscopy data to be in the range of $E_{\mathrm{G}} = (0.76 \pm 0.05)$ eV. This value lies in the center of the broad range of reported optical band gap values[2,97,136].

4.5 CONCLUSION

NbO_2 is an interesting material for metastable resistive switching applications like selector devices in memristive crossbar array devices. It's high temperature Mott-Peierls metal-insulator transition can provide temperature insensitive switching between the

two states for room-temperature applications and is thus advantageous over other materials such as VO_2. However, so far, epitaxial thin films reported in literature show a low resistivity in the low-temperature, insulating phase, preventing the material from being used in such a application.

In the present work, NbO_2 was grown hetero-epitaxially on MgF_2, since NbO_2 substrates are commercially unavailable and other substrates like TiO_2 have led to an increased conductivity of the thin films due to oxygen vacancy interdiffusion. The grown thin film shows a grainy structure. A post-growth annealing step increased the grain size from the sub-10 nm range up to 60 nm. The grains have shown a terraced surface and an reduced misalignment between the grain orientation after annealing. The rocking curves do not show a significant change in

Correlating with the grain size, the resistivity of the insulating phase could be increased by several orders of magnitude to 1 kΩ cm at room-temperature, which is only a factor of ten below the reported bulk resistivity of NbO_2. Temperature-dependent resistivity revealed two defect levels at 0.25 eV and 0.37 eV below the conduction band minimum. At high temperatures, close to the metal-insulator transition, the intrinsic resistivity of NbO_2 was measured and the band gap energy of 0.88 eV was measured. The metal-insulator transition itself could not be measured due to sample delamination at high temperatures. A model to describe the residual resistivity of the layer by a percolation conductivity along the grain boundaries was developed, which is in good agreement with the findings.

Since several values for the optical band gap were reported in literature, the band gap 0.77 eV was measured by spectroscopic ellipsometry and absorption spectroscopy. The big spread in reported band gap values in literature can be explained by lower crystal quality, since a distortion in the crystal leads to a change in the Nb-Nb dimer length, which is lowering the band gap.

Further experiments on NbO_2 are required to bring the material closer to commercial interest. Especially, a metallic bottom electrode or the growth on other resistive switching materials like $SrTiO_3$ is necessary to demonstrate the switching characteristics of the layer. Other substrates like GaN can be considered, as they are also oxygen free and more stable, enabling transmission electron microscopy investigations and higher annealing temperatures to further improve the layer quality.

5 STRONTIUM TITANATE

$SrTiO_3$ is a cubic perovskite with the space group Pm3m.[132] The semiconductor has an indirect band gap of 3.2 eV at room temperature.[88] Unlike other perovskites such as $BaTiO_3$, which exhibit ferroelectricity, $SrTiO_3$ is paraelectric at room temperature.[63] However, ferroelectricity can be induced via strains.[63] In addition, it has been shown that the Ti_{Sr} antisite defect has a permanent dipole moment and thus can also induce ferroelectricity.[26,85] A soft phonon mode in $SrTiO_3$ causes the permittivity to have a high value of 300 at room temperature and to increase up to 1×10^4 at cryogenic temperatures.[120] Superconductivity has been shown in $SrTiO_3$ at low temperatures.[4] $SrTiO_3$ single crystals are usually grown using the Verneuil growth method,[[155] but there are also single crystals grown via edge defined film-fed growth.[61,62,88] Thin films are usually grown using pulsed laser deposition (PLD)[68] or molecular beam epitaxy (MBE).[27]

Of particular interest is the possibility of creating oxygen vacancies by annealing the layer in vacuum or reducing atmospheres,[28] because oxygen vacancies are considered to be a crucial factor in resistive switching.[137] The reason is that oxygen vacancies have high mobility in $SrTiO_3$.[128] Two models for resistive switching in $SrTiO_3$ have been widely established. One is the filament model, where oxygen vacancies are created by a voltage pulse or accumulated in a filament.[171,192] Electric fields then allow the vacancies to move in the material, either breaking the filament, or reconnecting it. This results in a high-impedance or a low-impedance state.

The second model is based on the oxygen vacancies drifting to or from the electrode interface by electric fields.[54] In this case, the electrode is often made of platinum or gold, which forms a Schottky contact in $SrTiO_3$.[20,129] Due to the high concentration of vacancies, the Schottky barrier can be lowered, causing the sample to switch to the low resistive state. In the high resistive state, the vacancies drift away from the interface and the barrier energy becomes larger.

However, in this work, a new model based on the Ti_{Sr} antisite defect is developed. For this purpose, $SrTiO_3$ films grown by metal-organic vapor phase epitaxy are investigated. The concentration of the Ti_{Sr} defect in the material was controlled by changing the growth parameters. These films are first investigated for their $SrTiO_3$ dielectric properties and what influence the Ti_{Sr} defect has on these properties. In the second step, resistive switching

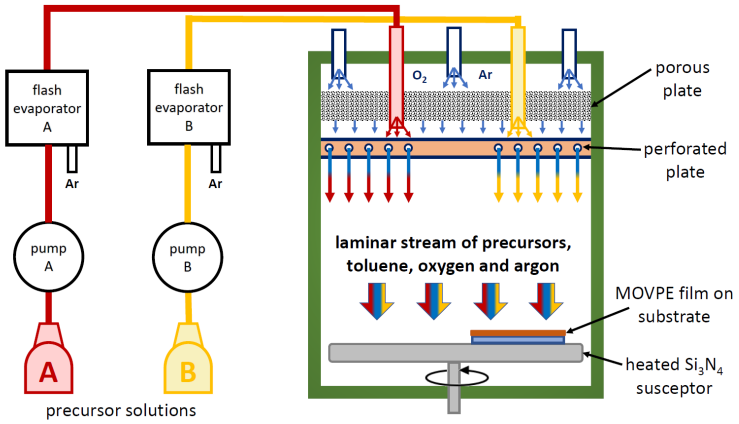

Figure 5.1: Schematic drawing of liquid delivery metal-organic vapor phase epitaxy for the deposition of $SrTiO_3$. The precursor solvent mixture is pumped via a peristaltic pump to the flash evaporator. The solution is dropped on a hot plate and evaporated. The vapor is then transferred via heated lines to the shower head reactor, where it is mixed with additional process gases. A fast spinning susceptor is used to achieve laminar gas flow in the reactor chamber. The graphic was created by Aykut Baki.

in $SrTiO_3$ is characterized and, in particular, the electrical transport through the layer is analyzed.

In the third part of this chapter, a model is developed on the basis of the knowledge gained that can explain resistive switching based on the Ti_{Sr} antisite defect.

5.1 THIN FILMS GROWN BY METAL–ORGANIC VAPOR PHASE EPITAXY

MOVPE process parameter

- **Precursor ratio:** 2.0 to 3.6
- **Precursor concentration:** 15 mmol L^{-1} in toluene
- **Vaporizer supply:** 0.5 mL min^{-1}
- **Vaporizer temperature:** 210 °C
- **O_2/Ar supply:** 5000 sccm / 1500 sccm
- **Process pressure:** 15 mbar
- **Substrate temperature:** 710 °C
- **Carrier rotation speed:** 600 rpm

Table 5.1: Growth parameter for the $SrTiO_3$ MOVPE process.

This chapter describes growth and structural characterization of the strontium titanate thin film samples investigated in the present work. The thin films were grown homoepitaxially by liquid delivery spin metal-organic vapor phase epitaxy (MOVPE).[159]

The presented results are mainly based on the work of Aykut Baki, who developed the MOVPE process and performed x-ray diffraction measurements, and of Tobias Schulz, who performed the scanning transmission electron microscopy (STEM) investigations. The presentation leans on a manuscript that was recently submitted for publication and is in the peer-review process.[8]

In figure 5.1, the system is schematically shown. The metal-organic precursors Ti(OiPr)2(tmhd)2[47] and Sr(tmhd)2 – tetraglyme[34] for titanium and strontium supply, respectively, are dissolved in dry toluene with a concentration of oxygen and water below 3 ppm. This precursor solutions are carried by two independent supply systems, consisting of a reservoir, from which the

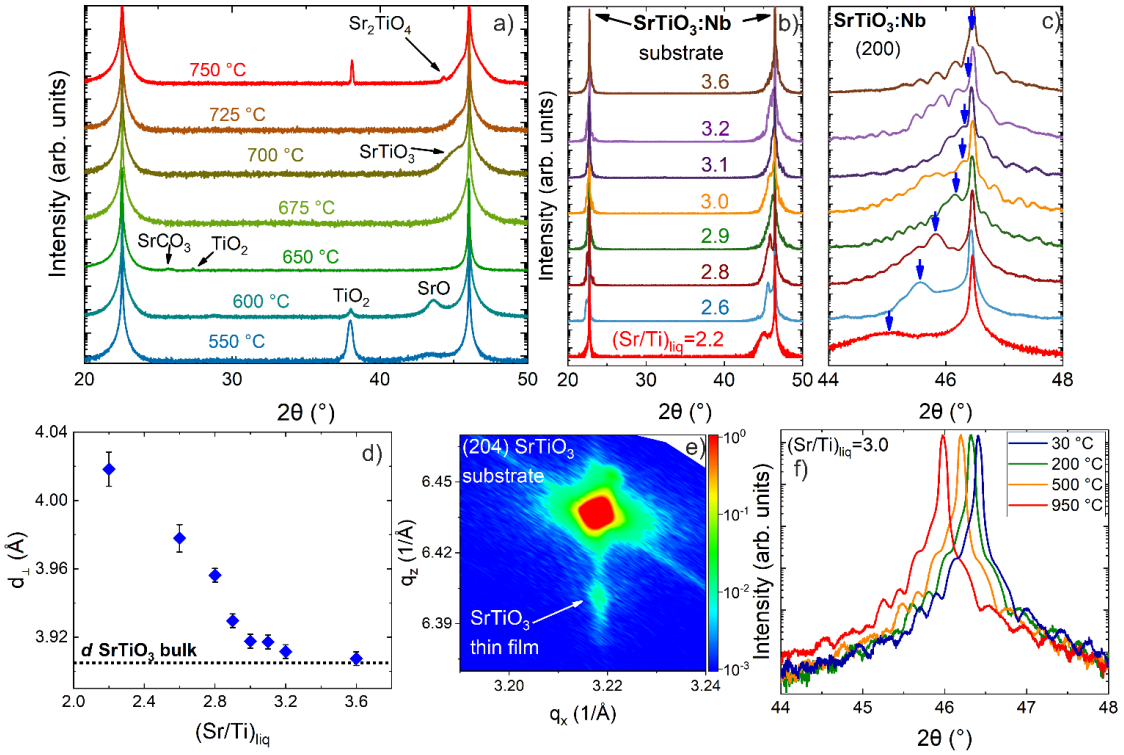

Figure 5.2: HRXRD patterns of (a) thin films grown under various substrate temperatures T_S from 550 °C to 750 °C on $DyScO_3$ (110), and (b) $SrTiO_3$ films grown with various precursors concentration ratios in the liquid sources $(Sr/Ti)_{liq}$ grown on $SrTiO_3$:Nb (100) in a 2θ range between 20° to 50°. (c) The same HRXRD scans from (b) with higher magnification in the vicinity of the $SrTiO_3$:Nb (200) substrate peak (the film peak position is illustrated by blue arrows) with increasing $(Sr/Ti)_{liq}$. (d) Vertical lattice parameter $d_\perp$ as a function of $(Sr/Ti)_{liq}$. (e) Reciprocal space maps of the films with $(Sr/Ti)_{liq} = 2.6$ in the vicinity of the (204) Bragg peak of bulk $SrTiO_3$. (f) In-situ HRXRD patterns at different temperature of post-annealed $SrTiO_3$ sample with $(Sr/Ti)_{liq} = 3.0$ in pure oxygen at ambient pressure up to 950 °C. (figure including description taken from Baki et al.[8])

solutions are transferred by peristaltic pumps to the flash evaporators. The flash evaporation systems vaporize the solutions by facing them in form of micro droplets onto a hot plate with a vaporization temperature of 210 °C. To avoid condensation and ensure a constant vapor pressure through the whole supply chain, the vapor is further transferred by heated lines to the shower head reactor by application of an argon push gas.

The shower head consist of two gas mixing chambers. In the upper one process gases, in this case oxygen and argon, are supplied with a flow of 5000 sccm and 1500 sccm, respectively. To provide a homogeneous mixture, the gases are pushed through a porous plate to the bottom mixing chamber, where the precursor/toluene supply lines are injected. The final gas mixture is then introduced to the growth chamber by a shower head.

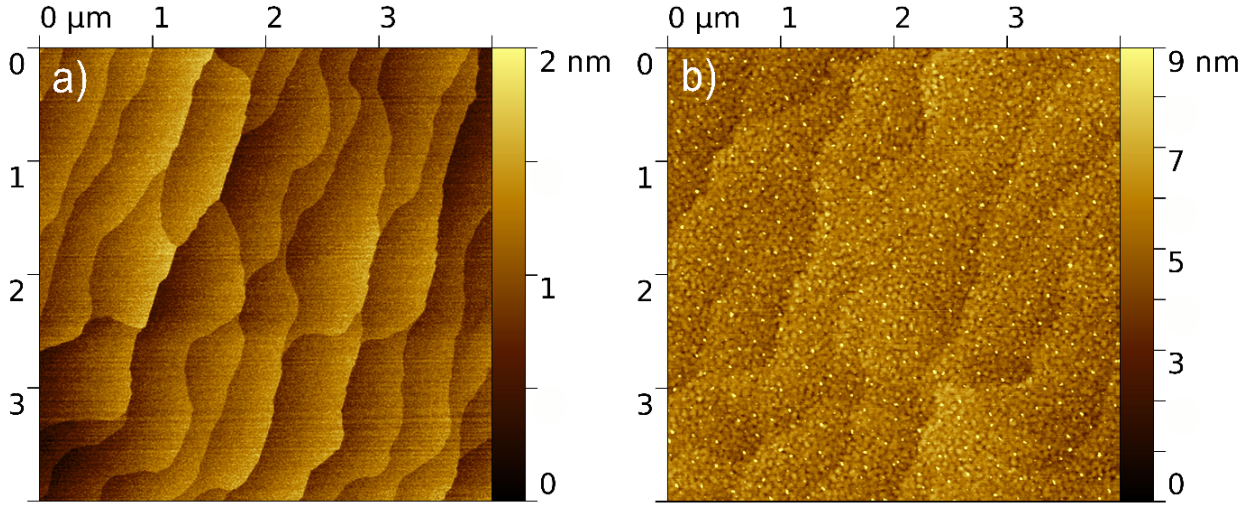

Figure 5.3: AFM image of (a) pre-deposited $SrTiO_3$:Nb substrate after etching and annealing (roughness is 0.4 nm) (b) $SrTiO_3$ thin film on $SrTiO_3$:Nb substrate with $(Sr/Ti)_{liq} = 3.2$ annealing (roughness 0.6 nm). (Measurement by Aykut Baki)

In the growth chamber, the substrates are placed on a heated, fast spinning susceptor to provide a laminar flow, which ensures a homogeneous supply of the precursor process gas mixture and the formation of a homogeneous supersaturation region close to the substrates surface. Onwards, the chamber pressure p was kept at 15 mbar over the whole process. In order to determine the appropriate substrate growth temperature (T_S) for achieving single-phase $SrTiO_3$ growth, depositions were performed from 550 °C to 750 °C. Figure 5.2(a) shows HRXRD $2\theta - \omega$ scans of samples grown under various T_S.

For growth temperatures below 675 °C, additional Bragg reflection peaks attributed to the single oxide contributions of TiO_2 and SrO are observed.[29,176] Additionally, $SrCO_3$ is formed at 650 °C.[189] At a temperature of 750 °C and above additional Ruddlesden-Popper (RP) phases like Sr_2TiO_4 and the TiO_2 phase are present. From 675 °C to 725 °C, single-phase $SrTiO_3$ with (100) surface orientation was observed. This temperature dependence of phase formation agrees with literature data and is reasoned by the standard formation enthalpies.[156] In order to obtain single-phase $SrTiO_3$ without the formation of single oxides, carbonates, and RP phases, T_S should be adjusted in the range of 675 °C to 725 °C, however was kept constant at 710 °C for all following thin films of $SrTiO_3$. An overview over the applied main process parameters for single-phase $SrTiO_3$ is given in table 5.1.

With this parameter set on hand, the growth was performed on $SrTiO_3$:Nb substrates with a (100) orientation and an off-cut of 0.1 % along the [001] direction and a doping level of 0.5 wt. % or 1.5×10^{20} cm^{-3}. Prior to growth, the $SrTiO_3$ substrates were etched in buffered hydrofluoric acid solution and subsequently

annealed in pure oxygen at 1100 °C for one hour. Atomic force microscopy images showed a terraced surface with terraces of 200 nm width and a step height of one unit cell (4 Å) as shown in figure 5.3. The surface was TiO_2 terminated.

Unlike other methods used for deposition of epitaxial $SrTiO_3$, e.g. molecular beam epitaxy or pulsed laser deposition, MOVPE processes are performed close to thermodynamic equilibrium. The chemical potential can be controlled by numerous parameters like supply rate of precursor, pressure or temperature and thus, the intrinsic defect formation, like cation vacancies, V_O or the Ti_{Sr} defect can be controlled by varying the supply ratios of the precursor and the oxygen.

After establishing a stable growth window, in which phase pure, single crystalline $SrTiO_3$ was grown homoepitaxially with a smooth surface on the $SrTiO_3$:Nb substrates (compare figure 5.3(b)), a special interest was put on the precursor concentration ratio. The ratio for the precursor concentration in the toluene was varied between 2.2 and 3.6 with keeping the total concentration at 15 mmol L^{-1}.

High resolution x-ray diffraction patterns were taken to analyze the thin films for foreign phases and off-stoichiometry. Figure 5.2(b) shows a 2θ-scan over a broad scanning range to identify peak signals from foreign phases. For all precursor ratios, the thin films were phase-pure $SrTiO_3$. Figure 5.2(c) shows the $SrTiO_3$:Nb (200) reflexes and hence the deviation of the layer peak from the bulk substrate peak. For low precursor ratios, the peak shift is strong and getting weaker for higher ratios. For a ratio of 3.6, the peak is coinciding with the substrate peak. The HRXRD profile was simulated with a multilayer model (exemplarily shown in figure 5.2(b, c)). Multiple layers were needed to achieve a sufficient agreement between measurement and simulation, indicating an inhomogeneous defect distribution for the off-stoichiometric samples. Only samples close to stoichiometry could be simulated with a single layer model and are homogeneous in structure. In order to exhibit the inhomogeneity in defect distribution STEM images with varying camera length were taken.

Figure 5.4(a) and (b) shows two exemplary STEM ADF images of an off-stoichiometric sample with $(Sr/Ti)_{liq} = 3.2$ acquired in the same region of the sample for two different camera lengths of 130 mm and 300 mm, respectively. The shorter camera length of 130 mm corresponds to HAADF conditions, which makes image intensity mainly sensitive to atomic mass contrast (Z-contrast). On contrary, a higher camera length of 300 mm corresponds to low angle annular dark field (LAADF) conditions, and indicate local lattice distortions. For both imaging conditions, the MOVPE layer becomes distinguishable by means of a contrast change with respect to the $SrTiO_3$ substrate, confirming the presence of atomic

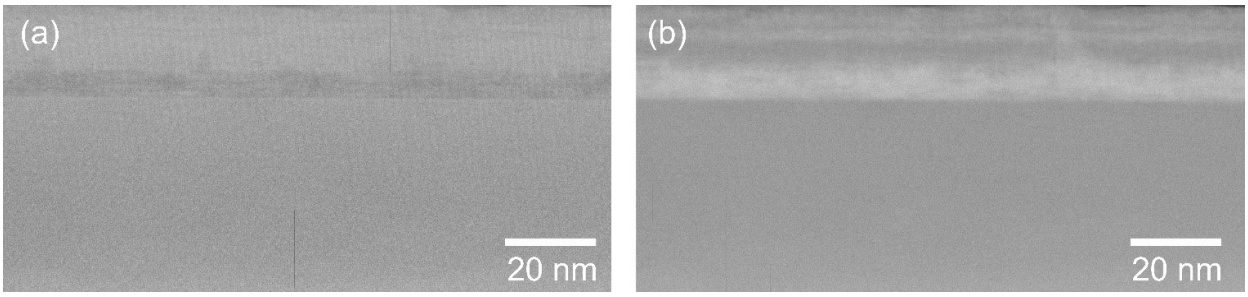

Figure 5.4: STEM LAADF and HAADF images of an off-stoichiometric $SrTiO_3$ layer with $(Sr/Ti)_{liq} = 3.2$ for camera lengths of (a) 130 mm (HAADF) and (b) 300 mm (LAADF). Measurements and graphics by Tobias Schulz

defects within the layer. In detail, off-stoichiometric layers generally appear darker for HAADF conditions, implying a lower atomic mass density as compared to the stoichiometric substrate. Vice versa, the brighter intensity under LAADF conditions suggests that these underlying defects additionally cause strong lattice distortions. Notably, the contrast in the MOVPE layer and thus the underlying defect distribution is inhomogeneous, particularly along the growth direction. The reason for this inhomogeneous defect distribution within the layer is the strong sensitivity of $SrTiO_3$ growth towards small changes in growth parameters, which is discussed in reference [8]. Inhomogeneities explain the irregularities in oscillations of the HRXRD patterns.

Cation vacancies lead to a local lattice expansion in $SrTiO_3$ due to repulsive coulomb forces.[87,179] This further leads to the deviation of the layer peak to the substrate peak and allows to use this shift as an estimation for the off-stoichiometry. Figure 5.2(d) therefore shows the deviation of the vertical lattice parameter in comparison to the bulk value for the different precursor concentration ratios. The off-stoichiometry determination by considering the HRXRD peak shift is only qualitative. The accuracy of this method is not very high and even thin films which have a lattice parameter like the bulk crystals can show deviations in the range of percent from stoichiometric Sr/Ti ratio.

As a next step, three samples grown with different precursor concentration ratios of 2.6, 3.2 and 3.6 were investigated with transmission electron spectroscopy. In figure 5.5, STEM high angle annular dark field (HAADF) images of these samples are shown. The off-stoichiometric thin films in (a) and (b) appear darker than the substrate, which can be explained with a lower mass density in the thin film, which agrees with the growth conditions and the HRXRD observations, suggesting a strontium deficiency in the thin films. Recent investigations by Tobias Schulz and Houari Amari by performing DFT calculations and STEM electron energy loss spectroscopy indicated, that also Ti_{Sr} anti-

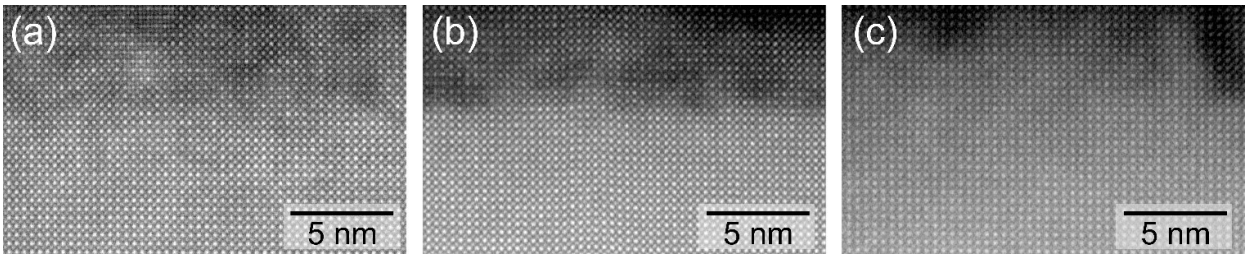

Figure 5.5: STEM high-angle annular dark-field images for precursor supply ratios $(Sr/Ti)_{liq}$ of 2.6 (a), 3.2. and 3.6 (c). (a) is a strongly off-stoichiometric film and (c) a nearly stoichiometric one. The thin film with a stoichiometric composition is more homogeneous with less diffuse scattering. Measurements and graphics by Tobias Schulz.

site defects exists in the layer. The Ti_{Sr} defect recently gained increased interest and is claimed to be abundant.[26,80,85,101] This defect will play an important role in interpreting the permittivity and resistive switching data.

For thin films closer to stoichiometry, these 1D defects were not observed. The findings are in well agreement with the HRXRD data, especially with the multilayer simulations of the HRXRD pattern of off-stoichiometric samples. For the stoichiometric sample with a precursor ratio of 3.6, the STEM-HAADF image appear homogeneous and again in good agreement with the single-layer model used for simulating the HRXRD pattern.

Concluding, it was successfully shown that single-crystalline and phase pure $SrTiO_3$ thin films can be grown with liquid delivery spin MOVPE and that the amount of cation defects can be controlled by changing the precursors concentration ratio. The formation of the defects was not homogeneous, probably due to instable growth conditions and strong sensitivity on the change of growth parameter. However, for (nearly) stoichiometric samples, a homogeneous layers were grown, which was confirmed by HRXRD and STEM-HAADF. Of particular interest for further investigation is the Ti_{Sr} antisite defect, which is likely present in high concentrations in these thin films.

5.2 EXPERIMENTAL CHARACTERIZATION OF THE PERMITTIVITY

The dielectric properties of $SrTiO_3$ strongly depend on the chosen material and are influenced by deviations of stoichiometry or defects. In this chapter, first an literature overview of the applied models on the dielectric constant of $SrTiO_3$ is given. Subsequently, the dielectric properties of bulk crystals and thin films grown with PLD are discussed. Finally, it is shown that the dielectric properties in MOVPE grown $SrTiO_3$ thin films strongly

deviate from the known properties of bulk crystals and PLD films, which is due to induced ferroelectricity by the Ti_{Sr} defect.

At room-temperature, a permittivity of around 300, but values between 43 to around 1000 are reported.[16,56,100,152,203] The range of reported values indicates the sensitivity of the permittivity in $SrTiO_3$ on various parameters like strain, deviations from stoichiometry or point defects. Neville et al. have measured the temperature dependence of the permittivity ϵ_r in $SrTiO_3$ in 1972.[120] They found an increase of ϵ_r from 330 at room-temperature to 30 000 at 4 K, as well as an field-dependence of the permittivity below 65 K, which they relates to a tetragonal to orthorhombic phase transition.[102] The dependence of the temperature was described in terms of an electrically active optical phonon[120] and by the Curie-Weiss-Law (reference [84, pp. 467-474]). Above 35 K to 40 K, the permittivity follows the Curie-Weiss-Law[120,153,194]

$\epsilon_r(0)$	static relative permittivity
$\epsilon(\infty)$	optical relative permittivity
ω_{TO}	Transversal optical phonon frequency
ω_{LO}	Longitudinal optical phonon frequency
A	Curie constant
T	Temperature
T_0	Phase-transition temperature

$$\epsilon_r = \frac{A}{T - T_0}. \tag{5.1}$$

The Lyddane-Sachs-Teller relation

$$\epsilon_r(0)\omega_{TO}^2 = \epsilon_r(\infty)\omega_{LO}^2, \tag{5.2}$$

sets the permittivity in relation with the optical phonon frequencies. The dynamic permittivity and the longitudinal optical phonon are insensitive to the change of temperature,[120,180] which means, that the transversal optical phonon must be temperature dependent, and even more, vanishes at T_0 due to

$$\omega_{TO}^2 \propto T - T_0. \tag{5.3}$$

The frequency of the product of the permittivity and the square transverse optical phonon was found to be

$$\epsilon_r(0)\omega_{TO}^2 = (9.65 \pm 0.30) \times 10^{28}\ \mathrm{s}^{-2} \tag{5.4}$$

by Neville et al.[120] and the shift and vanishing of the phonon mode was confirmed by neutron scattering experiments of Cowley.[30] The vanishing of the phonon mode, so called soft phonon mode, should lead to a ferroelectric phase transition of the crystal. However, near the phase transition temperature T_0, the permittivity deviates from the Curie-Weiss law and there is no ferroelectric phase transition in strain-free $SrTiO_3$. Barrett[9] used a mean-field approach to describe the deviation from the Curie-Weiss-Law by using

ϵ_r	static relative permittivity
A	Curie constant
T	Temperature
T_0	Curie temperature
T_1	Temperature, at which the deviation from Curie-Weiss law begins

$$\epsilon_r = \frac{A}{\frac{T_1}{2}\coth\left(\frac{T_1}{2T}\right) - T_0}, \tag{5.5}$$

which was confirmed for ferroelectric materials like $BaTiO_3$. However, in the case of $SrTiO_3$, the permittivity of the low-temperature

regime is underestimated by Barrett's formula and the expected ferroelectric phase transition was not observed. Müller et al.[114] found, that quantum fluctuations can suppress a ferroelectric phase transition, if the ferroelectric displacement Δz of the ion (in $SrTiO_3$: Ti) is smaller than the amplitude of the quantum fluctuation $\overline{\Delta}z$. The value for the Ti displacement in $SrTiO_3$ is $\Delta z = 0.045$ Å[1,91] and with $\overline{\Delta}z = 0.077$ Å[114] this condition is fulfilled. $SrTiO_3$ is therefore an intrinsic quantum paraelectric.[114] The quantum mechanical suppression mainly occurs in undistorted single-crystalline $SrTiO_3$ and can be easily prevented by crystal distortions or defects. It was even shown, that even exchanging ^{16}O by ^{18}O leads to a low temperature ferroelectricity with the Curie temperature at 38 K.[72] Biaxial strain in heteroepitaxially grown thin films results in a tetragonal distortion that is strong enough to stabilize ferroelectricity. Strain allows tuning the Curie temperature by[39,63]

ΔT_C	Shift in Curie temperature
κ	Biaxial strain
ϵ_0	vacuum permittivity
C	Curie constant
Q_{ij}	electrostrictive coefficient
s_{ij}	elastic coefficient

$$\Delta T_C = 2\kappa\epsilon_0 C\frac{Q_{11}+Q_{12}}{s_{11}+s_{12}}, \tag{5.6}$$

By using a $DyScO_3$ substrate, inducing 1 % biaxial strain into a 50 nm thin film grown by molecular beam epitaxy, the Curie temperature could be increased to $T_C = 293$ K and ferroelectricity was demonstrated.[63,201] Another way to enable ferroelectricity at low temperatures and thus change the temperature slope of the permittivity is inducing an off-stoichiometry by growing an either Sr-deficient or Ti-deficient thin films.[174]

A short overview about the work on field-dependence of the permittivity in $SrTiO_3$ will be given in the following, detailed description by introducing the Landau-Ginzburg theory is described in chapter 2.2.2. The Landau-Ginzburg theory was originally developed to describe superconductivity[59] and was later adapted to ferroelectric systems.[38,39,113] The general approach in describing the field dependence of ferroelectrics by expanding the free energy F by its order parameter P, the polarization,[23,145,202] to

$$F = F_0 + \frac{\chi}{2}P^2 + \frac{\xi}{4}P^4 - EP \tag{5.7}$$

and minimizing it, $\delta F/\delta P = 0$, which gives a relation between field and polarization:

$$E = \chi P + \xi P^3. \tag{5.8}$$

χ directly gives the susceptibility of the crystal, ξ is the non-linear dielectric response of the thin film. Different approaches were presented by finding the solution for $\epsilon_r(E,T)$.[107,145,204,205] In the present work, the approach of Yamamoto et al. is used, a detailed description is found in chapter 2.2.2. For the field-dependence, formula 2.32 is used.

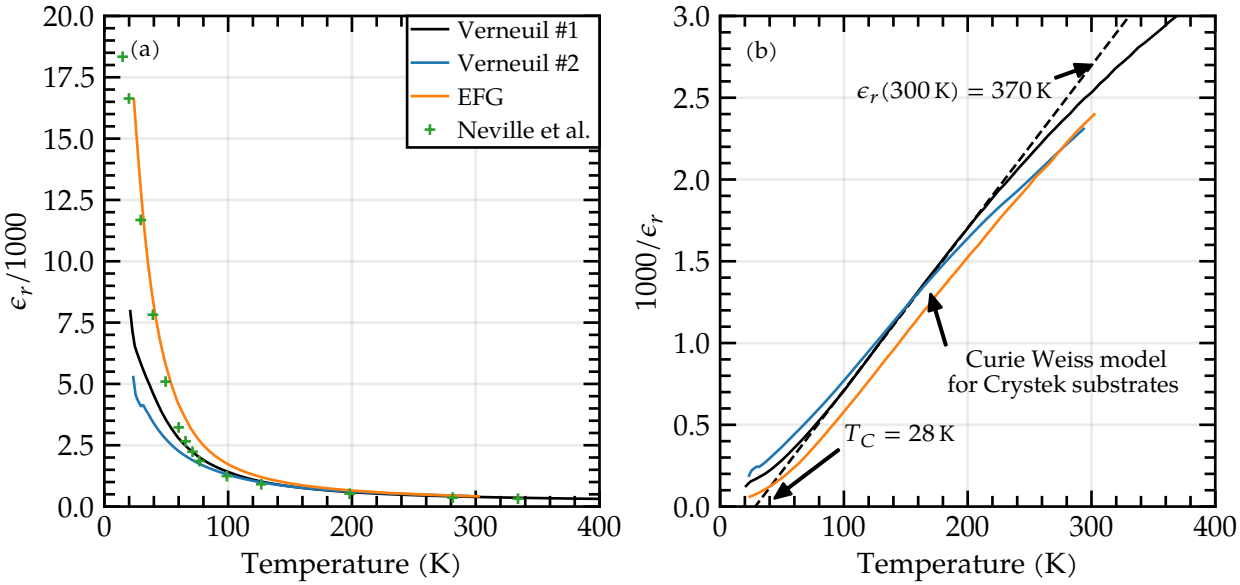

Figure 5.7: (a) Permittivity of different substrates over the temperatures compared to literature values,[120] measured in a plate capacitor setup. Only the EFG substrates reaches as high values as the reference at low temperatures. (b) The reciprocal permittivity shows a linear increase with temperature, as it is expected from equation 5.1. However, the Verneuil grown samples show a deviation to high permittivity values at room temperature. The Verneuil #1 substrate, which is used in this study, shows a Curie temperature of 28 K and a (interpolated) room-temperature permittivity of 330, which is in agreement with literature values.[120]

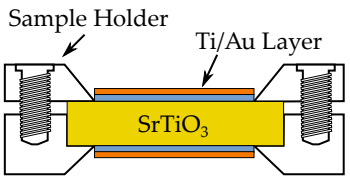

Figure 5.6: Plate capacitor structures based on $SrTiO_3$ single-crystal substrates. To get concentrically oriented contacts for a homogeneous electric field inside the substrate, a special clamping shadow mask was used. The sample is clamped in the holder. In a two step process, both sides of the substrate were deposited with 50 nm titanium and 50 nm gold.

5.2.1 Bulk single crystals

The dielectric constant for $SrTiO_3$ bulk single-crystals were measured in a plate capacitor setup and compared with literature reports (e.g. Neville et al.[120]) The dielectric properties of three single-crystals of different origin were compared:

1. Verneuil grown single-crystal (CrysTec GmbH[32])
2. Verneuil grown single-crystal (Crystal GmbH[31])
3. Edge-defined film-fed grown single-crystals (by Guguschev et al.[61])

Details about the crystal growth methods can be found in reference [155] for Verneuil growth and in references [61, 62, 88] for edge-defined film-fed growth. All crystals were (001)-oriented and chemically-mechanically polished. The thickness is given in table 5.2. All crystals were unintentionally doped and electrically insulating. Ti/Au contacts were used for the plate capacitor structure, to have flat conduction and valence bands at the interfaces. This gives the risk of oxygen interdiffusion between the electrode and $SrTiO_3$. However, no indication of oxygen vacancy formation by e.g. leakage current was detected. Additionally, gold is used as a second layer to prevent electrode oxidation, but is providing a second functionality. Even if a conductive $TiO_{2-\delta}$–$SrTiO_{3-\delta}$

Substrate	t (μm)	A (K)	T_C (K)	$\epsilon_r(T = 300\,\mathrm{K})$	$\epsilon_r(T = 20\,\mathrm{K})$
Neville et al.[120]		9.5×10^5	30	330	16 070
Verneuil #1 (CrysTec)	400	10.1×10^5	28	394	7965
Verneuil #2 (Crystal)	500	11.3×10^5	12	432	5277
EFG (IKZ)	750	10.5×10^5	38	416	16 588

Table 5.2: Three different types of substrates were compared, two commercial Verneuil grown substrates and an in-house grown EFG substrate. All substrates have comparable thickness t. Both Verneuil substrates show a too low permittivity ϵ_r compared to values reported by Neville et al.,[120] as well as a comparably low Curie temperature T_C.[114] In figure 5.7 is also a deviation from the Curie-Weiss law visible. EFG substrates, grown at IKZ, show Curie-Weiss behaviour up to room-temperature and the permittivity and Cure temperature values are comparably to literature.

exist, the band bending through the high work function of gold would form a space charge region, which would prevent the existence of free charge carriers near the interface. Thus the choice of electrode material is uncritical for the given sample structure. Titanium of 50 nmthickness was deposited by electron beam evaporation, followed by a 50 nm gold layer. A sample holder for electrode deposition through a shadow mask was designed and built (figure 5.6). The holder has a cavity to position the sample. A plate is put on the top side of the holder and fixed by a screw, so that the sample is thightly clamped between the holder and top plate. The holder and top plate have 3 mm circular holes, which are concentrically oriented to each other after mounting the plate on the holder. Using this holder, it is ensured to deposited two concentrically oriented electrodes of the same size on the front and the back of the sample. The permittivity over temperature curves are shown in figure 5.7 and were compared to literature values. The permittivity at low temperature is by a factor of 3 to 4 lower for the commercial, Verneuil grown substrates compared to the literature value. Only the edge-defined film-fed grown sample reaches similar values. In figure 5.7(b), the reciprocal permittivity is shown over temperature to confirm the Curie-Weiss behavior and the deviation from it at low temperature due to quantum fluctuations. All samples show a Curie temperature in the expected temperature range (table 5.2). However, the Verneuil grown samples show a deviation from the expected $\epsilon_r^{-1} \propto T$ slope at room-temperature.

The difference might come from the crystal growth method. Verneuil growth uses a hydrogen-oxygen flame to heat the material above melting point. The material is dropping from a reservoir on a seed crystal, where it's crystallizes. This can influence the crystals in two ways. Hydrogen can be incorporated into the crystal and large temperature gradients - a hot, molten droplet is

falling on the solid crystal - can occur, which can lead to high dislocation densities. Edge-defined film-fed growth is, analogously to Czochralski growth, pulling the crystal from a melt, with lower temperature gradients and thus lower dislocations. This can lead to the improved dielectric behavior at low temperatures.

Since all further investigations were performed on Verneuil substrates obtained from CrysTec GmbH (Verneuil #1), the linear regression of the Curie-Weiss slope is shown in figure 5.7(b). The interpolated value of the permittivity at room-temperature matches well the literature value of around 300 to 330,[120] however, the measured value is slightly higher at 400.

5.2.2 Permittivity in thick PLD grown $SrTiO_3$ layers

In the next step, the permittivity was measured on a PLD grown film of 1 µm thickness on a 0.5 wt. % niobium doped $SrTiO_3$. The substrate was heated in vacuum with a pressure below 1×10^{-6} mbar to 800 °C prior to deposition to remove the topmost TiO_x layer and get a SrO termination. For the growth in 1×10^{-1} mbar O_2 atmosphere, the temperature was reduced to 600 °C. The laser fluency was 2.2 J cm^{-2}. 25 000 pulses were needed to deposited 1 µm $SrTiO_3$ at a pulse frequency of 5 Hz. The distance between $SrTiO_3$ target and substrate was 61.5 mm. TEM investigations were performed on comparable thin films of 50 nm thickness, which were grown with the same growth parameter. No difference in contrast between substrate and layer was observed in high angular dark field TEM, and no of diffuse scattering was measured, which can indicate a low point defect density (see chapter 5.1). Thus it can be assumed that also the thick layers have a similar quality, however, changes in e.g. the target which might influence the layer quality can't be excluded. Platinum contacts with diameter of 150 µm, 200 µm and 300 µm and a thickness of 50 nm were deposited by electron beam evaporation through a shadow mask.

In the first step, the layer permittivity of $\epsilon_r = 259$ was determined by measuring the capacitance and using the plate capacitor equation

$$\epsilon_r = \frac{cd}{\epsilon_0}. \tag{5.9}$$

c	specific capacitance per area
ϵ_r	relative permittivity
ϵ_0	vacuum permittivity
d	thickness of dielectric

In figure 5.8(a) is the field dependence up to 1 MV cm^{-1} shown and the Landau-Ginzburg model was fitted to the data. The field dependence at room-temperature is following the Landau-Ginzburg model of non-linear dielectric response of the polarization on the electric field with the non-linearity factor ξ (equation 2.32).

Figure 5.8(b) shows the leakage current through the layer. Only for negative bias, a current is measurable, for positive bias,

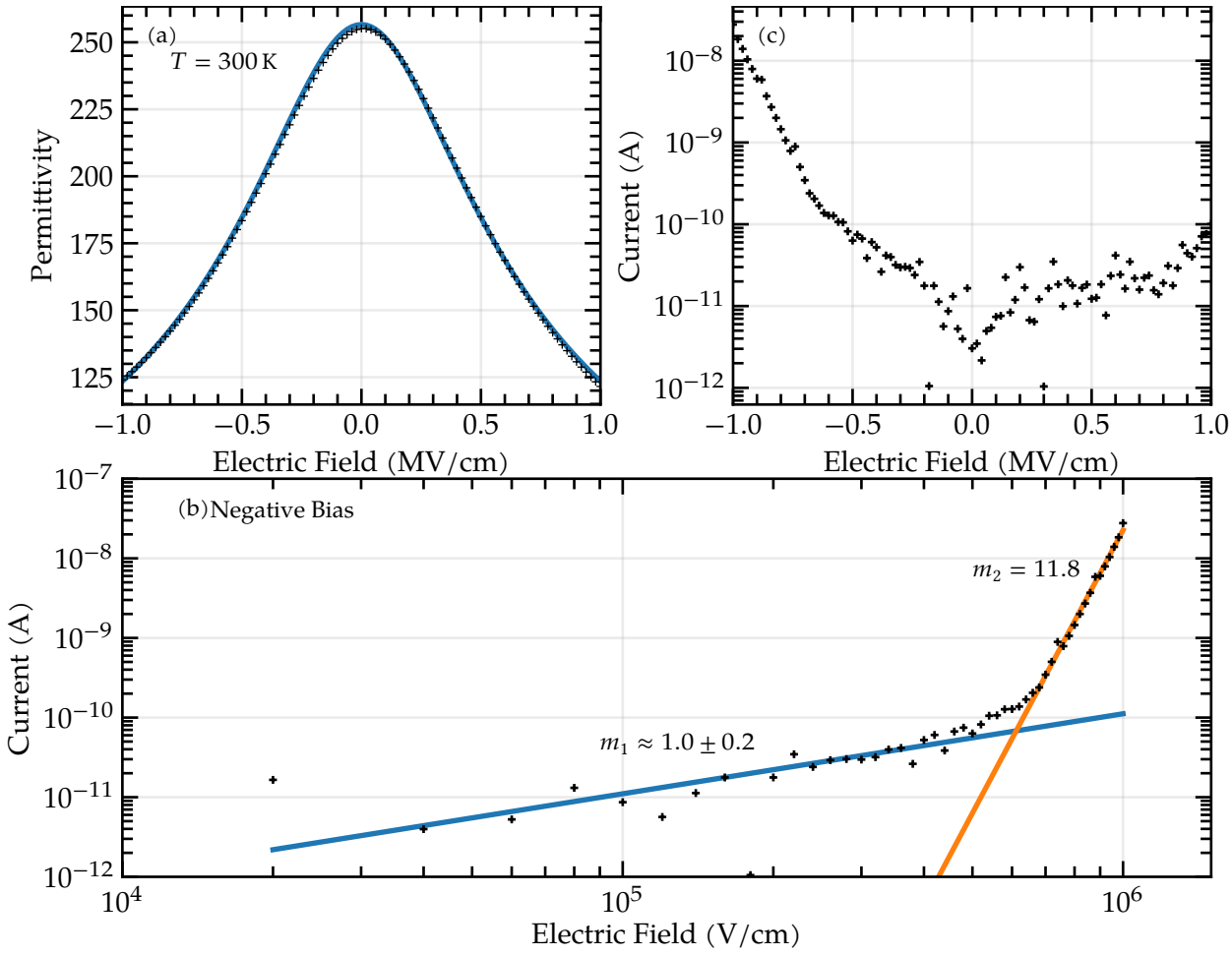

Figure 5.8: (a) Room-temperature field dependence of the permittivity, measured on a PLD grown $SrTiO_3$ thin film of 1 µm thickness. The zero-field permittivity is around 260. The Landau-Devonshire model was fitted to the field-dependent permittivity. (b) Current-voltage measurement to determine leakage currents. (c) Double logarithmic plot to determine the origin of the increase current for negative bias.

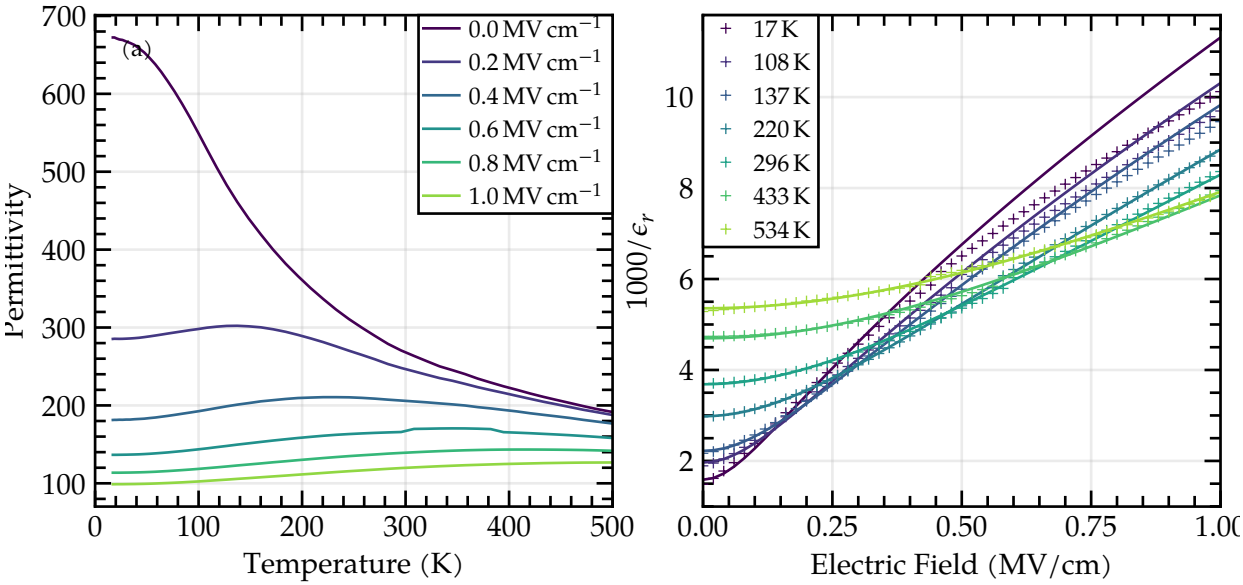

Figure 5.10: Measurement of the permittivity of the PLD layer in a temperature range of 20 K to 534 K and a electric field strength of up to 1 MV cm^{-1} to determine $\epsilon_r(T, E)$ for transport models in resistive switching devices.

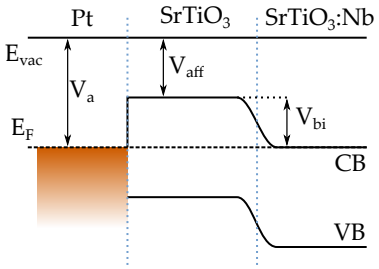

Figure 5.9: Ideal model of the band structure of an $SrTiO_3$ on $SrTiO_3$ metal-insulator-semiconductor structure. The built-in voltage V_{bi} comes from a different alignment of the Fermi level within the insulating and doped $SrTiO_3$ film and substrate, respectively. Due to that, a space charge region can form in the substrate. (adapted from reference [170])

the current is on a low level of 1×10^{-11} A. An approach was done to find the origin of the current flowing for negative bias. For this, the current over electric field is plotted in double logarithmic scale in figure 5.8(c). Two slopes were identified: $m_1 = 1.0 \pm 0.2$ in the low field region and a steep slope of $m_3 = 11.8$ in the high field region. The slope directly gives the proportionality of current to field, thus m_1 represents an ohmic conduction. The slope of m_3 can be addressed to space-charge limited conduction, which can occur at high field strength in a dielectric by charge carrier injection.[78,134,170] The high proportionality ($I \propto V^{11.8}$) can occur, if traps play a role in space-charge limited devices. After reaching a threshold voltage, all traps are filled with charge carriers and additional charge carriers are injected into the conduction band, leading to a strong increase of the current.[78,134] Further discussions about the transport mechanism can be found in chapter 5.3.

Figure 5.10(a) shows the temperature dependence of the layer for the field-free permittivity. Compared to the values from literature and bulk single-crystals (chapter 5.2.1), the increase of the permittivity with lowering the temperature is weakened. In bulk single-crystals, the permittivity is increased by a factor of 100, in the case of the thin films, it less than a factor of 4. The reasons for this lowering will be discussed in the following.

Until now, an ideal plate capacitor structure was considered. Interface charges $C_{\text{interlayer}}$ and the substrate contribution $C_{\text{substrate}}$ have to be considered as well, which gives a series capacitance and thus lead to a lowering of the estimated permittivity. The capacitance for calculating the permittivity using equation 5.9 is then

given by subtraction of the series contribution from the measured inverse capacitance value $C_{\text{meas.}}$:

$$\frac{1}{C_{\text{layer}}} = \frac{1}{C_{\text{meas.}}} - \frac{1}{C_{\text{substrate}}} - \frac{1}{C_{\text{interlayer}}}. \tag{5.10}$$

If the capacitance of the substrate and the interlayer are high, they can be neglected. If they are within the same range of the layer, the underestimation can get large. For the substrate, this contribution can effectively avoided by using a high doping level, since the contribution would come from the space charge region in the substrate. For such a substrate, the capacitance would be high. The doping concentration in the used substrate is 0.5 wt. %, which results in $N_D \approx 1.5 \times 10^{20}\,\text{cm}^{-3}$, which was confirmed by Hall effect measurements. Using the formula for the specific capacitance of a space charge region[170]

$$c = \sqrt{\frac{q\epsilon_0\epsilon_r N_D}{2\left(V_{bi} - V - \frac{k_B T}{q}\right)}}, \tag{5.11}$$

the space charge region capacitance can be estimated. The permittivity value for the substrate was taken from figure 5.6. Electron affinity is a material parameter for semiconductors in analogy to the workfunction of metals. It is not referenced to the Fermi level as in metals but to the conduction band minimum, i.e., for both the substrate and the layer it is the same value. The built in voltage, which is the difference between the electron affinities of both, the substrate and the thin film is hard to determine and depends on the position of the Fermi level (figure 5.9). In the ideal case, the Fermi level of the insulating, unintentionally doped thin film is in the center of the band gap, for the highly doped substrate it is to be expected, that the Fermi level is in the conduction band. Thus, a $V_{bi} = 1.63\,\text{V}$, which is half of the band gap, was used for the calculation. The Boltzmann factor $k_B T/q \leq 0.026\,\text{V}$ for temperatures below or at room-temperature was neglected. The space charge region capacitance is then

C	capacitance
c	specific capacitance per area
q	elementary charge
ϵ_0	vacuum permittivity
ϵ_r	relative permittivity
N_D	donor concentration
V_{bi}	built-in voltage
V	external bias
$k_B T/q$	Boltzmann factor

$$c_{\text{substrate}}(300\,\text{K}) = 1.5 \times 10^{-5}\,\frac{\text{F}}{\text{cm}^2}. \tag{5.12}$$

Typically, capacitances were measured in the range of $c_{\text{min}} = 7 \times 10^{-9}\,\text{F cm}^{-2}$ and $c_{\text{max}} = 1 \times 10^{-7}\,\text{F cm}^{-2}$, resulting in a maximum underestimation of less than 1 % of the layer capacitance. In the case of the PLD layer discussed in this chapter, the room temperature value was $c_{\text{PLD}} = 2.2 \times 10^{-7}\,\text{F cm}^{-2}$, resulting in a permittivity value of $\epsilon_r = 259$. In figure 5.11, the capacitance of the measurement, the capacitance of the substrate and the resulting layer capacitance (equation 5.10) are shown over the temperature. At any temperature, the influence of the substrate capacitance is low and $C_{\text{meas.}} \approx C_{\text{layer}}$.

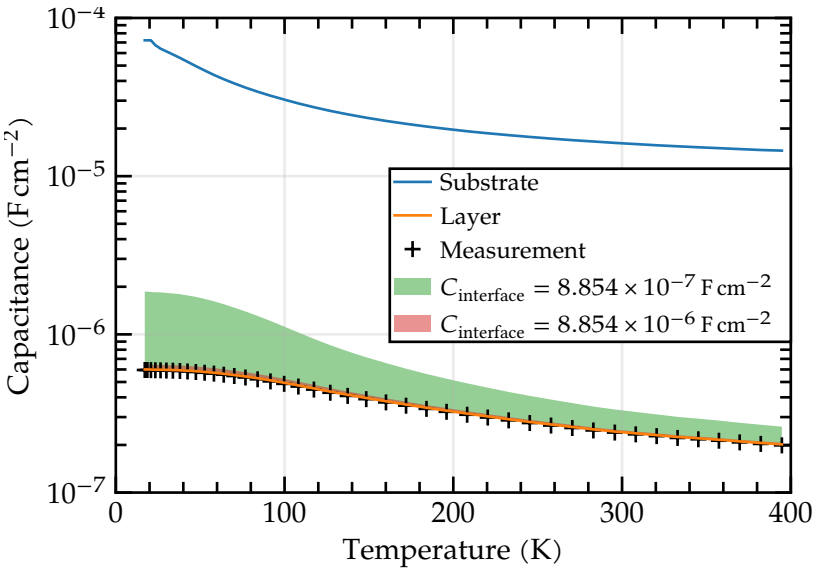

Figure 5.11: Temperature dependence of substrate capacitance and layer capacitance. The capacitance of the layer is weakly temperature dependent, unlike the substrate capacitance. Interface charges, if low, can lead to an underestimation of the permittivity.

Another effect can be interface charges between electrode and thin film, which was discussed by various authors.[107,205] They consistently found an interface capacitance of $c_{\text{interface}}$ from $8.854 \times 10^{-6}\,\text{F cm}^{-2}$ to $8.854 \times 10^{-5}\,\text{F cm}^{-2}$ and an independence to the temperature. The shaded areas in figure 5.11 show layer capacitance with taking interface charges into consideration. With the minimal value from literature reports for the interface charge, the underestimation of the permittivity is still negligible (red area, barely visible). With assuming a lower interface charge, the underestimation of the permittivity gets larger. On the other hand, the interface capacitance, assuming it is temperature independent,[107,205] cannot explain the deviation from the temperature dependence of the substrates. If the interface capacitance gets more dominant in the series capacitance, it increases the low temperature permittivity and reduces the deviation from the substrate permittivity value. At the same time, it would increase the room-temperature permittivity above the value of around 300 measured for substrates, and thus give an deviation from the substrate permittivity at room temperature. For example, in figure 5.11, a low interface capacitance of $8.854 \times 10^{-7}\,\text{F cm}^{-2}$ was assumed, which increases the calculated value of the permittivity from 680 to 2260 at 20 K (Neville et al.:[120] 16 000). At the same time, the room temperature permittivity is increased from 259 to 340 (Neville et al.:[120] 330).

The weakening of the permittivity in epitaxial layers is extensively studied and the origin is frequently explained by interface, dielectrically dead interface layers, meaning that the quotient ϵ_r/d

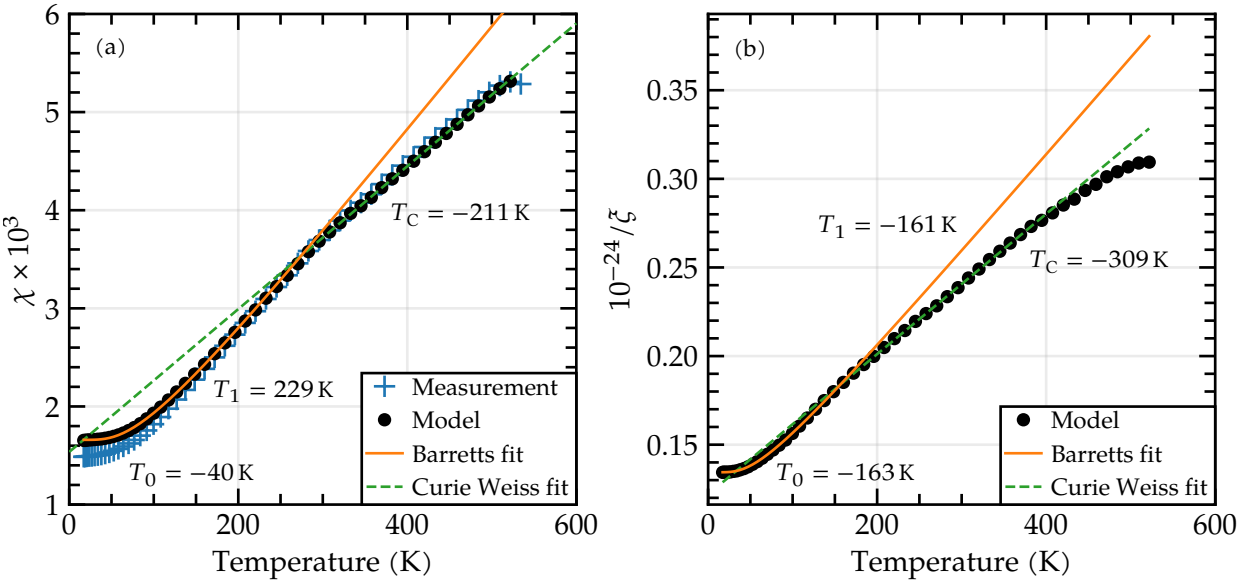

Figure 5.12: Modeling the temperature and field-dependence with the Landau-Ginzburg model by using the permittivity data presented in figure 5.10. Barretts formula and the Curie Weiss law are then applied on the obtained coefficients χ and ξ.

is small.[10,209] Using a mean-field approach, Zhou et al. pointed out, that this dead dielectric layer is even intrinsic. Contrary to this explanation, also very high permittivity values exceeding 1×10^4 were achieved.[53,100] Sirenko et al.[164] measured the TO_1 phonon frequency in a 2 µm thick PLD grown layer with a weak temperature dependence of the permittivity, They found, that the phonon frequency is less temperature dependent in such a layer, the soft-phonon mode is hardened. The measurement is a confirmation of the Lyddane-Sachs-Teller relation (equation 5.2) and the dominant contribution of the TO_1 mode to the permittivity. Additionally to this, it is a proof, that the permittivity of the layer itself is less temperature dependent without the need of an additional interface layer. Moreover, the phonon hardening has been shown to be dependent on off-stoichiometry[67,73,95,178], point-defects[100] and impurities[6]. Beside of this, the phonon hardening can be a accompanied with the formation of polar nano regions.[175] Polar nano regions can occur in ferroelectric materials and similar to magnetic domains, stabilize the local polarization due to interaction of the dipoles. Polar nano regions will play a role in the modeling of the resistive switching in the $SrTiO_3$ MOVPE thin films and will be further discussed in chapter 5.4. Concluding the findings so far, the lowering of the permittivity can't be explained by the influence of the substrate or dielectrically dead interface layers. Thus, it is expected to have a extrinsically induced phonon hardening. e.g. by defects. Additionally, it can be a hint for polar nano regions in the material.

Figure 5.10(a) shows not only the zero-field temperature dependence of the permittivity, but also the temperature dependence for high electric fields of up to $1\,\mathrm{MV\,cm^{-1}}$, which was achieved by applying voltages of up to 100 V. The permittivity increase with lowering the temperature is weaker with higher electric fields. At the maximum field of $1\,\mathrm{MV\,cm^{-1}}$, the temperature dependence of the permittivity changes from increasing to decreasing. Figure 5.10(b) shows the same data, but in this case, the field dependence is shown for a fixed temperature. The data was fitted with the Landau-Ginzburg theory. At high temperatures, the permittivity follows the model, but at low temperature, a deviation from the model is visible. This can be explained by the occurrence of an additional polarization at low temperatures and the occurrence of polar nano regions.[5,175] Akimov et al.[5] have shown, that again, the permittivity is connected to the soft phonon mode and that the lowering of the permittivity by the electric field can be attributed to a hardening of that mode. Thus, they expanded the Lydanne-Sachs-Teller relation to the field-dependence of permittivity and soft phonon mode:[5]

$$\epsilon_r(T,E) \propto \frac{1}{\omega^2_{\mathrm{TO}_1}(T,E)}. \tag{5.13}$$

ω_{TO_1}	Thin film soft phonon frequency
Ω_{TO_1}	Bulk single-crystal soft phonon frequency
$\langle P_S \rangle$	Extrinsic, static polarization

Akimov et al. also concluded, that from the difference between the soft phonon frequency of the bulk crystal and the thin film the extrinsic polarization of the crystal can be derived by

$$\omega^2_{\mathrm{TO}_1}(T,P_S) - \Omega^2_{\mathrm{TO}_1}(T) \propto \langle P_S^2(T) \rangle. \tag{5.14}$$

This equation is only valid for a perfect paraelectric substrate. The permittivity data measured for the used substrate indicate, that this is probably not the case, due to the low permittivity at low temperature. However, still, the strong lowering of the soft-phonon mode is an indication for a extrinsically induced polarization. Akimov et al. additionally conclude from the hardening of the soft phonon mode, that polar nano regions can exist in the layer. The occurance of polar nano regions can be induced by the $\mathrm{Ti_{Sr}}$ antisite defect. The influence of this defect on the dielectric and ferroelectric properties in $\mathrm{SrTiO_3}$ will be discussed in the next chapter for MOVPE thin films.

5.2.3 MOVPE grown $\mathrm{SrTiO_3}$ thin films

Metal-organic vapor phase epitaxy (MOVPE) was used to homoepitaxially grow $\mathrm{SrTiO_3}$ thin films of 40 nm thickness. The ratio of the strontium and titanium precursor was varied between 2.2 and 3.6. This refers to the ratio of the precursor in the liquid phase before evaporation and thus, the incorporated ratio

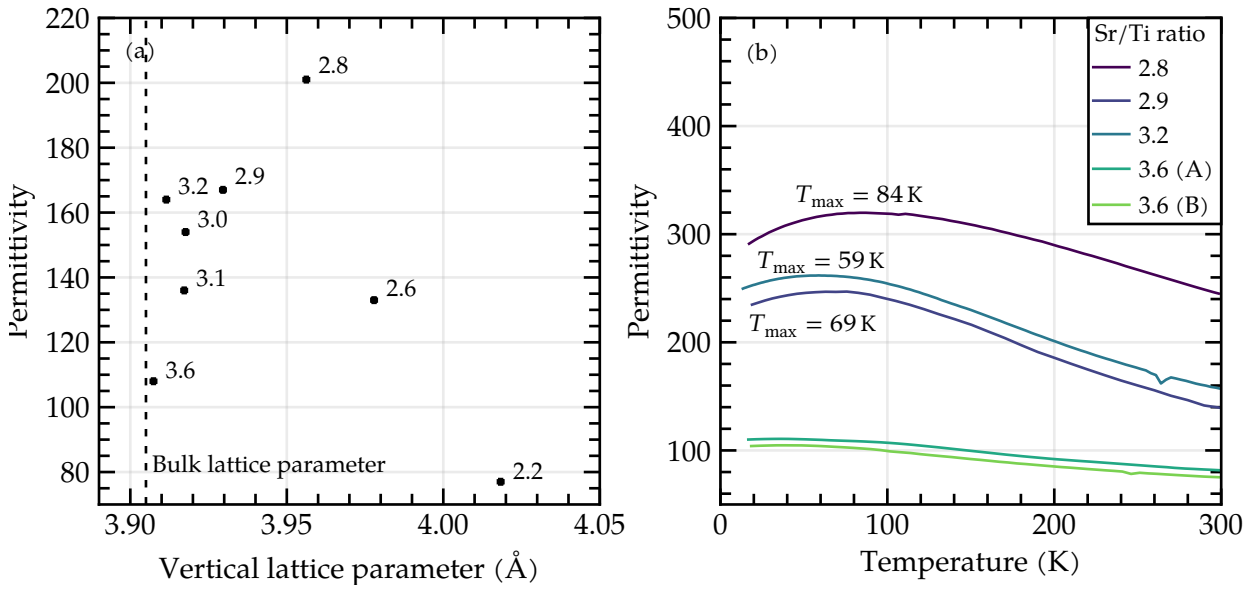

Figure 5.13: (a) Dependency of the permittivity for MOVPE grown $SrTiO_3$ on the lattice parameter and thus the tetragonal distortion. Additionally, it correlates with the Sr/Ti precursor ratio, which is an indication of stoichiometry control in the thin films. (b) The permittivity over temperature plots for some a selection of the grown thin films. The temperature dependence is weak. Beside of that, a damping of the permittivity at low temperature is seen, which is an indication of strong polarization.

of strontium and titanium can differ from this value. As an indicator for the deviation from stoichiometry the vertical lattice parameter was measured. Any off-stoichiometry lead to a tetragonal distortion, thus, a value close to the bulk lattice parameter is assumed to be "stoichiometric". However, this can only be a rough estimate and only deviations from stoichiometry in the range of percent can be detected.

The thin films were investigated for their dielectric properties. For this, circular platinum contacts with a thickness of 50 nm and a diameters of 150 µm, 200 µm and 300 µm were deposited through a shadow mask by e-beam evaporation (figure 5.14). The backside was covered with In/Ga eutectic to form a ohmic contact. The specific capacitance was in the range of 2×10^{-6} F cm^{-2} to 5×10^{-6} F cm^{-2}, so that again the substrate capacitance contribution can be neglected. In principle, an effect from a interface layer can lower the measured permittivity, however, as it was pointed out in chapter 5.2.1, the existence of such a layer is questionable.

In figure 5.13(a), the dependence of the permittivity on two parameter is shown: The lattice parameter and the Sr/Ti precursor ratio (annotated numbers). The lattice parameter of $SrTiO_3$ is shown as a vertical dashed line in the plot. It can be seen that the permittivity of the stoichiometric sample is significantly lower and has a value of around 100 compared to the permittivity value of around 300 for $SrTiO_3$ bulk single-crystals. With increasing

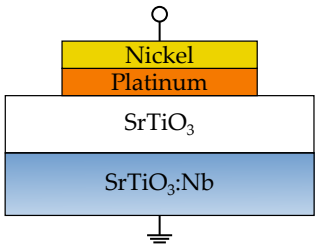

Figure 5.14: Schematic layout of the device structure

MOVPE thin film

- **Thickness:** 40 nm
- **Sr/Ti precursor ratio:** 2.9
- **Substrate:** $SrTiO_3$:Nb 0.5 wt. %
- **Top contact:** Pt 20 nm/Ni 20 nm
- **Contact size:** circular, ⌀200 µm
- **Bottom contact:** In/Ga eutectic

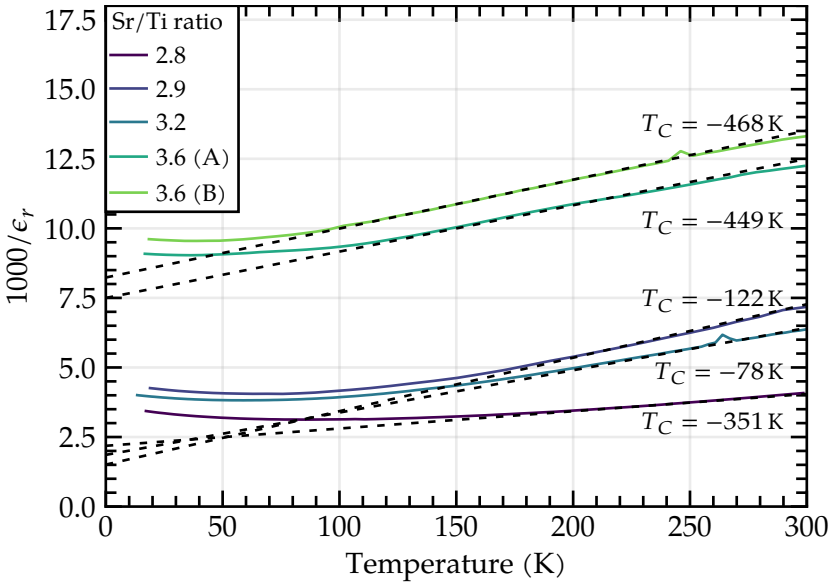

Figure 5.15: Curie-Weiss law fitted to the permittivity over temperature of MOVPE grown samples grown under different Sr/Ti precursor ratios.

deviation from the stoichiometry, the permittivity is increasing, with a peak at around 3.95 Å vertical lattice parameter or a Sr/Ti precursor ratio of 2.8. For higher deviations from the stoichiometry, the permittivity is decreasing again.

Figure 5.13(b) shows the temperature dependence for samples with different Sr/Ti precursor ratio value between 2.8 and 3.6. The values at room-temperature slightly deviate from the measurements in figure 5.13(a). Additionally, the temperature dependent measurement were performed on two similar samples with a ratio of 3.6, which again shows a small shift in the curves. The reason for these discrepancies can be inomogeneities in the thin films or differences in the contact preparation. However, the temperature dependent measurement of the sample with a ratio of 3.6 shows a good reproducibility of the temperature dependency.

Two samples with a Sr/Ti precursor ratio of 3.6, close to stoichiometry, were measured. The temperature increase almost vanished and is for both samples only increasing by 25 %. Both samples show a similar slope, indicating a good reproducibility of the process. Samples with decreasing Sr/Ti precursor ratio have a stronger dependence of the permittivity of the temperature. In contrast to substrates, pulsed laser deposited samples or the stoichiometric samples, the permittivity has a peak and is decreasing below that peak temperature again. The sample with the strongest off-stoichiometry in this series, with a Sr/Ti precursor ratio of 2.8, also shows this peak. However, the sample again shows a weaker temperature dependency.

Figure 5.15 shows the plot of $1/\epsilon_r(T)$ of the samples from figure 5.13(b). For the stoichiometric samples, a well-defined linear slope is visible, which was used for fitting the Curie-Weiss law from equation 5.1. A calculated Curie temperature of around $-450\,\mathrm{K}$ was measured for both samples, indicating a suppressed ferroelectric phase transition. The Curie-Weiss fit for the samples with a lower Sr/Ti precursor ratio is more difficult, since no clear linear slope was measured. The Curie temperature, shown in the figure, are higher but still negative compared to the stoichiometric samples.

Two effects play a role in influencing the dielectric properties of the MOVPE grown thin films. First of all, the temperature dependence is strongly weakened, indicating a phonon hardening, as it was discussed in the previous chapters. This phonon hardening can also explain the low permittivity at room-temperature.

Since the lattice parameter of the samples with a Sr/Ti precursor ratio of 3.6 is very close to the lattice parameter of bulk single-crystals, it is unlikely that the phonon hardening comes from a tetragonal distortion, especially, one would expect that the phonon hardening is getting stronger for higher deviations from the bulk vertical lattice parameter. Also, the stoichiometry series shows, that a dielectrically dead interface layer, as it was discussed in literature, is not the dominant factor in reducing the permittivity. The electrode preparation is the same for all samples, but still the dependence on the Sr/Ti precursor ratio is visible. Point defects, especially V_{Sr} or the $\mathrm{Ti}_{\mathrm{Sr}}$ defect, are possibly be responsible for the phonon hardening. The presence of such a defect is expected due to the additional supply of Ti. Varley et al.[182] have shown a low formation energy of strontium vacancies under high oxygen and titanium partial pressure. Choi et al.[26] have shown a low formation energy under Ti rich conditions, however, they also pointed out that for oxygen and titanium rich conditions, the formation energy can be higher. At least the formation of V_{Sr} is highly likely in these samples, as STEM-EDX measurements have shown a strong strontium deficiency (chapter 5.1).

The second effect is the decrease of the permittivity below a certain temperature. The effect gets stronger with higher strontium deficiency. Beside of the formation of a peak permittivity, also the peak is shifting to higher temperatures, from $T_{\mathrm{max.}} = 59\,\mathrm{K}$ for the Sr/Ti precursor ratio of 3.2 to $T_{\mathrm{max.}} = 84\,\mathrm{K}$ for a Sr/Ti precursor ratio of 2.8. The permittivity at temperatures above this peak temperature is also not clearly following the Curie-Weiss law anymore. These are a indication of polar nano regions, as they were already discussed to exist in $SrTiO_3$.[26] This is especially interesting, since the $\mathrm{Ti}_{\mathrm{Sr}}$ defect is inducing a dipole and has different stable positions and thus different polarization configurations are

possible. It is expected, that for nearly stoichiometric samples, strontium vacancies (and Ti_{Sr}) exist, but in such a low concentration, that no interaction between the defects is occurring. For lower Sr/Ti precursor ratios, a strontium deficiency of up to 20 % was shown. In this case, the defects can interact with each other and stabilize their polarization, similar like magnetic domains, in form of polar nano regions.

Lastly, it has to be discussed, why the permittivity is dropping to lower values at very low Sr/Ti precursor ratios. There are two possible explanations. The first one is, that TEM investigations have shown extended defects in these layers, which might reduce the polarizability. On the other hand, density functional theory calculations by Klyukin et al.[85] have even expected a decrease of polarizability for high Ti_{Sr} concentration. The reason is, that due to the high defect concentration the displacement of the titanium atom gets reduced from 0.78 Å for a Sr/Ti ratio(1) of 0.93 to 0.45 Å for a cation ratio of 0.78. The cation ratio for which the displacement is reduced fits also to the TEM investigations. The sample with the highest strontium deficiency without showing extended defects has a cation ratio of 0.77 (23 % Sr deficiency, chapter 5.1), which is close to the value from Klyukin et al. Thus, it can be concluded that the formation of V_{Sr}, in combination of Ti_{Sr} defects, are the driving factor for the phonon hardening in MOVPE grown $SrTiO_3$ thin films and that these defects can form polar nano regions.

5.2.4 Summary

In this chapter, the dielectric properties of $SrTiO_3$ substrates, PLD films and MOCVD thin films were investigated. The temperature dependence of the permittivity is a central point in this investigations, since it can indicate a hardening of the soft phonon mode, which can be caused by strain or defects, and can give a indication for polar nano regions.

In the first step, different substrates were compared with literature values. For some substrates, a lowering of the permittivity was found, indicating defects in the crystals. These might be impurities or occur due to the high thermal stress during the Verneuil growth. High quality, edge-defined film-fed grown crystals in contrast show a high low temperature permittivity and Curie temperatures, which was also reported in literature. However, the availability of edge-defined film-fed grown crystals was limited, so commercial Verneuil crystals were used.

(1) In this case, the ratio means the cation ratio in the crystal, not the precursor ratio which is used for the MOVPE grown thin films.

A pulsed laser deposited film of 1 µm was investigated for the temperature and field dependency. It was found, that the ferroelectric phase transition is suppressed and the permittivity is strongly lowered, thus the soft phonon mode is hardened. Since strain would increase the Curie temperature and no extended defects were found, theses hardening is most likely caused by point defects, which can also induce an additional, extrinsic polarization in the crystal. The Landau-Ginzburg theory for the field and temperature dependence of the permittivity was applied on the permittivity data, allowing it to calculate $\epsilon_r(E,T)$, which can be used in the transport models for resistive switching.

The impact of stoichiometry on MOVPE grown thin films was discussed. It was shown, that for stoichiometric samples, a very low permittivity of around 100 was measured, showing a weak temperature dependency. These can be attributed to phonon hardening by V_{Sr} and Ti_{Sr} defects. Higher concentrations of these defects increase the polarizability and thus the permittivity value. Temperature dependent measurements additionally indicate the formation of polar nano regions for highly off-stoichiometric samples. The decrease of permittivity for Sr/Ti precursor ratios below 2.8 is another strong indication for the presence of Ti_{Sr} defects, as it was predicted, that the displacement (and thus polarizability) of the antisite titanium is reduced in such layers.

5.3 EXPERIMENTAL CHARACTERIZATION OF RESISTIVE SWITCHING

5.3.1 Hysteresis curves

In this chapter, the hysteresis curves will be discussed. Figure 5.16 shows the schematic layout of the investigated resistive switching devices. They consists of an highly doped $SrTiO_3$:Nb(001) substrate with a Nb concentration of 0.5 %. On this substrate, unintentionally doped $SrTiO_3$ thin films of around 40 nm thickness were deposited.

Circular top contacts with 200 µm diameter were deposited by electron beam evaporation. The contact stack consists of a 20 nm thick platinum and a 20 nm thick nickel layer. Platinum was used to prevent oxidation of the contact, which can lead to the formation of oxygen vacancies in the thin film. Nickel was used to mechanically protect the platinum.

Static current-voltage curves were measured in 2-point probe setup. The measurements were performed to identify hysteresis behavior of the sample. For this, the voltage was ramped in both directions, first with increasing voltage, afterwards with de-

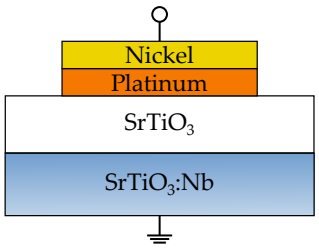

Figure 5.16: Schematic layout of the $SrTiO_3$ resistive switching device.
MOVPE thin film

- **Thickness:** 40 nm
- **Sr/Ti precursor ratio:** 2.9
- **Substrate:** $SrTiO_3$:Nb 0.5 wt. %
- **Top contact:** Pt 20 nm/Ni 20 nm
- **Contact size:** circular, ⌀200 µm
- **Bottom contact:** In/Ga eutectic

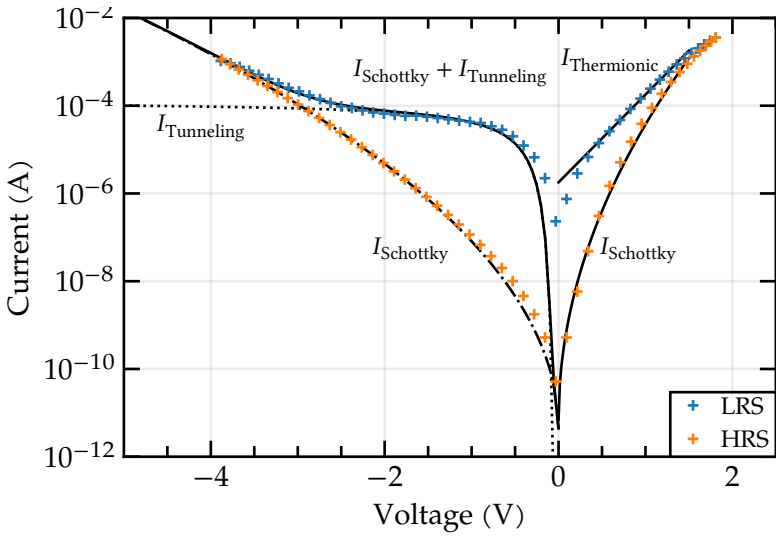

Figure 5.18: Hysteresis current-voltage curve an off-stoichiometric $SrTiO_3$ thin film. Each branch of the curve were fitted with appropriate electrical transport models. In negative voltage region for the LRS, a parallel current of trap-assisted tunneling and Schottky emission was found.

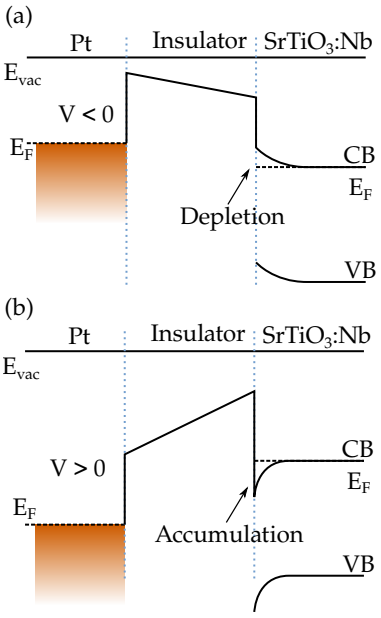

Figure 5.17: Band structures of MIS devices. (a) A negative bias leads to a depletion zone at the insulator semiconductor interface. (b) A positive bias leads to an accumulation of charge carrier at the interface.

creasing voltage. The voltage was continuously applied during the whole sweep. A voltage increment of 10 ms combined with an integration time of 10 mV were chosen.

The sample stack represents a metal-insulator-semiconductor (MIS) structure. Figure 5.17 shows the band structure of typical MIS devices with applied positive and negative bias. Applying bias leads to an depletion or accumulation at the interface. The insulating layer between top contact and substrate acts as a barrier for the current.

Still, a residual current can flow through the insulator due to injected charge carriers at high electric fields. Charge carrier injection can e.g. occur due to thermal emission above the interface barrier, or due to tunneling through the insulator. Some basic current transport mechanism are introduced in chapter 2.1. The sample was investigated for this current by measuring current-voltage curves.

In Figure 5.18 shows the current-voltage curve through an off-stoichiometric sample, grown with a Sr/Ti precursor ratio of 2.7. The sample shows resistive switching and a strong hysteresis between the low resistive state (LRS) and the high resistive state (HRS) was found. The current-voltage curves show a asymmetry between the positive and negative voltage region and in positive bias region, the current increases more rapidly compared to the negative voltage region.

The HRS of the negative voltage region was fitted by Schottky emission with the formula (see page 7)

$$J = A^{**}T^2 \exp\left(\frac{q}{k_B T}\left(\sqrt{\frac{qE}{4\pi\epsilon_0\epsilon_r}} - \phi_B\right)\right). \tag{5.15}$$

In the LRS, additionally a tunneling current occurs, which follows the current-voltage dependence of trap-assisted tunneling (see page 8)

$$J = \frac{q^2}{8\pi h\phi_T}E^2 \exp\left(\frac{-8\pi\sqrt{2qm^*}}{3hE}\phi_T^{3/2}\right). \tag{5.16}$$

The fit of the LRS was done by adding the tunneling current to the emission current I_{Schottky} of the HRS, so that $I_{\text{total}} = I_{Schottky,HRS} + I_{Schottky,LRS}$. This indicates parallel current paths of tunneling and Schottky currents in the LRS.

To determine the barrier height by using the models mentioned above, the field strength across the insulating layer has to be known. In the most simple case, the field strength can be calculated by dividing the voltage through the thickness of the thin film. However, this can be inaccurate due to two reasons. First of all, a depletion zone in the substrate would increase the insulating barrier thickness. Secondly, especially in the low resistive state, the voltage drop is not limited to the thin film itself anymore. Since the resistivity of the thin film in the LRS is so low, also voltage drops across the contacts and the substrate becomes relevant. Still, as a first approximation, the thin film thickness is used to calculate the electric field strength. Thus, determined values of the barrier height, especially in the LRS, might not represent the true barrier heights of the device.

The forward direction in the LRS follows the thermionic emission law. The barrier height was determined from equation 2.9 on page 6

$$J = A^{**}T^2 \exp\left(\frac{q}{k_B T}\left(\frac{V}{\eta} - \phi_B\right)\right). \tag{5.17}$$

A Richardson constant of 156 A cm^{-2} K^{-2}[166] and a temperature of 300 K is used for calculation. A barrier height of the LRS of 0.76 eV was found. This value was also found for Pt/$SrTiO_3$:Nb Schottky diodes.[99,127] The ideality factor was found to be $\eta = 8$. In an ideal Schottky diode, the ideality factor should be equal to one. In this device however, an insulating thin film is used, which increases the ideality factor. Concluding from the thermionic emission in the LRS, the device structure differs from a typical MIS structure in such a way, that there is no band discontinuity between substrate and thin films in the LRS. Instead, the devices has continous bands with a bending at the substrate - thin film interface due to the difference in fermi energy (figure 5.19).

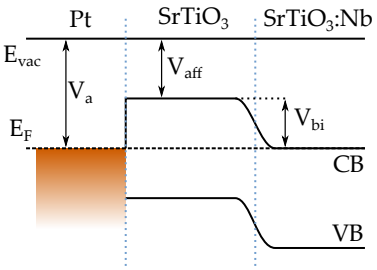

Figure 5.19: Band structure of the $SrTiO_3$ thin film in the LRS.

The HRS follows, similar like in the negative voltage region, also in the positive voltage region. The barrier height of 1.1 eV is higher than in the negative voltage region. Due to the current mechanism based on charge carrier injection, in the HRS the continuity of band can't be assumed and a situation like in figure 5.17 is expected. This means, that the resistive switching mechanism has to be influenced from the band alignment at the interfaces and is not a bulk effect, like it is the case for resistive switching models based on oxygen vacancy migration (see chapter 5.4).

5.3.2 Threshold voltage and gradual switching

In the following, the switching itself is discussed in more detail. For this, the resistive switching of an off-stoichiometric $SrTiO_3$ thin film, grown with a precursor ratio of $Sr/Ti = 2.9$ is investigated. The test structure on the left figure was cooled down to 10 K in a closed cycle helium refrigerator. The background pressure was at around 1×10^{-6} mbar. The current-voltage curves are recorded similar to the measurement in chapter 5.3.1. In the following chapters, the sweep with increasing voltage is called "forward direction", the sweep with decreasing voltage is called "backward direction". The minimum and maximum voltage (voltage range) is gradually increased until a hysteresis in the current-voltage curves is found. The corresponding current-voltage curves at 10 K are shown in figure 5.20.

Measuring the current-voltage curves in a small voltage range of ± 0.1 V ($\pm 25\,\mathrm{kV\,cm^{-1}}$) a current at the noise level of around 1×10^{-12} A is measured, indicating a highly insulating layer with $\rho >> 1 \times 10^{12}\,\Omega\,\mathrm{cm}$.

By further increasing the voltage, a current through the thin film is measured. During the first three sweeps (#1-#3) with a voltage range of ± 0.5 V, ± 0.75 V, and ± 1.0 V, no hysteresis was observed in the current-voltage curves. Repeating sweeps in this voltage range reproduce this observation.

A subsequent increase of the range to -2 V to 1.5 V leads to the evolution of a hysteresis curve. The hysteresis can be divided into two states, a high resistive state (HRS), which has a current level below the initial current (sweeps #1-#3), and a LRS, which has a current level above the initial state of the first three sweeps.

Figure 5.21 shows the current ratio between LRS and HRS. In the negative voltage range, a peak ratio of 2.1×10^7 is measured at -0.3 V. To higher voltages, the on-off ratio is decreasing. In the positive voltage range, the peak is at 0.75 V with a ratio of 4.1×10^5. Above this voltage, the ratio is decreasing again.

To investigate the resistive switching, pulsed measurements were performed. For this, a readout voltage was set to $U_{\mathrm{ro}} = -0.1$ V. This voltage is below, but close to the maximum of the

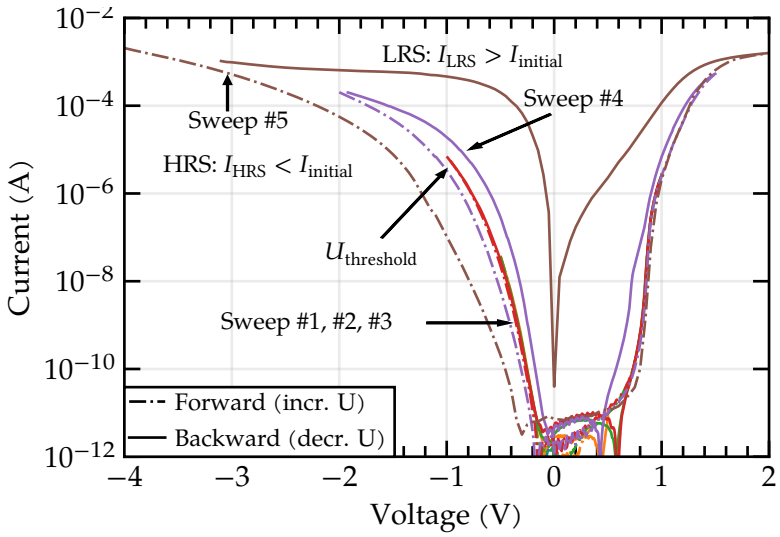

Figure 5.20: Current-voltage characteristics of $SrTiO_3$ thin film at 10 K. Several IV curves with different voltage ranges were recorded. Sweeps #1, #2, and #3 show reproducible (overlapping) IV characteristics. No hysteresis is found. The voltage range in sweep #4 is extended, so that the sweep has Sweep #4 voltage range is extended to negative and positive range and part of the sweep is above a threshold voltage U_4. As a result, the thin film is switching between HRS and LRS. The HRS curve shows a current below the initial, non-switching sweeps, the LRS an higher current. Sweep #5 has an even extended voltage range, increasing the difference between LRS and HRS.

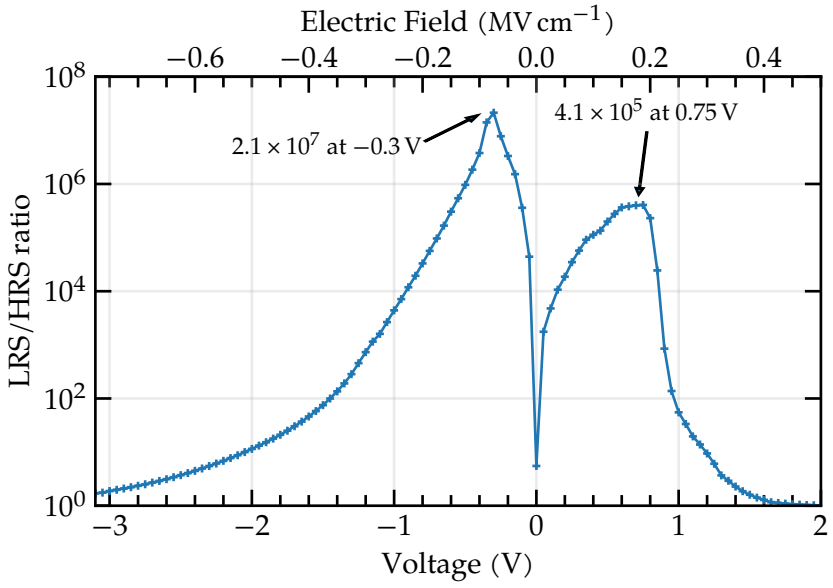

Figure 5.21: Ratio between LRS and HRS of hysteresis sweep #5 in figure 5.20. The maximum ratio between the states is 2.1×10^7 at −0.3 V and 4.1×10^5 at 0.75 V.

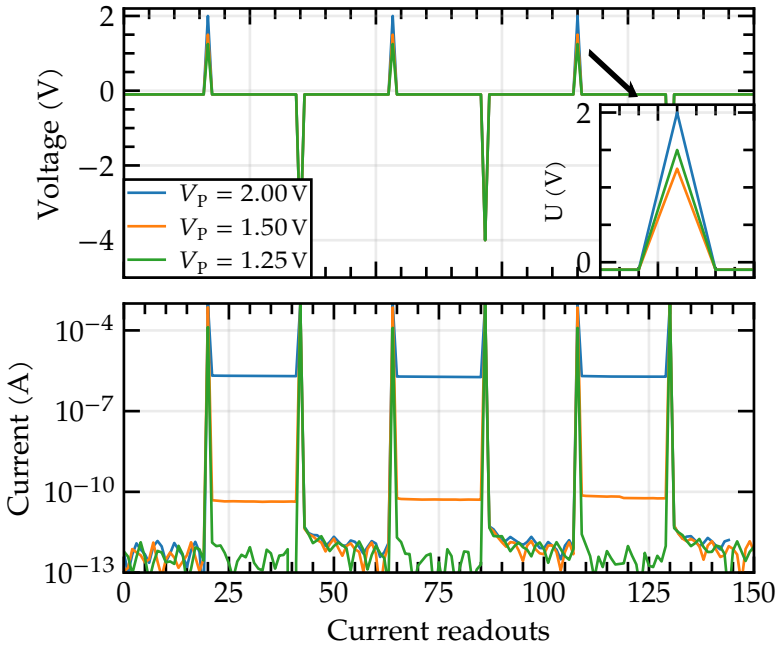

Figure 5.22: Pulsed IV measurements of $SrTiO_3$ thin film at 10 K. The U_{HRS} was set to −4 V. The U_{LRS} was varied between 1.25 V to 2 V. The readout voltage was set to $U_{ro} = -0.1$ V. The pulse length was set to 100 ms for all pulses. On the top, the voltage pulse pattern over time is shown. On the bottom, the corresponding current is shown. It is seen, that the LRS current increases with pulse U_{HRS} and no switching is observed below the threshold voltage $U_{threshold}$.

LRS/HRS ratio in figure 5.21. A small voltage is also chosen to prevent switching of the thin film during read-out. Since in figure 5.20 the sweeps up to ±1 V don't show a hysteresis, no switching is expected during the readout.

Voltage pulses were used to switch the sample between the two states. To switch the thin film from LRS to HRS, a voltage pulse of $U_{HRS} = -4$ V was applied. For switching from HRS to LRS, three different voltage pulses U_{LRS} of 1.25 V, 1.50 V, and 2.00 V were applied. The pulse lengths were 100 ms. After each pulse, 20 current readings with an integration time of 100 ms were used to check the state of the device.

Figure 5.22 shows the pulsed measurement. On the top, the voltage sequence *readout*, *LRS pulse* and *HRS pulse* is displayed. On the bottom, the corresponding current readings are plotted. After starting the measurement in HRS state with a current of 1×10^{-13} A at U_{ro}, a positive voltage pulse U_{LRS} sets the sample to the LRS. During the pulse a peak current is measured. Afterwards the readout is performed at U_{ro}, showing an increased current level for the LRS. For $U_{LRS} = 2$ V the LRS current is highest with 2×10^{-6}, $U_{LRS} = 1.5$ V shows a LRS current of 5×10^{-11} A, and $U_{LRS} = 1.25$ V does not show a switching to the LRS, the current stays at 1×10^{-13} A.

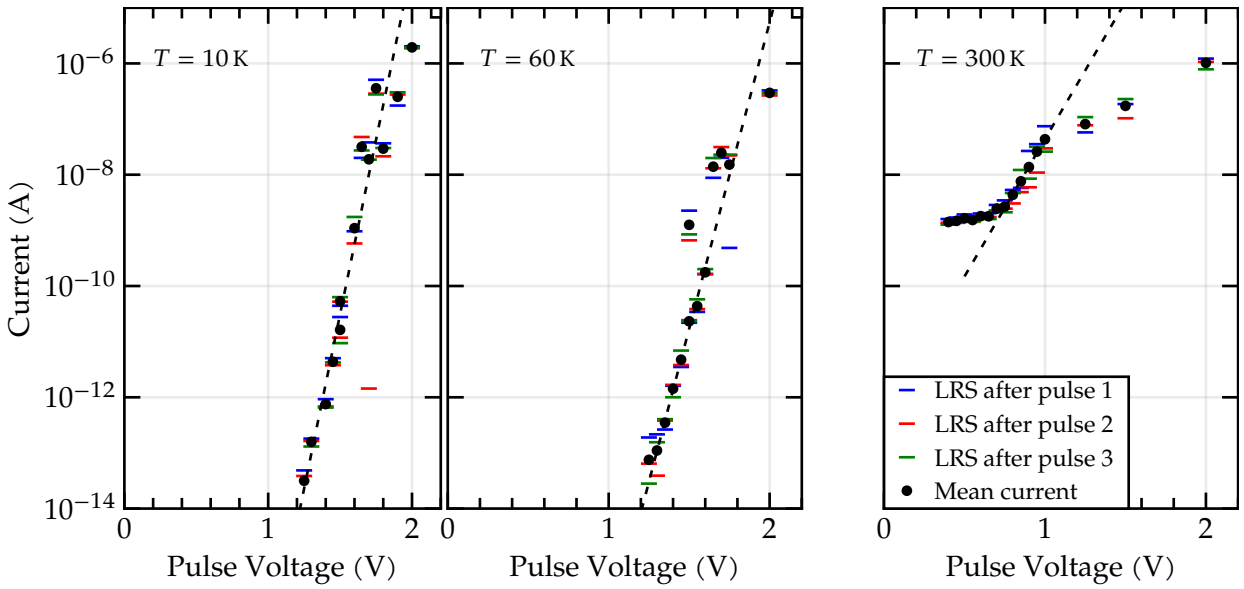

Figure 5.23: Measurement of the threshold voltage for resistive switching at different temperatures. The sample was pulsed with the pulse pattern shown in figure 5.22. Each horizontal line represent the average current measured at LRS after each of the three LRS pulses. The black circle represents the average of the three average LRS current values. For low temperature, the threshold voltage is at around $U_{\text{threshold}} = 1.2\,\text{V}$ to $1.4\,\text{V}$ and the LRS current is exponentially increasing with U_{LRS}. At 300 K, still a threshold at around 0.7 V to 0.8 V can be measured. In contrast to the low temperature measurements, the current at lower pulse voltages is limited by the increased HRS current and to the top by saturation.

The threshold voltage, at which a difference between LRS and HRS can be measured, was investigated at 10 K, 60 K and 300 K (figure 5.23). For this, a pulse pattern like in figure 5.22 was used with varying U_{LRS}. The U_{HRS} was fixed to $-4\,\text{V}$. The pulse width was set to 100 ms, the readout voltage was set to $-0.1\,\text{V}$.

In figure 5.23, the horizontal bars show average current level for the LRS after each of the three pulses for each pulse voltage. Additionally, the black circle shows the average of the three measurements. At 10 K, the U_{LRS} was varied between 1.2 V to 2 V. The LRS current level is exponentially increasing with increasing the pulse voltage. The threshold voltage can be determined to be 1.2 V to 1.4 V, which corresponds to an electric field strength of $300\,\text{kV cm}^{-1}$ to $350\,\text{kV cm}^{-1}$. The same is observed at 60 K.

A reduced threshold voltage of 0.7 V was measured at 300 K. Additionally, the current level of the HRS is increased to 1×10^{-7} A, which reduces the on-off ratio. At the threshold voltage, the current level of the increases exponentially over two order of magnitude from 1×10^{-9} A to 1×10^{-7} A. Above the threshold region, the LRS current increases to a maximum of 1×10^{-6} A.

Using the current voltage curves from figure 5.20, the transition between the different transport regimes can be shown. In the case where electronic transport is dominated by Schottky emission, a

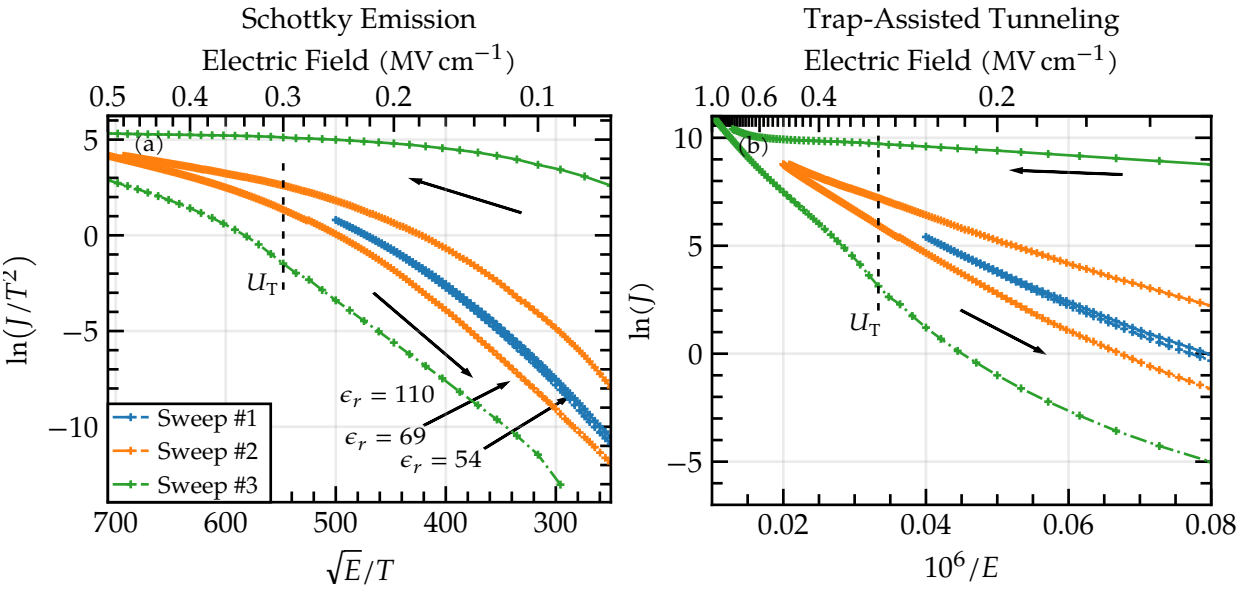

Figure 5.24: Linearized current - voltage relations for a) Schottky emission and b) trap-assisted tunneling. A linear slope indicates a good agreement with the corresponding model. The dashed vertical line indicates the threshold voltage U_T, for which the switching between the LRS and HRS occurs. For the HRS in the Schottky emission model, the permittivity is increasing the more the state is pronounced.

linearized relation between current and voltage can be obtained from equation 2.13 (page 7) via the graphical plotting of

$$\ln\left(\frac{J}{T^2}\right) \propto \frac{\sqrt{E}}{T}. \tag{5.18}$$

Analogously, the linearized relation in case of trap-assisted tunneling (derived from equation 2.17, page 8) is

$$\ln(J) \propto \frac{1}{E}, \tag{5.19}$$

and for thermionic emission (derived from equation 2.9, page 6) is

$$\ln(J) \propto V. \tag{5.20}$$

By plotting the current-voltage data with the above relationships, a linear appearance of the plot would give an indication of the corresponding transport mechanism. One difficulty in plotting these curves is that the exact field strength applied to the thin film is unknown. The field strength was calculated using $E = V/d$, with the applied voltage V and the film thickness d. However, the distance over which the field is applied can be much larger, e.g., if a space charge region exists in the substrate. In addition, it must be expected that, especially in the LRS, the voltage drop does not only occur across the $SrTiO_3$ layer, but also across the entire device, i.e. a significant voltage drop also occurs in the substrate or at the contacts. All models introduced in chapter 2.1 were tested

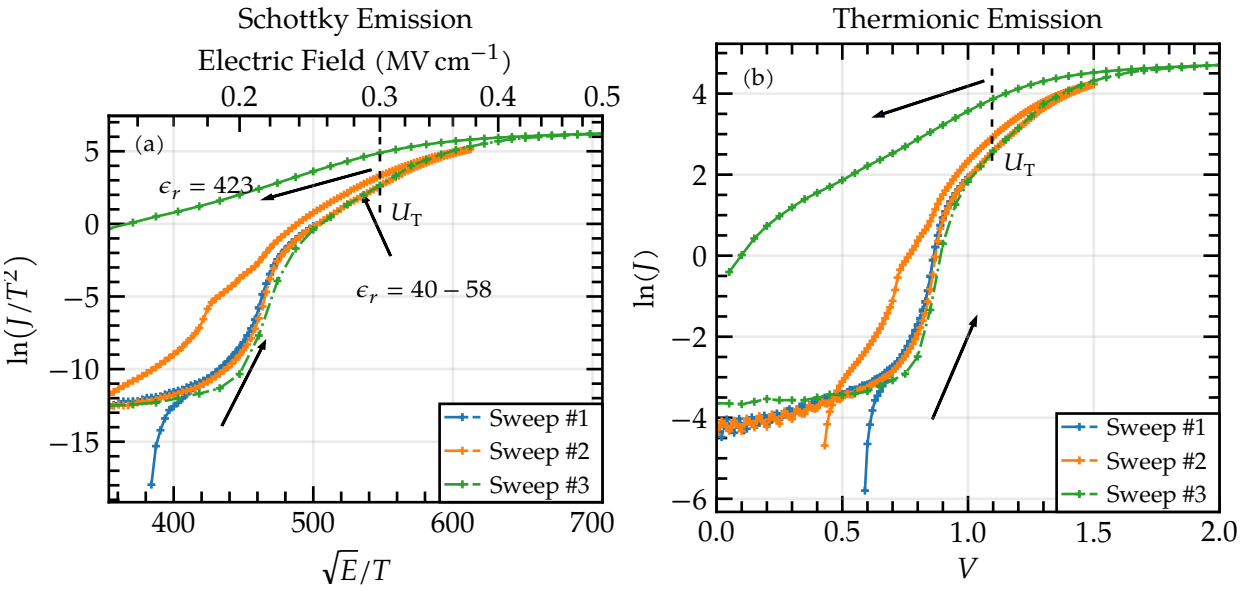

Figure 5.25: Linearized current - voltage relations for a) Schottky emission and b) thermionic emission. A linear slope indicates a good agreement with the corresponding model. The dashed vertical line indicates the threshold voltage U_T, for which the switching between the LRS and HRS occurs.

for consistency with the measurements, however, only those who show consistent results are presented in the following.

Figure 5.24 show the linearized relation between current and voltage for the Schottky emission model and the trap-assisted tunneling model in the negative voltage range. It can be seen that in the HRS, Schottky emission and in the LRS, trap-assisted tunneling dominates the charge carrier transport through the device. The states can be switched gradually, and the stronger the state was switched (by using higher electric fields), the more pronounced are the linear slopes. For the HRS, the permittivity was determined using equation 2.13 (page 7). Permittivity values between 54 and 110 were determined, which is in agreement to previous dielectric measurements (chapter 5.2.3). The more the HRS is pronounced, the higher is the permittivity.

To interpret the permittivity values determined from the emission current, static low-temperature capacitance measurements were performed at 1 MHz. The capacitance was measured at −0.1 V (probe voltage) for the HRS and LRS at 10 K. The LRS capacitance was 1139 pF, the HRS capacitance 1163 pF, which corresponds to $\epsilon_r(0)$ values of 163 and 167. This confirms that the permittivity of the thin-film differs for the HRS and LRS.

Figure 5.25 shows the forward direction in the linearized form for Schottky and thermionic emission. In the forward direction, the dominant transport mechanisms are Schottky emission and thermionic emission. Due to the low temperature, the charge carriers are initially not sufficiently thermally excited to overcome the barrier. Only from a field strength of about 200 kV cm^{-1} a

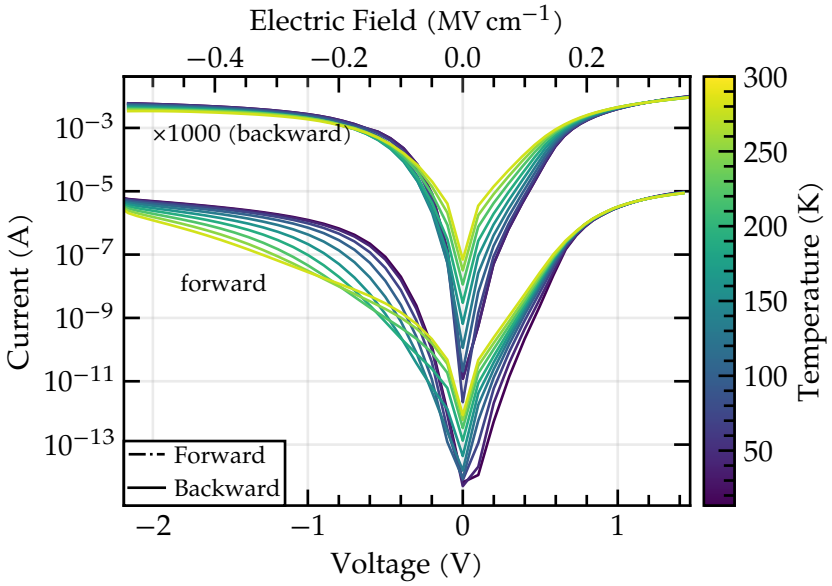

Figure 5.26: Temperature dependence of the current through the $SrTiO_3$ thin film. The low-resistive state in the LRS is temperature independent, indicating a tunneling current. The HRS in the negative voltage region decreases until cooling to 200 K, and increases again by further cooling the sample to 10 K. The positive bias region is temperature dependent and thus indicating a emission current.

strong increase in the current of the HRS is measurable. From the increase, a permittivity of 40 to 58 could be determined, which is somewhat lower than the value determined for the barrier direction. Thermionic emission dominates the LRS. From the slope of the curve, the ideality factor nu can be determined. The determined value is 374. A value of 1 is expected for an ideal Schottky diode. The reason for the significantly higher value in this resistive switching device is the insulating thin-film barrier.

Figure 5.26 shows the current voltage curves of the HRS and LRS for a temperature range of 10 K to 300 K. The positive voltage range shows a temperature dependence and the current decreases with lower temperatures. At higher voltages around 1 V, no temperature dependence can be observed, which may be due to a current-limiting series resistance, e.g. at the back contact. In the negative voltage range, only the HRS is dependent on the temperature. It can be seen that the current increases again at low temperatures below 200 K. This is attributed to the increase of the switching threshold voltage, which is increased at lower temperatures (see section before). Therefore, the layer is no longer completely switched between states at low temperatures.

The LRS in the negative voltage range shows no temperature dependence. This confirms the previous assumptions that this current load is dominated by a tunneling current.

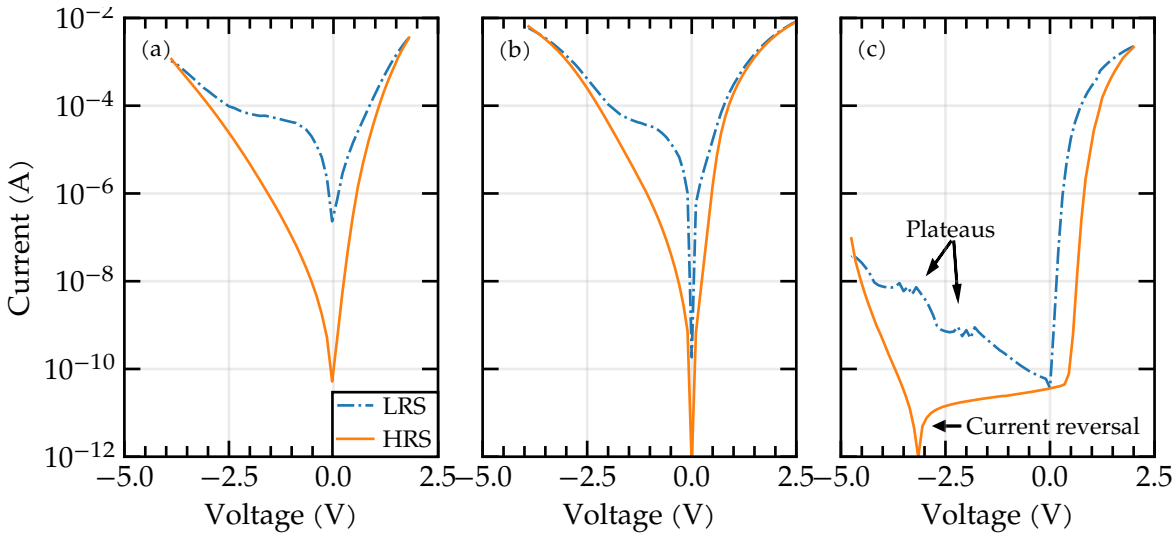

Figure 5.27: Resistive switching for three samples with differences in Sr deficiency measured at room-temperature. The Sr/Ti precursor ratios were (a) 2.7, (b) 2.9 and (c) 3.6. The ratio between low and HRS is higher for strong Sr deficiency and gets low for almost stoichiometric samples (c). The stoichiometric sample still shows a hysteresis, indicating some residual defect concentration.

5.3.3 Impact of Strontium deficiency

In figure 5.27, the hysteresis curves for three samples grown under different Sr/Ti precursor ratios are shown. (a) shows a off-stoichiometric sample with a high Sr vacancy concentration (Sr/Ti precursor: 2.7). (c) is a sample with a almost stoichiometric composition (Sr/Ti precursor: 3.6). The ratio between LRS and HRS increases with increasing off-stoichiometry. In the case of the nearly stoichiometric sample, still an asymmetry of the LRS and HRS is visible, but close to zero bias, no difference between the states can be measured. The positive bias region in the nearly stoichiometric sample also shows thermionic emission behavior for both, the LRS and HRS. This is in contrast to the off-stoichiometric samples, for which a Schottky emission current was measured in the HRS (see chapter 5.3.1).

Figure 5.28 shows pulsed measurements for a Sr deficient sample (Sr/Ti precursor ratio of 2.7), and of an stoichiometric sample. The pulse voltages to switch from the HRS to LRS at room-temperature where 2.3 V, and −4 V and −6 V to switch from the LRS to the HRS of the off-stoichiometric and stoichiometric sample, respectively. Even though the pulse voltage for the stoichiometric sample is higher, the ratio between low and HRS is only a factor of two. The off-stoichiometric sample shows a significantly higher on-off ratio of 1×10^3. The measurement of the off-stoichiometric sample shows gaps between several measurement points. This is due to device limitation, where the change of measurement range is causing delays.

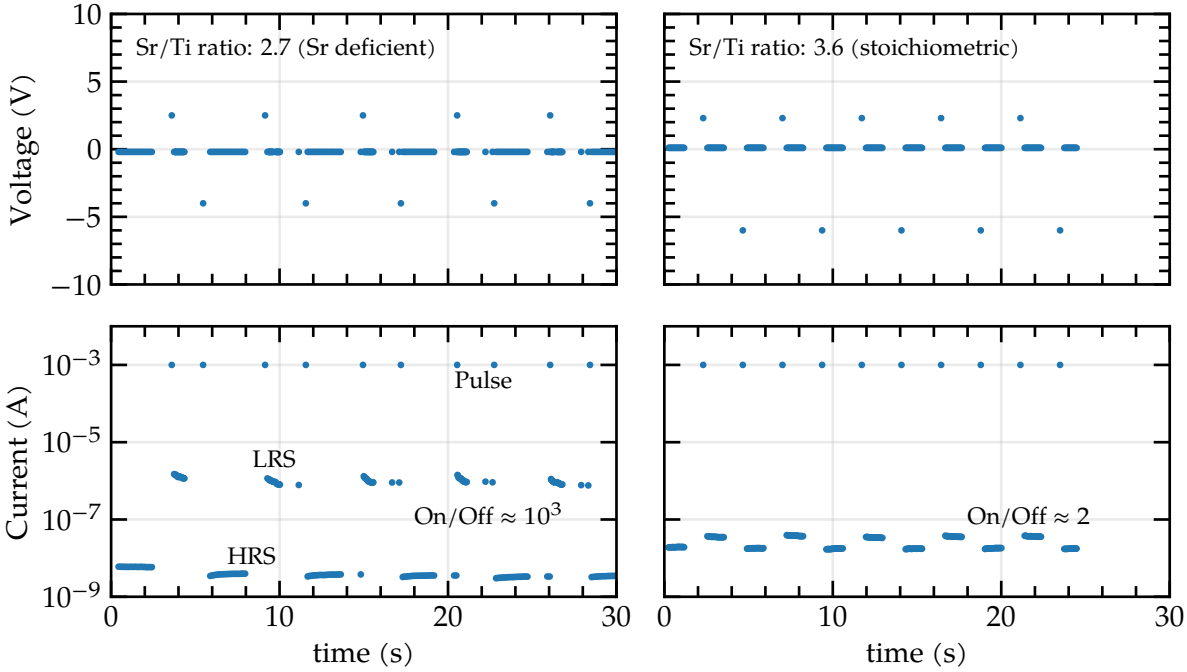

Figure 5.28: Pulsed measurement of a Sr deficient sample (left) and an almost stoichiometric sample. The off-stoichiometric sample shows a high ratio between low and HRS of 1×10^3, the stoichiometric sample only by a factor of 2.

In the following, the stoichiometric sample will be further discussed. The stoichiometric sample in figure 5.27(c) shows multiple plateaus with a constant current in the negative bias region for the backward direction. In forward direction, the current flow direction is reversing even before changing the electric field direction. In forward direction, the sample shows thermionic emission current behavior with a high n-factor of above 10, which indicates a non-ideal Schottky junction. This is expected, since the thin film is initially insulating.

The activation of the sample from the initially insulating state to the hysteresis curve was investigated and is shown in figure 5.29. With increasing the voltage range, the overall conductivity of the sample increases, e.g., at 0.5 V, the current increases by a factor of roughly 5 from the first to the last sweep. Similar to the measurements at 10 K, the hysteresis evolves with higher voltages due to the switching threshold voltage.

It was observed, that the process of "activating" the sample is reversible, so that the overall conductivity of the sample is decreasing again. The measurement is shown in figure 5.30. Over a period of 140 min, the current-voltage curve in a range of −0.5 V to 0.5 V is measured. The voltage was chosen to be below the switching threshold voltage. It can be seen, that the resistivity falls back to its initial value before switching. This behavior was

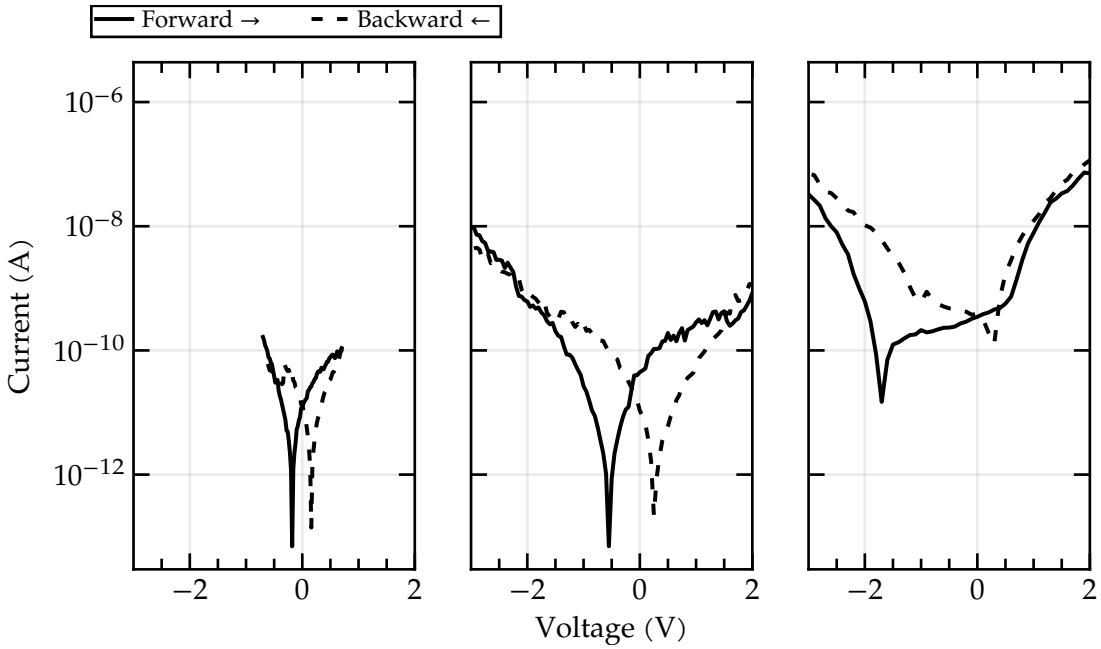

Figure 5.29: Current-voltage curves of a stoichiometric sample (Sr/Ti precursor ratio 3.6). The voltage range was gradually increased, which leads to an increased current the formation of the hysteresis

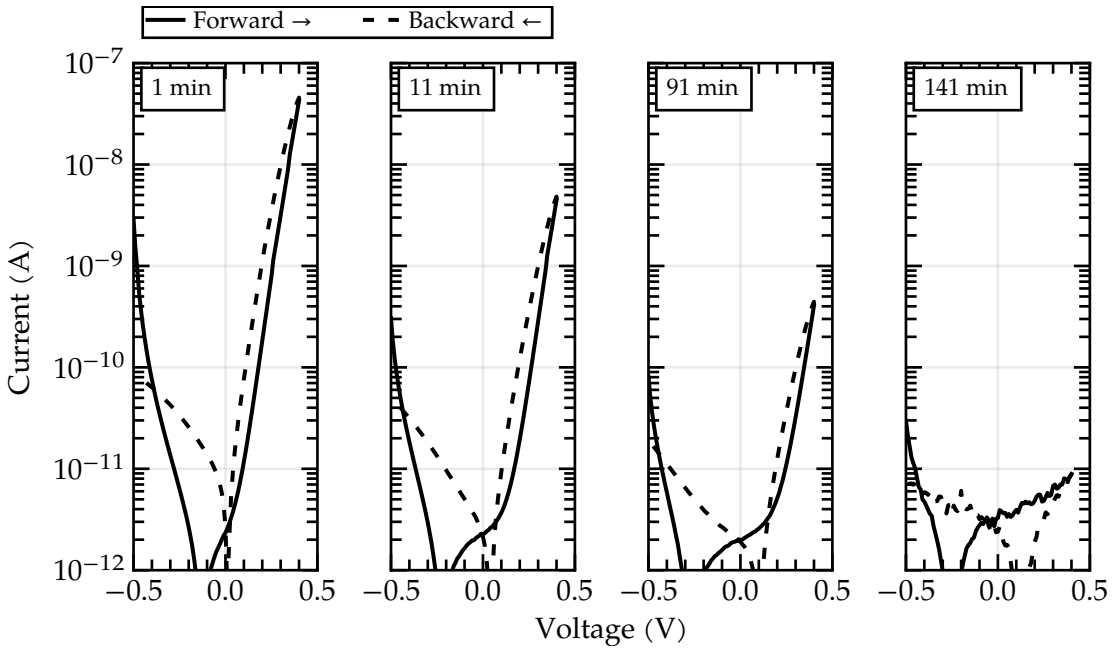

Figure 5.30: Decrease of conductivity of a stoichiometric $SrTiO_3$ thin film over time after performing resistive switching sweeps.

also observed for off-stoichiometric samples, but on much longer time scales of days to weeks.

This raises the question, how oxygen vacancies diffusion, which is normally used for explaining resistive switching, can lead to such a behavior. The fast migration of oxygen vacancies is explained by Joule heating of filaments. But without applying voltages to the thin film, no Joule heating can lead to fast oxygen vacancy migration. Still the resistivity increases after a few minutes. This discrepancy with the established filament model is discussed further in chapter 5.4.

Instead, an activation of a defect, e.g. by trapping or detrapping of charges, can explain this phenomena. The results indicate, that the resistive switching is dependent on the off-stoichiometry of the sample. Especially, the Sr deficiency, and thus, also the Ti_{Sr} antisite defect concentration might play a role in the resistive switching mechanism. How the Ti_{Sr} defect can lead to the resistive switching will also be discussed in chapter 5.4.

The stoichiometric sample still shows a weak on-off ratio, indicating, that it is not perfectly stoichiometric. Also, the current-voltage curve shown in figure 5.27(c) still shows a hysteresis. In the rectifying direction, also plateaus are forming with a constant current at changing voltages. Such plateaus were also found in chromium doped $SrTiO_3$ thin films.[133]. Hopping conduction between traps were found as the origin for this feature. A similar mechanism might play a role in these thin films, as traps-assisted tunneling was also already identified as the transport mechanism for the LRS. Thus, a hopping conductivity over V_{Sr} (or Ti_{Sr}) can be concluded as the transport mechanism through the thin film.

5.3.4 Summary

The resistive switching of MOVPE grown $SrTiO_3$ thin films was investigated. It was shown that the bands are continous at the substrate - thin film interface are continous for the LRS, resulting in a thermionic like conduction in the LRS for positive voltages. In the negative voltage range, the current of the LRS is dominated by trap-assisted tunneling. It was shown, that the switching to the HRS is gradually and parallel conduction paths for the HRS and LRS exists in the negative voltage region. The HRS itself is dominated by Schottky emission.

Due to this, the HRS is strongly dominated by temperature and the conductivitiy of the HRS is decreasing at lower temperatures. Due to this, the best on-off ratio of up to 1×10^7 was found at 10 K. It was also shown, that there is a threshold voltage for the switching and above the threshold voltage, the states can gradually switched over several orders of magnitude between on and off states.

A dependence of the on-off ratio to the Sr defiecency was found and highly off-stoichiometric samples show stronger resistive switching than nearly stoichiometric ones. Additionally it was found, that the switching in the nearly stoichiometric sample is not stable and shows an ´´activation" of the conductivity. The activation is reversible and depends on the stoichiometry. For stoichiometric samples, the time scale is minutes, but this can increase to weeks for off-stoichiometric samples.

The results raise big questions, if resistive switching in these samples can be explained by oxygen vacancy diffusion. Thus, in the next chapter, the existing models will be tested for compatibility and an alternative explanation for the resistive switching mechanism will be presented.

5.4 RESISTIVE SWITCHING MODEL BASED ON THE Ti_{Sr} ANTISITE DEFECT

$SrTiO_3$ was grown epitaxially by MOVPE and stoichiometric as well as non-stoichiometric samples were investigated by coworkers with various methods like STEM-HAADF, STEM-EDX, x-ray diffraction. The epitaxial growth and the x-ray diffraction analysis were performed by Aykut Baki and the transmission electron microscopy measurements by Tobias Schulz (see chapter 5.1). The following section was submitted for publication and is currently under peer-review.[8] The electrical characterization as well as the development of the resistive switching model with the Ti_{Sr} is part of the present work.

The controllability of Sr deficiency was shown by high resolution x-ray diffraction. STEM-EDX has shown a strontium deficiency of up to 20 %, which did not influence the singlecrytallinity of the thin film, which was shown by STEM-HAADF. Recent investigations with STEM-EELS (electron energy loss spectroscopy) have additionally confirmed, that the thin films are not oxygen deficient and have a small excess of Ti (chapter 5.1).

In Sr-deficient samples, a cloudy pattern is visible in STEM-HAADF, caused by diffuse scattering. Density functional theory (DFT) calculations were used to simulate the cloudy pattern. For this, supercells containing different types of defects, V_O, V_{Sr} and Ti_{Sr} were simulated. It was found, that only Ti_{Sr} defects can give the cloudy contrast measured in the STEM-HAADF images. The titanium antisite defect recently gained an increased interest, since it has a permanent dipole moment and different stable positions within the unit cell, thus, can induce ferroelectricity in $SrTiO_3$. This is in agreement with the permittivity measurements, which have shown the formation of polar nano regions for highly

off-stoichiometric samples. Further details from the structural characterization can be found in chapter 5.1.

The comprehensive investigations clearly point towards Ti_{Sr} defects as the dominating defect in the MOVPE grown $SrTiO_3$ thin-films. Due to the high oxygen partial pressure during MOVPE, in contrast to pulsed laser deposition and molecular beam epitaxy, which take place in high vacuum and ultra high vacuum, respectively, the formation of V_O is unlikely and no indication of a significant concentration of this defect was found in any investigation. Beside of that, the thin films were highly insulating, which means that either no oxygen vacancies exists in the thin film, or that they are compensated and thus not contributing to n-type conductivity in the thin film.

The electrical measurements, however, have shown hysteresis behavior in off-stoichiometric samples even without a forming pulse. This indicates, that the thin film itself already brings the capability of resistive switching and the driving defect for the switching is already present in the pristine thin film. This makes it reasonable to take alternative models for resistive switching under consideration.

5.4.1 Established models from literature

Prior to introducing a new resistive switching model, the established models for resistive switching are tested for compatibility with the resistive switching observed in the $SrTiO_3$ thin films of the present work. The two commonly used models, filament switching and valence change switching, are discussed in the following.

Filament switching

Filament switching was established as one of the first models for resistive switching and is based on an dielectric breakdown, which is triggered by an high voltage pulse.[11,35] This forms oxygen vacancies.[171] Oxygen vacancies are shallow donors in $SrTiO_3$,[76] thus this filament is providing a conductive path through the insulating thin film. Indirect proof of these filaments were shown by e.g. conductive hot-spots[172], valence change of titanium shown by STEM-EELS[42] and SrO segregation[65] after the forming pulse. Supporting simulations were done to calculate the dynamics of the filament switching.[92,104] As a result, the simulations showed a thermally supported drift of the oxygen vacancies.[92,104] Due to the small spatial size of the filaments, temperatures of several thousand kelvin and switching speeds in the nanosecond range can be achieved.[104] To switch these devices, they are often driven in compliance current, especially for

switching from LRS to HRS. This means that the current through the filament is limited (to prevent further growth of the filament). The switch from HRS to LRS is often observed as a jump of several orders of magnitude in current. This type of switching is frequently found in Ti-deficient samples.

Filament forming is a mechanism, which is independent from contact size, since the current density is defined by the filament dimensions. One strong argument against the filament model would thus be a current proportionally scaling with the contact size. For electrical characterization, metal electrodes were deposited through a shadow mask by e-beam evaporation, which consists of three electrode sizes with contact areas of $1.77 \times 10^{-4}\,cm^2$, $3.14 \times 10^{-4}\,cm^2$ and $7.07 \times 10^{-4}\,cm^2$. The difference in total current between the smallest and largest contact would be a factor of 4, if the current scales with the contact area. However, the deviations between two electrodes of the same size can be by a factor of 10. Thus, the inhomogeneity in the thin film or the resistive switching is too high to show the scaling of the current with the contact area. Using significantly larger contacts would lead to a compliance in current measurement and is a limiting factor. Smaller contact require more advanced electrode preparation. To this date, these challenges have prevented a final conclusion as to whether the current scales with contact size.

Samples that exhibit resistive switching via conductive filaments typically require a forming pulse. However, this was not necessary for the $SrTiO_3$ thin-films grown by MOVPE and forming-free resistive switching was demonstrated.

Some literature reports have demonstrated forming-free resistive switching based on filaments.[66] In this case, anti-phase boundaries were intentionally introduced to the thin film by using a high off-cut and high lattice mismatch substrate. Phase boundaries act as preformed filaments in such a case and the switching mechanism is based on the release and reintroduction of oxygen into the phase boundary.[66]

These anti-phase boundaries were not identified so far in the investigated thin films and are more likely in titanium deficient thin films due to the formation of Ruddlesden-Popper phases. The experiments in the present work were performed at 10 K in high-vacuum. Consequently, released oxygen can't be reintroduced from the atmosphere into the anti-phase boundaries. There is a possibility, that the oxygen is diluted in the electrode, however, the diffusion and dilution of oxygen in platinum is very low. In addition, the measurements in the present work have shown an increase in resistivity after the first sweep. However, if oxygen is released from the sample during this sweep, a decrease of resistivity is expected.

Another argument against switching based on filaments is the following. After the initial forming step the conductive filament spans the whole film thickness. By switching to the HRS this filament is ruptured only locally near the contact, i.e. the formed non-conductive gap is much smaller than the film thickness. Hence, both the height and width of the potential barrier for emission and tunneling currents in the HRS are much lower than in the virgin state of the film. Combined with the electric field enhancement at the ruptured filament top, one has to expect in the HRS a much higher conductivity than in the virgin layer. The thin films discussed in the present work have a HRS which shows a lower current, which would be contrary to the filamentary model.

The forming-free resistive switching as well as the decrease of conductivity during the first sweep are strong indications, that filament switching does not occur in the investigated thin films. However, to finally proof this, further investigation regarding the scaling of the current with the contact area are needed.

Valence change switching

Valence change switching is based on the drift of oxygen vacancies in the thin film without the need of conductive filament. The switching is achieved either by a change of Schottky barrier height or by a change in the space charge region width by redistributing oxygen vacancies in the thin film.[129,190] Thin films with this switching mechanism do not necessarily need a forming pulse, but a soft-forming sweep.[66] During this sweep, oxygen is released from the thin film to the air or to the electrode. This was supported by experiments, which included an additional thin layer of titanium below the platinum electrode. However, with increasing titanium thickness of up to 10 nm, the LRS/HRS ratio decreased and the total current increased, probably due to the lower work function of the titanium. The current-voltage characteristics of valence change switching differs from the filament switching model. In this case, no jump from HRS to LRS is observed, but a continuous transition.

Qualitatively, the current-voltage curves shown for valence change switching are similar to the current-voltage curves in this study.[168] However, oxygen is released (soft-forming) from thin films which show valence change resistive switching and thus reducing the overall resistance of the thin film. As shown in figure 5.20 (p. 71), the HRS shows a current of at least two orders of magnitude lower than the initial state at $-1\,\mathrm{V}$.

5.4.1.1 Ferroelectric switching

Even though $SrTiO_3$ is not ferroelectric, it was pointed out in chapter 5.2 that ferroelectricity can be induced by e.g. strain and defects. One of the defects inducing a ferroelectricity is the Ti_{Sr} defect, which was found in the thin films in high concentrations. Further work is needed to confirm the ferroelectricity in the MOVPE grown thin films, but so far, temperature dependent permittivity measurements have shown good indication for a stable polarization in the thin films. The strength of the relaxor ferroelectric behavior was dependent on the cation ratio in the thin films and stoichiometric thin films haven't shown relaxor ferroelectric behavior. Permittivity measurements have shown good agreement with the proposed dependence on defect concentration by Choi et al.[26]. Thus, a resistive switching based on the Ti_{Sr} has to be considered.

Klyukin et al.[86] have calculated, that resistive switching based on the Ti_{Sr} antisite defect is possible, induced by a change of tunnel electro resistance for the different polarizations. Lu et al.[101] have found tunneling hotspots in strain-free, ferroelectric $SrTiO_3$ by measuring conductive AFM.(2) The number of conductive spots increase for the LRS and decrease for the HRS and have a diameter of 10 nm to 20 nm. With increasing film thickness, no conductive spots were detected anymore.

Thus, resistive switching based on ferroelectric switching is limited to very thin layers, below e.g. 10 nm. The tunnel mechanism is mostly described as direct tunneling or Fowler-Nordheim tunneling.[58]. For direct tunneling, the amplitude decays exponentially with the film thickness and thus limiting the layer thickness. Fowler-Nordheim tunneling describes the tunneling through a triangular barrier. To reduce the width of this barrier, a strong bending of the bands and thus very high electric fields have to be achieved, and thicker layers reduce the field strength in the layer at same applied voltages.

In the work of Lu et al.[101], the limit for resistive switching was at roughly 36 unit cells ($\approx$ 18 nm) film thickness (see also ref. [96]), in which the switching was shown up to 24 unit cells layer thickness).

In the present work, stable resistive switching was shown for 40 nm film-thickness. The difference to ref [101] is the higher concentration of up to 20 % Sr deficiency compared to 1 %. The higher density of Ti_{Sr} could stabilize the ferroelectric domains even for thick layers. This is also confirmed by the observation, that less Sr-deficient layers show a weaker resistive switching. However, a

(2) Conductive hotspots were also found in early studies about resistive switching in $SrTiO_3$, but were attributed to filamentary conduction along dislocations.[172]

direct tunneling mechanism would be still prevented by the film thickness.

It was shown, that the transport mechanism in the LRS is based on trap-assisted tunneling. In trap-assisted tunneling, the limitation is the distance between the trap sites. The film thickness is not the limiting factor anymore. As a consequence, a model combining a trap based mechanism is suggested through the thin film and switching occurs by changing the barrier at the interface between thin film and substrate. The electrical transport model is described in the next chapter 5.4.2.

At this point, further agreements of the measured data with the model is discussed. An important features is the gradual increase of the on-off ratio with the switching voltage (figure 5.23 on p. 73). This was also observed in ferroelectric tunnel junctions (FTJ) based on $BaTiO_3$.[24] Chanthbouala et al.[24] explain the gradual switching by a nucleation and growth of ferroelectric domains by applying an external field.

It also explains why no stable resistive switching is observed in the stoichiometric sample, even though the current-voltage curve shows a strong hysteresis between forward and backward direction. If ferroelectric domains are needed to stabilize the switching state, the density in the stoichiometric sample could be too low to form ferroelectric domains. But still, Ti_{Sr} antisite defects can exists in a low concentration. The external field, as long as it is applied, will also still force the defects into one polarization, which then leads to the insulating or conductive state, but the state will not persist after removing the external field.

To conclude, the ferroelectric switching based on the Ti_{Sr} is the most likely switching mechanism in the MOVPE grown $SrTiO_3$ thin films. In the following, the electrical transport model will be described.

5.4.1.2 Defect related electrical transport

Different mechanism, considering ferroelectricity as the switching mechanism, are possible. One idea would be, that different stable positions of the Ti_{Sr} in the unit cell have a different energy level within the band gap. Indeed, Choi et al.[26] calculated, that the energy level differs for the [100] and [110] configurations. Choi et al. calculated a trap depth of 0.96 eV and 1.12 eV for the isolated Ti_{Sr} on the [100] and [110] configurations, respectively. The work of Klyukin et al.[86] has shown that small difference in the defect configuration lead to a strong difference in tunneling propability for a few unit cells thick thin film.

The model of Choi et al.[26] needs to be adjusted to explain the observations of the present work. A pure tunneling mechanism as it was described in ref. [86] would require very thin layers with

only a few unit cells width. In the present work, thin films of 40 nm thickness are used, which reduces the tunneling probability and can't explain the high currents of the LRS. But due to the differences of the trap depth in the band gap, a mechanism based on the change of the fermi level would be a possibility. Raebiger et al.[141] suggested a mechanism based on charging and decharging of traps. For the LRS, he suggests that the traps are not ionized and thus the fermi level is close to the conduction band. For the HRS, the traps are ionized. In this case, the fermi level is in the center of the band gap and the thin film is insulating. The model would be in good agreement with the gradual switching shown in chapter 5.3.2. Yet, the model is based on the fact that the electrons in the LRS cannot emit from the trap sites due to Schottky barriers formed at both interfaces. This usually is the case for metal-semiconductor-metal structures. In the present work, the interface between thin-film and substrate shows continous bands, which would allow the traps to emit the charge carriers and get ionized, thus leading to a fast transition to the HRS.

Mojarad et al.[109] investigated the electrical transport of a Pt – $SrTiO_3$ – Pt structure and found a combination of trap-assisted tunneling and Poole-Frenkel conduction. The work does not show resistive switching, but showed an asymmetry in current-voltage characteristics, even though the structure itself is symmetric. The authors claim a non-uniform distribution of V_O leads to the asymmetry in current-voltage characteristics. On the interface with a lower oxygen vacancy concentration, the charge carrier injection into the thin film is lower and based on trap-assisted tunneling, whereas the transport through the thin film itself is based on Poole-Frenkel conduction. The authors also observe a unique feature seen in the stoichiometric samples of the present work, the reversal of current before passing through zero bias, but are not discussing this observation any further. The barrier heights of the combined transport of trap-assisted tunneling and Poole-Frenkel emission were 0.13 eV to 0.11 eV and 0.90 eV to 0.55 eV, respectively.

Even though the results by Mojarad et al.[109] show good agreement with the current-voltage curves measured in the present work, a slightly different approach is chosen for explaining the transport. The current in the LRS is dominated by tunneling and contrary to the work of Mojarad et al., no contribution of Poole-Frenkel emission was measured. Instead, in the present work, it is expected, that trap-assisted tunneling is the dominating transport mechanism through the thin film and the emission current is the limiting contribution for the HRS.

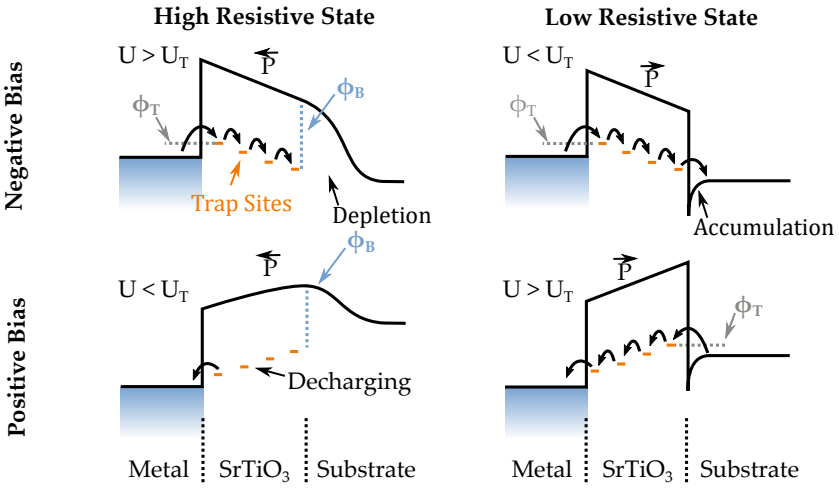

Figure 5.31: Schematic band diagram of the trap-assisted ferroelectric tunnel junction. $|U| < |U_T|$ is the state below the threshold voltage, $|U| < |U_T|$ the state above the threshold voltage. The polarization leads to either a accumulation or depletion at the interface between thin film and substrate. The depletion leads to an additional barrier, which is blocking the charge carriers and thus increasing the resistivity. In the low-resistive state, the current is dominated by trap-assisted tunneling, which has a small barrier height.

5.4.2 Model of the electrical transport

Up to this point, the following observations have been made to serve as the basis for the resistive switching model. First, it was found that the Ti_{Sr} induces ferroelectricity in the thin films. Therefore, depending on the polarization direction, polarization charges form either at the electrode interface or at the substrate interface. This was measured via a change in the permittivity of the layer for the HRS and LRS. The current voltage characteristics show a diode-like behavior. In the HRS, the current is dominated by Schottky emission. In the LRS, charge transport takes place via thermionic emission for positive voltages (forward direction) and via defect-assisted tunneling for negative voltages (reverse direction). In the case of stoichiometric samples, a discharge current that reverses the current direction is observed for the negative voltage direction.

Figure 5.31 shows the suggested transport mechanism. Like in a metal-insulator-semiconductor structure, a depletion or a accumulation zone near the thin film - substrate interface can form. Due to the ferroelectricity in the thin film, the depletion/accumulation is stabilized by the polarization, even with changing the field direction up to the threshold voltage. Above the threshold voltage, the polarization of single polar nano regions will switch and lead to an gradually switching between LRS and HRS.

The state thereby mainly depends on the depletion or accumulation at the thin film - substrate interface. In case of the HRS, a depletion layer forms. The charge carriers can overcome this depletion layer by e.g. Schottky emission. The emission current is temperature dependent. This confirms the observation, that the HRS strongly increases in current with increasing temperatures. The HRS is switched in the negative voltage range, in which the charge carriers are injected from the metal electrode into the thin film and then blocked by the depletion layer. In the HRS with applied positive bias, the barrier height of the depletion zone will decrease due to band bending. This eventually leads to an increased emission current by injecting charge carriers from the substrate to the thin film, if the barrier height is sufficiently lowered before switching the polarization of the thin film.

In the LRS, no blocking depletion layer is suppressing the current and the current is dominated by trap-assisted tunneling. In good agreement with the measurements, the LRS is expected to be more symmetric for the positive and negative bias region. The only difference might come from different barrier heights between metal electrode - traps and substrate - traps.

The model is also in good agreement with a frequently observed change of Schottky barrier height in Pt-$SrTiO_3$:Nb. This is generally explained by the occurrence of a interfacial dielectric layer and the diffusion of oxygen vacancies, which leads to a change in barrier height. Bourim et al.[15] e.g. have found a combination of tunneling and emission current at the interface of a resistive switching $SrTiO_3$:Nb Schottky diode with an dielectric interface layer. They measured the charge carrier lifetime, which was shorter for the LRS. This can be a hint for hole conduction in the $SrTiO_3$ layer. Since an accumulation layer (of electrons) forms at the $SrTiO_3$- substrate interface in LRS, the holes can, similar to a pn-junction, recombine with electrons, whereas for the HRS, the depletion layer would prevent this.

A support for the model of a trap-assisted ferroelectric tunnel junction is the LRS-HRS ratio based on the switching voltage (chapter 5.3.2). Multistate switching in ferroelectric tunnel junctions was shown by Chanthbouala et al., who have shown a dependence of the device resistance on V_{write}.[24], which is explained by the gradual growth of domains. The same was shown for the thin films of the present work and is hardly explainable by V_{O} diffusion.

Several features of the current-voltage characteristics of the stoichiometric sample can also be explained by this model. Even though no stable switching was shown, a hysteresis was measured, which indicates that still Ti_{Sr} defects are present in the thin film, but in a too low concentration to form polar nano regions. One of the observations was a reversal of current direction in the

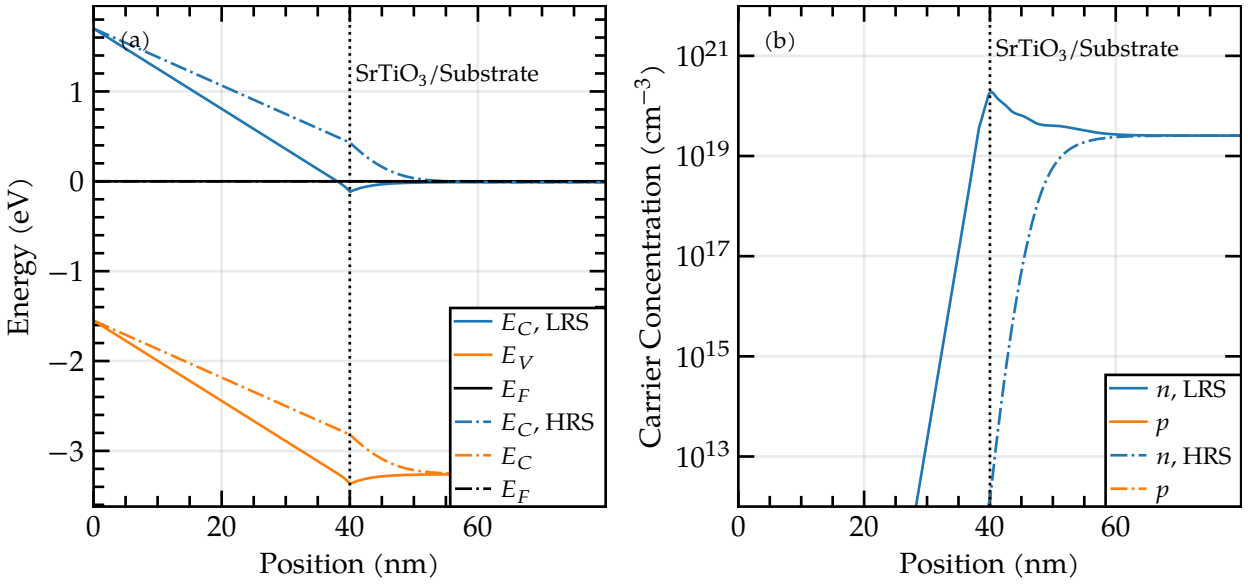

Figure 5.32: (a) Simulated band structure of the suggest trap-assisted ferroelectric tunnel junction in low and high resistive state. The Fermi level is at 0 eV. The vertical dashed line represents the interface of thin film and substrate. (b) The corresponding charge carrier concentration. The hole concentration is negligible.

HRS in the negative bias region, which means that some electric field, stronger than the externally applied field, leads to a reversal of current. In the case of ferroelectricity induced by the Ti_{Sr} defect in the thin film, a stable electric field exists in the thin film. Thus, the reversal of current, induced by the ferroelectric field in the thin film, can be explained by decharging of the traps from the thin film to the platinum electrode.

Another characteristic feature of the current-voltage hysteresis were plateaus in the reverse current of the backward direction (figure 5.27(c)) This behavior was described as trap controlled conduction in Cr-doped $SrTiO_3$.[133] Thus it is a confirmation of the idea, that tunneling or hopping between localized trap sites is the dominating factor in conduction through the thin film.

A first approach was done to simulate the device using a 1D Poisson solver. The tool `1D-DDCC` by Wu et al.[198–200] was used. The relevant material parameters are shown in table 5.3. A structure consisting of a Pt contact, a 40 nm thick $SrTiO_3$ thin film and a $SrTiO_3$:Nb substrate with a n-type doping concentration of $1 \times 10^{20}\,cm^{-3}$ was used. The device was simulated at 0 V using two polarizations of the same magnitude, but of reversed direction, $\overleftarrow{P}$ and $\vec{P}$. The band structure and electron concentration is shown in figure 5.32. Confirming the suggested model, a depletion zone is forming for the $\overleftarrow{P}$ polarization, and a accumulation layer for the case of the $\vec{P}$ polarization.

In the next step, the device is simulated with applying bias. In figure 5.33, the band structure and the charge carrier concen-

Band gap	3.25 eV[88]
Electron Affinity	3.9 eV[147]
Pt Work function	5.6 eV[106]
ε_r (layer)	80 (this work)
ε_r (substrate)	300 (this work)
Temperature	300 K
Electron Mobility	$5\,cm^2\,V^{-1}\,s^{-1}$[111]
Polarization	$16.8\,\mu C\,cm^{-2}$[85]

Table 5.3: Material parameter used for simulating trap-assisted FTJ.

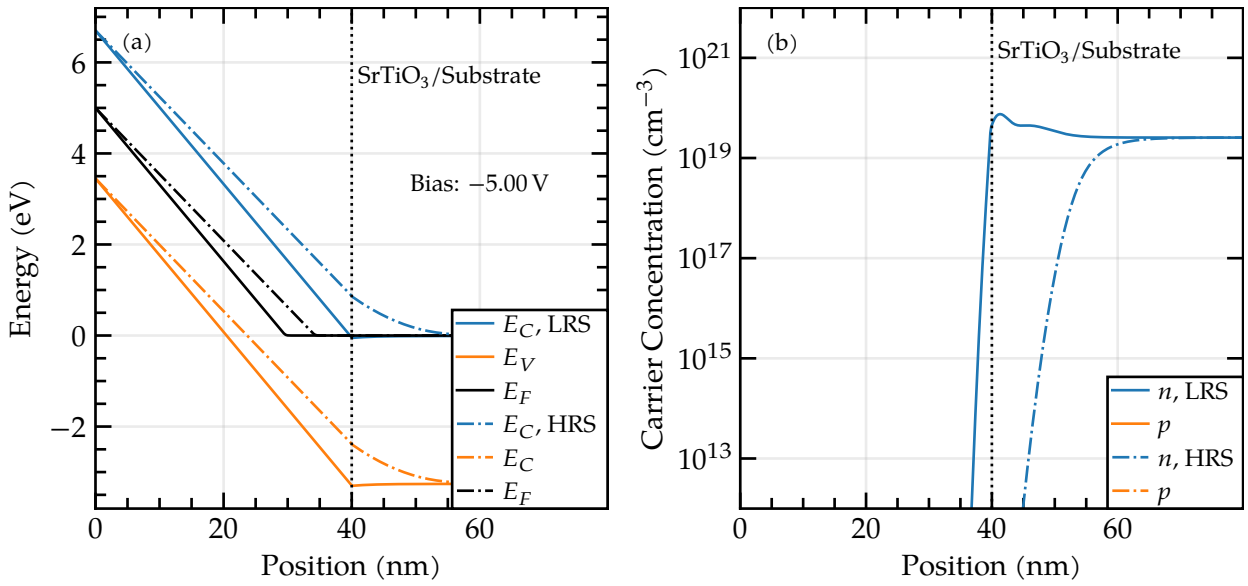

Figure 5.33: (a) Simulated band structure at −5 V of the suggest trap-assisted ferroelectric tunnel junction in low and high resistive state. The vertical dashed line represents the interface of thin film and substrate. (b) The corresponding charge carrier concentration. The hole concentration is negligible.

tration for a negative bias of −5 V is shown. So far, no tunneling of charge carrier could be simulation. Still, the figure gives some hint for the difference between LRS and HRS. In the case of the LRS, donors exists even close to the interface in the $SrTiO_3$ thin film. With trap-assisted tunneling, charge carriers can pass through the thin film. An alternative with holes in the thin film would be a conduction like in pn junction in forward direction with recombination of holes and electrons at the interface. For the HRS however, the depletion layer at the interface prevents injection through the interface. Charge carriers would need to emit over the barrier via Schottky emission, like it was measured for the real devices.

In figure 5.34, the situation in positive voltage range is shown. Charge carriers are injected into the thin film for both states, however, the depletion leads to a strongly reduced charge carrier concentration of around two orders of magnitude. This, e.g., fits well to the measurements in chapter 5.3.3, were the positive voltage range shows a high current for both states.

5.4.3 Conclusion

Resistive switching in homoepitaxially grown MOVPE $SrTiO_3$ thin films were tested for compatibility with existing models of resistive switching. Especially the forming-free switching in the $SrTiO_3$ is a new observation, which is hardly compatible with filamentary switching. Beside of that, the most dominant defect

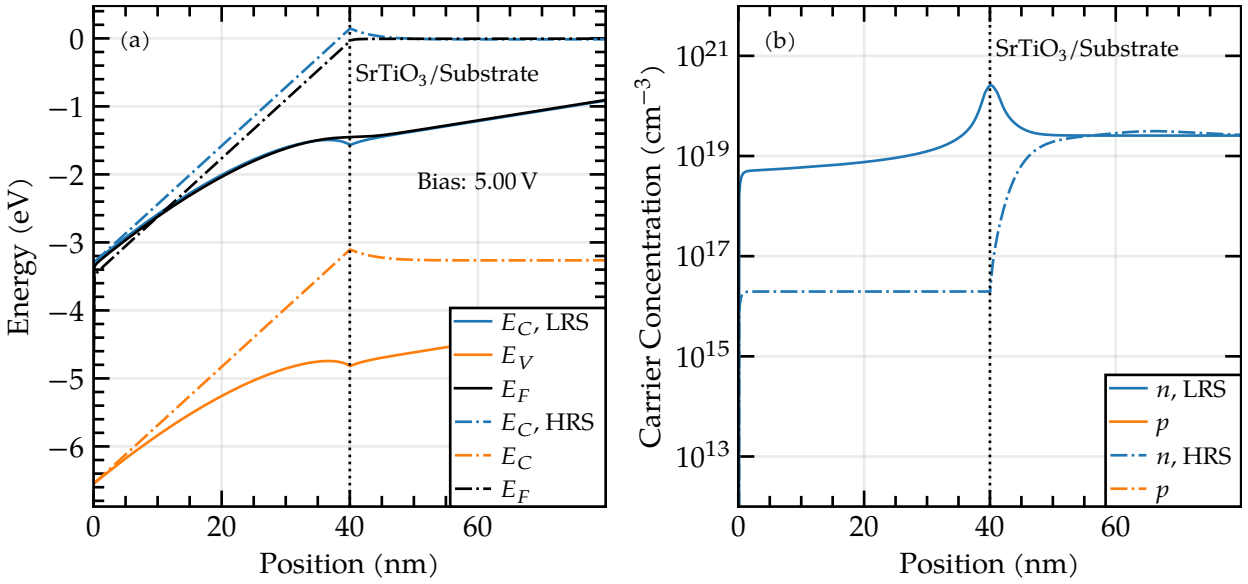

Figure 5.34: (a) Simulated band structure at 5 V of the suggest trap-assisted ferroelectric tunnel junction in low and high resistive state. The vertical dashed line represents the interface of thin film and substrate. (b) The corresponding charge carrier concentration. The hole concentration is negligible.

in the thin films is the Ti_{Sr} antisite defect, which is inducing a ferroelectricity in the thin films.[26] V_O are probably negligible due to the high oxygen background pressure during growth.

Ferroelectric $SrTiO_3$ tunnel junctions were already demonstrated for ultra thin layers using this defect, but was limited to a few unit cells.[101] Temperature-dependent permittivity measurements also indicated a ferroelectricity in the MOVPE grown layers of the present work and a good agreement with the predicted dependence of the permittivity to the Ti_{Sr} concentration[85] was found in the layers discussed in the present work, a model was developed to explain the resistive switching without the formation of filaments and without the diffusion of V_O.

The developed model is based on trap-assisted tunneling through the thin film. The resistive switching is then performed by changing the polarization of the Ti_{Sr} antisite defect. Surface charges at the interface to the substrate then lead to a accumulation or depletion layer, which leads to the LRS and the HRS, respectively. The current-voltage measurements are in good agreement with this model. A further support of a ferroelectric switching effect is the gradual switching between the state, which was shown for ferroelectric tunnel junctions and is related to the growth of ferroelectric domains.[24]. Also the dependence of the off-stoichiometry can be directly correlated to the antisite defect concentration. In a stoichiometric sample with a low Ti_{Sr} concentration, no stable domains can form, thus no stable LRS and HRS can be set. Temperature dependent measurements have shown a strong temperature dependence of the HRS, but not of the LRS, which is further

supporting the model, in which a depletion region is blocking the current, and residual conductivity is based on emission current. A change of permittivity with switching the device between LRS and HRS can also be an indication of the formation of depletion and accumulation zones in the substrate. Finally, a reversal in current from negative to positive was measured for the stoichiometric sample in the negative voltage range, which indicated an internal electric film in the thin film.

Simulations of the band bending expected in the device structure are in good agreement with the suggested qualitative model. Calculation of I-V curves however, would need including tunneling currents in the simulations.

Several experiments can be performed to confirm this model and especially more work on determining the ferroelectricity in the thin films are needed. A thickness series is one of the most important experiments to proof the model. In thinner layers, the conductive hotspots should occur and the ferroelectricity should be measurable. Finally, the scaling of the film-thickness will provide further insight into the conduction mechanism, which is generally dependent on the field strength. Also, the resistive switching might be influenced by the doping concentration of the substrate, as the space charge region is forming within this region. This would also lead to different permittivity values for the LRS and HRS in dielectric measurements.

For characterizing the ferroelectricity, several experiments can be performed. First of all, temperature dependent permittivity measurements can be performed using different measurement frequencies. Using the Vogel-Fulcher equation, the freezing temperature of the ferroelectric domains can be determined.[185,186] Additionally, piezo-force microscopy can be performed to identify hotspots or stable ferroelectric domains. It is not necessarily expected to see such hot spots, since the occurrence were limited to ultra thin layers[96,101].

A direct proof of ferroelectric switching of the Ti_{Sr} antisite defect might be possible using in-situ experiments. On going effort is done using in-situ STEM and in-situ x-ray diffraction experiments. First attempts in performing an in-situ current-voltage curve in an STEM experiment have shown a shift in contrast between the top and bottom electrode during the sweep. However, no atomic resolution could be obtained in this experiments due to sample thickness. Further experiments are planned. Additionally, first attempts in using resonant x-ray diffraction were done in October 2020 at the DESY synchrotron beamline P23. Even though a displacement in the unit cell could be measured by switching the sample between the LRS, HRS and read-out voltage, no clear stable ferroelectric switching was measured and the effect might result from the displacement of Ti in the unit

cell due to the electric field (which is measurable as the field-dependent permittivity). A reason could be a too low sensitivity on the defect displacement due to background from the substrate. Another problem during the experiment was the strong photoconductivity during the illumination of the sample with the synchrotron beam. Further experiments will require either thicker samples or the growth of $SrTiO_3$ on foreign substrates to reduce the background noise and increase the sensitivity to measure the polarization of the Ti_{Sr} defect. Additionally, low-temperature experiments can stabilize the ferroelectric polarization during the experiment.

6 SUMMARY AND OUTLOOK

In the present work, the impact of crystal defects on the resistive switching in the materials $SrTiO_3$ and NbO_2 is investigated. The work is structured in two parts.

The investigations of NbO_2 (001) thin films deposited on MgF_2 (001) are presented in the first part. These were epitaxially grown by pulsed laser deposition. NbO_2 is a material that exhibits an insulator-metal transition, which can be induced thermally at 1080 K, or by external electric fields at room-temperature, making it interesting for threshold switching applications.[2,75,161] So far, thin films in the insulating phase have shown lower resistivities[50,79,123,191] compared to the resistivity of NbO_2 single crystals, which is 10 kΩ cm.[75] To make this material applicable for threshold switching devices, the resistivity in the insulating phase has to be increased to effectively block the current in the high resistive state.

Throughout the investigations presented in this work, the resistivity of NbO_2 thin films was increased to 945 Ω cm. For this, the NbO_2 was annealed at 880 °C after epitaxial growth, increasing the grain diameter by a factor of 10 to 60 nm. It was shown that conductive percolation paths along the grain boundaries are responsible for the decrease in resistivity. The reason for this is the disturbance of the Nb d-orbital dimerization at the grain boundaries, which results in a collapse of the band gap and thus in the local formation of the metallic phase.

So far, band gap energies have been reported from 0.28 eV to 1.16 eV.[2,98,125,150,197] This can be attributed to the local perturbations of the dimerization by crystal defects leading to a collapse of the band gap. Using temperature-dependent resistivity measurements, it was shown that the intrinsic conductivity of NbO_2 exceeds the defect-related conductivity at temperatures higher than 650 K. From the intrinsic conductivity, a bandgap energy of 0.88 eV was determined. In addition, the band gap energy was determined optically at room temperature using spectroscopic ellipsometry and absorption spectroscopy. An energy of 0.77 eV was measured for the optical band gap at room temperature. Thus, a significant improvement in the electrical properties of the NbO_2 thin films could be obtained, which is prerequisit to achieve satisfactory high-resistance states in NbO_2 based switching devices.

The next step is to demonstrate the switching behavior of the NbO_2 thin films. For this purpose, it is necessary to deposit appropriate electrodes on the material. Challenging here is the fabrication of a backside contact, since MgF_2 is an insulating substrate. It would be possible, for example, to deposit NbO_2 on other substrates, e.g. gallium nitride, or on a metallic back electrode such as platinum.

In the second part of the work, the influence of the Ti_{Sr} defects on resistive switching in $SrTiO_3$ thin films grown by metal-organic vapor phase epitaxy is investigated. The thin films were deposited with different Sr/Ti ratios, which allowed the degree of strontium deficiency in the thin film to be controlled. In the strontium deficient layers, the formation of the Ti_{Sr} defect was shown.

It was shown that the soft phonon mode in $SrTiO_3$ was hardened with the degree of strontium deficiency, resulting in a significantly weakened temperature dependence of the permittivity. For very highly strontium deficient films, it was also shown that polar nano regions were formed. These polar nano regions were attributed to the Ti_{Sr} defect. The Ti_{Sr} defect has a permanent dipole moment and can therefore induce ferroelectricity in $SrTiO_3$.[26] Due to the formation of the polar nano region, it was concluded that the defect must be present in a high concentration.

Due to the high concentration of Ti_{Sr} defect, the impact on resistive switching was investigated. It could be shown that the on-off ratio increases with increasing strontium deficiency. Thus, at 10 K, a maximum on-off ratio of 2×10^7 could be measured for a strongly strontium deficient layer. In contrast, a nearly stoichiometric layer shows only a weak resistive switching ratio of 2. Moreover, the resistive switching states are not stable and decay within a few minutes, whereas switching in strontium deficient layers is stable over several days. A significant advantage over previous reports of resistive switching in $SrTiO_3$ is that no forming step was needed to activate the resistive switching in the MOVPE grown $SrTiO_3$ thin-films of the present work.

These observations were tested for their consistency with the filament model and the valence change model, which have previously been used to describe resistive switching.[42,129,171,190] These models cannot satisfactorily explain switching in the MOVPE grown layers, so a new model based on the Ti_{Sr} defect was developed. This was based on the analysis of the electrical transport in the HRS and LRS.

Current-voltage measurements have shown a diode-like electrical transport. This is dominated by Schottky emission in the HRS. In the LRS, the transport mechanisms differ for positive and negative voltages. For positive voltages, in the forward direction, a thermionic emission current dominates, whereas for negative voltages a defect-assisted tunnel current prevails. It was shown

that in the LRS for negative voltages, the tunnel current flows in parallel with a lower Schottky emission current.

Poisson simulations were used to show that the resistive switching mechanism is based on the fact that the polarization charges induced by the Ti_{Sr} defect affect the interfacial charges between the thin film and the substrate. In the case of HRS, the polarization charges lead to the formation of a depletion layer that acts as a barrier. In this case, the charge carriers have to overcome the barrier by Schottky emission.

In the LRS, the polarization charge causes the charge carriers to accumulate at the boundary layer, hence no barrier limits the current flow. This allows the charge carriers to flow via thermionic emission via the conduction band from the substrate across the thin film into the electrode. In reverse direction on the other hand, the conduction mechanism works via defect states in the thin-film, which means that the defect-assisted tunnel current limits the charge carrier transport.

Until now, the forming step has been a major hurdle for industrial applications because filament formation is difficult to control and therefore reproducible switching voltage and currents are not achieved. In $SrTiO_3$ films fabricated by MOVPE, this step is eliminated and thus a major hurdle for device reproducibility.

However, several experiments could not be performed within the scope of the present work, which would further support the model and help understanding the device physics. One important measurement is frequency and temperature dependence of the permittivity to further understand the role of polar nano regions in the thin-films. Piezo force microscopy can be an additional method to characterize the ferroelectricity in the thin-films.

Additionally, experiments with in-situ techniques are in preparation. In particular, in-situ transmission electron microscopy experiments as well as x-ray diffraction experiments at the DESY (Deutsches Elektronen Synchrotron)[37] are currently conducted. The aim of these experiments is to measure the change of polarization direction of the Ti_{Sr} antisite defect by switching the device between low resistive state and high resistive state.

Another important experiment is to investigate the role of the space charge region, which is formed in the substrate by the polarization charges. For this purpose, substrates with lower doping levels will be used to increase the size of the space charge region and thus can improve the current blocking in the high resistive state.

The results may pave the way to use resistive switching for commercial applications. To benefit from low power consumption and high switching speed, resistive switching memories must be operated as a crossbar array. Selector devices, such as NbO_2, are necessary to prevent sneak paths. This work was able to iden-

tify the cause of increased conductivity of the insulating phase of NbO_2 and eliminate it through an annealing step, allowing it to be used as a metastable switch.

Previous work on resistive switching in $SrTiO_3$ required a formation step, which is difficult to control and thus problematic to use in commercial applications. By using MOVPE grown, strontium deficient $SrTiO_3$ thin films, a switching mechanism based on the Ti_{Sr} antisite defect was developed which eliminates the need for the formation step. The elimination of this difficult-to-control step opens the way for the commercialization of $SrTiO_3$.

7 BIBLIOGRAPHY

[1] S. C. Abrahams, S. K. Kurtz, and P. B. Jamieson. „Atomic Displacement Relationship to Curie Temperature and Spontaneous Polarization in Displacive Ferroelectrics." In: *Physical Review* 172.2 (Aug. 10, 1968), pp. 551–553. DOI: 10.1103/PhysRev.172.551.

[2] David Adler. „Mechanisms for Metal-Nonmental Transitions in Transition-Metal Oxides and Sulfides." In: *Reviews of Modern Physics* 40.4 (Oct. 1, 1968), pp. 714–736. DOI: 10.1103/RevModPhys.40.714.

[3] Nagaphani B. Aetukuri et al. „Control of the Metal–Insulator Transition in Vanadium Dioxide by Modifying Orbital Occupancy." In: *Nature Physics* 9.10 (Oct. 2013), pp. 661–666. ISSN: 1745-2473, 1745-2481. DOI: 10.1038/nphys2733.

[4] Kaveh Ahadi, Luca Galletti, Yuntian Li, Salva Salmani-Rezaie, Wangzhou Wu, and Susanne Stemmer. „Enhancing Superconductivity in SrTiO3 Films with Strain." In: *Science Advances* 5.4 (Apr. 1, 2019), eaaw0120. ISSN: 2375-2548. DOI: 10.1126/sciadv.aaw0120.

[5] I. A. Akimov, A. A. Sirenko, A. M. Clark, J.-H. Hao, and X. X. Xi. „Electric-Field-Induced Soft-Mode Hardening in SrTiO 3 Films." In: *Physical Review Letters* 84.20 (May 15, 2000), pp. 4625–4628. ISSN: 0031-9007, 1079-7114. DOI: 10.1103/PhysRevLett.84.4625.

[6] Chen Ang and Zhi Yu. „Dielectric Relaxor and Ferroelectric Relaxor: Bi-Doped Paraelectric SrTiO3." In: *Journal of Applied Physics* 91 (2002), p. 1487. DOI: 10.1063/1.1428799.

[7] R. M. A. Azzam and N. M. Bashara. *Ellipsometry and Polarized Light*. ISBN: 978-0-444-87016-2.

[8] Aykut Baki, Julian Stöver, Tobias Schulz, Toni Markurt, Carsten Richter, Klaus Irmscher, Martin Albrecht, and Jutta Schwarzkopf. „Stoichiometry Control for Electrical Properties of MOVPE Grown $SrTiO_3$ Thin Films." In: *Scientific Reports* under review (Oct. 27, 2020).

[9] John H. Barrett. „Dielectric Constant in Perovskite Type Crystals." In: *Physical Review* 86.1 (Apr. 1, 1952), pp. 118–120. DOI: 10.1103/PhysRev.86.118.

[10] Cem Basceri, S. K. Streiffer, Angus I. Kingon, and R. Waser. „The Dielectric Response as a Function of Temperature and Film Thickness of Fiber-Textured (Ba,Sr)TiO3 Thin Films Grown by Chemical Vapor Deposition." In: *Journal of Applied Physics* 82.5 (Sept. 1997), pp. 2497–2504. ISSN: 0021-8979, 1089-7550. DOI: 10.1063/1.366062.

[11] A. Beck, J. G. Bednorz, Ch. Gerber, C. Rossel, and D. Widmer. „Reproducible Switching Effect in Thin Oxide Films for Memory Applications." In: *Applied Physics Letters* 77.1 (June 28, 2000), pp. 139–141. ISSN: 0003-6951. DOI: 10.1063/1.126902.

[12] S. Beucher and C. Lantuéjoul. *Use of Watersheds in Contour Detection*. 1979. URL: /paper/Use-of-watersheds-in-contour-detection-Beucher-Lantu%C3%A9joul/a20974c101f6baf22bda94c4b2d91dc4163d5be7 (visited on 09/17/2020).

[13] A. A. Bokov and Z. -G. Ye. „Recent Progress in Relaxor Ferroelectrics with Perovskite Structure." In: *Frontiers of Ferroelectricity: A Special Issue of the Journal of Materials Science*. Ed. by Sidney B. Lang and Helen L. W. Chan. Boston, MA: Springer US, 2007, pp. 31–52. ISBN: 978-0-387-38039-1. DOI: 10.1007/978-0-387-38039-1_4.

[14] Adrian A. Bolzan, Celesta Fong, Brendan J. Kennedy, and Christopher J. Howard. „A Powder Neutron Diffraction Study of Semiconducting and Metallic Niobium Dioxide." In: *Journal of Solid State Chemistry* 113.1 (Nov. 1, 1994), pp. 9–14. ISSN: 0022-4596. DOI: 10.1006/jssc.1994.1334.

[15] El Mostafa Bourim, Yoonjung Kim, and Dong-Wook Kim. „Interface State Effects on Resistive Switching Behaviors of Pt/Nb-Doped $SrTiO_3$ Single-Crystal Schottky Junctions." In: *ECS Journal of Solid State Science and Technology* 3.7 (2014), N95–N101. ISSN: 2162-8769, 2162-8777. DOI: 10.1149/2.0081407jss.

[16] E. Breckenfeld, R. Wilson, J. Karthik, A. R. Damodaran, D. G. Cahill, and L. W. Martin. „Effect of Growth Induced (Non)Stoichiometry on the Structure, Dielectric Response, and Thermal Conductivity of $SrTiO_3$ Thin Films." In: *Chemistry of Materials* 24.2 (Jan. 24, 2012), pp. 331–337. ISSN: 0897-4756, 1520-5002. DOI: 10.1021/cm203042q.

[17] Stephen L. Brown, Stephen M. Rossnagel, John Bruley, Matthew Copel, Marco J. P. Hopstaken, Vijay Narayanan, and Martin M. Frank. „Oxygen Migration in TiO_2-Based Higher-k Gate Stacks." In: *Journal of Applied Physics* 107.5 (Mar. 1, 2010), p. 054102. ISSN: 0021-8979. DOI: 10.1063/1.3298454.

[18] D. a. G. Bruggeman. „Berechnung verschiedener physikalischer Konstanten von heterogenen Substanzen. I. Dielektrizitätskonstanten und Leitfähigkeiten der Mischkörper aus isotropen Substanzen." In: *Annalen der Physik* 416.7 (1935), pp. 636–664. ISSN: 1521-3889. DOI: 10.1002/andp.19354160705.

[19] Gerald Burns and F. H. Dacol. „Crystalline Ferroelectrics with Glassy Polarization Behavior." In: *Physical Review B* 28.5 (Sept. 1, 1983), pp. 2527–2530. ISSN: 0163-1829. DOI: 10.1103/PhysRevB.28.2527.

[20] R. Buzio, A. Gerbi, A. Gadaleta, L. Anghinolfi, F. Bisio, E. Bellingeri, A. S. Siri, and D. Marrè. „Modulation of Resistance Switching in Au/Nb:$SrTiO_3$ Schottky Junctions by Ambient Oxygen." In: *Applied Physics Letters* 101.24 (Dec. 10, 2012), p. 243505. ISSN: 0003-6951, 1077-3118. DOI: 10.1063/1.4771603.

[21] Cambridge Philosophical Society and Niels Bohr, eds. *Proceedings of the Cambridge Philosophical Society.* Cambridge: Cambridge Philosophical Society, 1843.

[22] A. Cavalleri, T. Dekorsy, H. H. W. Chong, J. C. Kieffer, and R. W. Schoenlein. „Evidence for a Structurally-Driven Insulator-to-Metal Transition in VO_2: A View from the Ultrafast Timescale." In: *Physical Review B* 70.16 (Oct. 2004), p. 161102. ISSN: 2469-9950. DOI: 10.1103/PhysRevB.70.161102.

[23] P. Chandra and P. B. Littlewood. *A Landau Primer for Ferroelectrics*. Sept. 14, 2006. arXiv: cond-mat/0609347. URL: http://arxiv.org/abs/cond-mat/0609347 (visited on 10/04/2020).

[24] André Chanthbouala et al. „A Ferroelectric Memristor.“ In: *Nature Materials* 11.10 (Oct. 2012), pp. 860–864. ISSN: 1476-1122, 1476-4660. DOI: 10.1038/nmat3415.

[25] A. K. Cheetham and C. N. R. Rao. „A Neutron Diffraction Study of Niobium Dioxide.“ In: *Acta Crystallographica Section B: Structural Crystallography and Crystal Chemistry* 32.5 (5 May 15, 1976), pp. 1579–1580. ISSN: 0567-7408. DOI: 10.1107/S0567740876005876.

[26] Minseok Choi, Fumiyasu Oba, and Isao Tanaka. „Role of Ti Antisitelike Defects in SrTiO 3.“ In: *Physical Review Letters* 103.18 (Oct. 30, 2009), p. 185502. ISSN: 0031-9007, 1079-7114. DOI: 10.1103/PhysRevLett.103.185502.

[27] Miri Choi, Agham Posadas, Rytis Dargis, Chih-Kang Shih, Alexander A. Demkov, Dina H. Triyoso, N. David Theodore, Catherine Dubourdieu, John Bruley, and Jean Jordan-Sweet. „Strain Relaxation in Single Crystal SrTiO $_3$ Grown on Si (001) by Molecular Beam Epitaxy.“ In: *Journal of Applied Physics* 111.6 (Mar. 15, 2012), p. 064112. ISSN: 0021-8979, 1089-7550. DOI: 10.1063/1.3695998.

[28] Dennis V. Christensen, Merlin von Soosten, Felix Trier, Thomas S. Jespersen, Anders Smith, Yunzhong Chen, and Nini Pryds. „Controlling the Carrier Density of SrTiO3-Based Heterostructures with Annealing.“ In: *Advanced Electronic Materials* 3.8 (2017), p. 1700026. ISSN: 2199-160X. DOI: 10.1002/aelm.201700026.

[29] *Combustion Synthesis Process for the Rapid Preparation of High-Purity SrO Powders*. DOI: 10.2478/s13536-014-0250-9. URL: https://sciendo.com/article/10.2478/s13536-014-0250-9 (visited on 03/16/2021).

[30] R. A. Cowley. „Lattice Dynamics and Phase Transitions of Strontium Titanate.“ In: *Physical Review* 134 (4A May 18, 1964), A981–A997. ISSN: 0031-899X. DOI: 10.1103/PhysRev.134.A981.

[31] *CRYSTAL GmbH*. https://crystal-gmbh.com/de/products/substrates/oxides.php. URL: https://crystal-gmbh.com/de/products/substrates/oxides.php (visited on 10/06/2020).

[32] *CrysTec GmbH*. http://www.crystec.de/srtio3-d.html. URL: http://www.crystec.de/srtio3-d.html (visited on 10/06/2020).

[33] F. A. Cuellar, G. Sanchez-Santolino, M. Varela, M. Clement, E. Iborra, Z. Sefrioui, J. Santamaria, and C. Leon. „Thermally Assisted Tunneling Transport in La 0.7 Ca 0.3 MnO 3 /SrTiO 3 :Nb Schottky-like Heterojunctions.“ In: *Physical Review B* 85.24 (June 20, 2012), p. 245122. ISSN: 1098-0121, 1550-235X. DOI: 10.1103/PhysRevB.85.245122.

[34] Hywel O Davies, Jonathon J Brooks, Anthony C Jones, Timothy J Leedham, Jamie F Bickley, Alexander Steiner, Paul O'Brien, Andrew J. P White, and David J Williams. „Synthesis and Crystal Structures of Three New Strontium β-Diketonate Complexes: [Sr(Tmhd)2(iPrOH)4], [Sr2(Tmhd)4(dmaeH)2(M2-dmaeH)2] and [Sr4(Tmod)8].“ In: *Polyhedron* 20.18 (Aug. 15, 2001), pp. 2397–2403. ISSN: 0277-5387. DOI: 10.1016/S0277-5387(01)00830-0.

[35] G. Dearnaley, D.V. Morgan, and A.M. Stoneham. „A Model for Filament Growth and Switching in Amorphous Oxide Films.“ In: *Journal of Non-Crystalline Solids* 4 (Apr. 1970), pp. 593–612. ISSN: 00223093. DOI: 10.1016/0022-3093(70)90097-9.

[36] Maarten de Jong et al. „Charting the Complete Elastic Properties of Inorganic Crystalline Compounds." In: *Scientific Data* 2.1 (1 Mar. 17, 2015), p. 150009. ISSN: 2052-4463. DOI: 10.1038/sdata.2015.9.

[37] *Deutschlands Größtes Beschleunigerzentrum - Deutsches Elektronen-Synchrotron DESY*. URL: https://www.desy.de/ (visited on 03/21/2021).

[38] A.F. Devonshire. „XCVI. Theory of Barium Titanate: Part I." In: *The London, Edinburgh, and Dublin Philosophical Magazine and Journal of Science* 40.309 (Oct. 1949), pp. 1040–1063. ISSN: 1941-5982, 1941-5990. DOI: 10.1080/14786444908561372.

[39] A.F. Devonshire. „Theory of Ferroelectrics." In: *Advances in Physics* 3.10 (Apr. 1954), pp. 85–130. ISSN: 0001-8732, 1460-6976. DOI: 10.1080/00018735400101173.

[40] J. F. Dewald, A. D. Pearson, W. R. Northover, and W. F. Peck Jr. „Semi-Conducting Glasses." In: *Electrochem. Soc* 109 (1962), p. 243c.

[41] Robert Dittmer. „Lead-Free Piezoceramics ? Ergodic and Nonergodic Relaxor Ferroelectrics Based on Bismuth Sodium Titanate." Darmstadt: Technische Universität, 2013.

[42] Hongchu Du, Chun-Lin Jia, Annemarie Koehl, Juri Barthel, Regina Dittmann, Rainer Waser, and Joachim Mayer. „Nanosized Conducting Filaments Formed by Atomic-Scale Defects in Redox-Based Resistive Switching Memories." In: *Chemistry of Materials* 29.7 (Apr. 11, 2017), pp. 3164–3173. ISSN: 0897-4756, 1520-5002. DOI: 10.1021/acs.chemmater.7b00220.

[43] Saul Dushman. „Electron Emission from Metals as a Function of Temperature." In: *Physical Review* 21.6 (June 1, 1923), pp. 623–636. ISSN: 0031-899X. DOI: 10.1103/PhysRev.21.623.

[44] Robert Eason, ed. *Pulsed Laser Deposition of Thin Films: Applications-Led Growth of Functional Materials*. Hoboken, NJ, USA: John Wiley & Sons, Inc., Nov. 17, 2006. ISBN: 978-0-470-05212-9 978-0-471-44709-2. DOI: 10.1002/0470052120; http://web.archive.org/web/20200910182715/https://onlinelibrary.wiley.com/doi/book/10.1002/0470052120.

[45] Iguchi Eisuke and Yajima Kazuo. „Diffusion of Oxygen Vacancies in Reduced Rutile (TiO_2)." In: *Journal of the Physical Society of Japan* (Dec. 12, 2013). DOI: 10.1143/JPSJ.32.1415.

[46] Johannes van Ek, Dieter Weller, and Martin L. Plumer. *The Physics of Ultra-High-Density Magnetic Recording*. 2001. ISBN: 978-3-642-56657-8.

[47] R. John Errington, John Ridland, William Clegg, Robert A. Coxall, and Jan M. Sherwood. „β-Diketonate Derivatives of Titanium Alkoxides: X-Ray Crystal Structures and Solution Dynamics of the Binuclear Complexes [{Ti(OR)3(Dik)}2]." In: *Polyhedron* 17.5 (Mar. 30, 1998), pp. 659–674. ISSN: 0277-5387. DOI: 10.1016/S0277-5387(97)00418-X.

[48] Kam Eshghi, Alessia Marelli, and Rino Micheloni, eds. *Inside Solid State Drives (SSDs)*. 2nd ed. 2018. Springer Series in Advanced Microelectronics 37. Singapore: Springer Singapore : Imprint: Springer, 2018. 1 p. ISBN: 9789811305993. DOI: 10.1007/978-981-13-0599-3.

[49] V. Eyert. „The Metal-Insulator Transition of NbO_2: An Embedded Peierls Instability.“ In: *EPL (Europhysics Letters)* 58.6 (June 2002), p. 851. ISSN: 0295-5075. DOI: 10.1209/epl/i2002-00452-6.

[50] Ali Fakih, Johan Biscaras, and Abhay Shukla. *Growth and Characterization of Polycrystalline NbO_2 Thin Films on Crystalline and Amorphous Substrates*. Oct. 7, 2019. arXiv: 1910.02824 [cond-mat]. URL: http://arxiv.org/abs/1910.02824 (visited on 09/09/2020).

[51] W. A. Feil and B. W. Wessels. „Defect Structure of Strontium Titanate Thin Films.“ In: *Journal of Applied Physics* 74.6 (Sept. 15, 1993), pp. 3927–3931. ISSN: 0021-8979. DOI: 10.1063/1.354492.

[52] Ralph Howard Fowler and L. Nordheim. „Electron Emission in Intense Electric Fields.“ In: *Proceedings of the Royal Society of London. Series A, Containing Papers of a Mathematical and Physical Character* 119.781 (May 1, 1928), pp. 173–181. DOI: 10.1098/rspa.1928.0091.

[53] D. Fuchs, C. W. Schneider, R. Schneider, and H. Rietschel. „High Dielectric Constant and Tunability of Epitaxial SrTiO3 Thin Film Capacitors.“ In: *Journal of Applied Physics* 85.10 (May 5, 1999), pp. 7362–7369. ISSN: 0021-8979. DOI: 10.1063/1.369363.

[54] Carsten Funck, Astrid Marchewka, Christoph Bäumer, Peter C. Schmidt, Phillip Müller, Regina Dittmann, Manfred Martin, Rainer Waser, and Stephan Menzel. „A Theoretical and Experimental View on the Temperature Dependence of the Electronic Conduction through a Schottky Barrier in a Resistively Switching SrTiO3-Based Memory Cell.“ In: *Advanced Electronic Materials* 4.7 (2018), p. 1800062. ISSN: 2199-160X. DOI: 10.1002/aelm.201800062.

[55] Carsten Funck, Stephan Menzel, Nabeel Aslam, Hehe Zhang, Alexander Hardtdegen, Rainer Waser, and Susanne Hoffmann-Eifert. „Multidimensional Simulation of Threshold Switching in NbO_2 Based on an Electric Field Triggered Thermal Runaway Model.“ In: *Advanced Electronic Materials* 2.7 (2016), p. 1600169. ISSN: 2199-160X. DOI: 10.1002/aelm.201600169.

[56] Yanfeng Gao, Yoshitake Masuda, Tetsu Yonezawa, and Kunihito Koumoto. „Site-Selective Deposition and Micropatterning of $SrTiO_3$ Thin Film on Self-Assembled Monolayers by the Liquid Phase Deposition Method.“ In: *Chemistry of Materials* 14.12 (Dec. 2002), pp. 5006–5014. ISSN: 0897-4756, 1520-5002. DOI: 10.1021/cm020358p.

[57] V. Garcia, S. Fusil, K. Bouzehouane, S. Enouz-Vedrenne, N. D. Mathur, A. Barthélémy, and M. Bibes. „Giant Tunnel Electroresistance for Non-Destructive Readout of Ferroelectric States.“ In: *Nature* 460.7251 (7251 July 2009), pp. 81–84. ISSN: 1476-4687. DOI: 10.1038/nature08128.

[58] Vincent Garcia and Manuel Bibes. „Ferroelectric Tunnel Junctions for Information Storage and Processing.“ In: *Nature Communications* 5.1 (1 July 24, 2014), pp. 1–12. ISSN: 2041-1723. DOI: 10.1038/ncomms5289.

[59] V. L. Ginzburg and L. D. Landau. „On the Theory of Superconductivity.“ In: *On Superconductivity and Superfluidity: A Scientific Autobiography*. Ed. by Vitaly L. Ginzburg. Berlin, Heidelberg: Springer, 2009, pp. 113–137. ISBN: 978-3-540-68008-6. DOI: 10.1007/978-3-540-68008-6_4.

[60] *Grafox - Oxides for Electronics Research*. URL: http://grafox.pdi-berlin.de/ (visited on 03/15/2021).

[61] Christo Guguschev, Zbigniew Galazka, Dirk J. Kok, Uta Juda, Albert Kwasniewski, and Reinhard Uecker. „Growth of $SrTiO_3$ Bulk Single Crystals Using Edge-Defined Film-Fed Growth and the Czochralski Methods.“ In: *CrystEngComm* 17.25 (2015), pp. 4662–4668. ISSN: 1466-8033. DOI: 10.1039/C5CE00798D.

[62] Christo Guguschev, Dirk J. Kok, Zbigniew Galazka, Detlef Klimm, Reinhard Uecker, Rainer Bertram, Martin Naumann, Uta Juda, Albert Kwasniewski, and Matthias Bickermann. „Influence of Oxygen Partial Pressure on $SrTiO_3$ Bulk Crystal Growth from Non-Stoichiometric Melts.“ In: *Crystengcomm* 17.17 (2015), pp. 3224–3234. ISSN: 1466-8033. DOI: 10.1039/c5ce00095e.

[63] J. H. Haeni et al. „Room-Temperature Ferroelectricity in Strained SrTiO3.“ In: *Nature* 430.7001 (Aug. 12, 2004), pp. 758–761. ISSN: 0028-0836. DOI: 10.1038/nature02773.

[64] Gene H. Haertling. „Ferroelectric Ceramics: History and Technology.“ In: *Journal of the American Ceramic Society* 82.4 (1999), pp. 797–818. ISSN: 1551-2916. DOI: 10.1111/j.1151-2916.1999.tb01840.x.

[65] F.V.E. Hensling, T. Heisig, N. Raab, C. Baeumer, and R. Dittmann. „Tailoring the Switching Performance of Resistive Switching SrTiO3 Devices by SrO Interface Engineering.“ In: *Solid State Ionics* 325 (Nov. 2018), pp. 247–250. ISSN: 01672738. DOI: 10.1016/j.ssi.2018.09.003.

[66] Felix V. E. Hensling, Hongchu Du, Nicolas Raab, Chun-Lin Jia, Joachim Mayer, and Regina Dittmann. „Engineering Antiphase Boundaries in Epitaxial SrTiO3 to Achieve Forming Free Memristive Devices.“ In: *APL Materials* 7.10 (Oct. 1, 2019), p. 101127. DOI: 10.1063/1.5125211.

[67] Takashi Hirano, Masahiro Taga, and Takeshi Kobayashi. „Effect of Nonstoichiometry on Dielectric Properties of Strontium Titanate Thin Films Grown by ArF Excimer Laser Ablation.“ In: *Japanese Journal of Applied Physics* 32 (12A Dec. 1993), p. L1760. ISSN: 1347-4065. DOI: 10.1143/JJAP.32.L1760.

[68] Masahiko Hiratani, Yoshinobu Tarutani, Tokuumi Fukazawa, Masakuni Okamoto, and Kazumasa Takagi. „Growth of SrTiO3 Thin Films by Pulsed-Laser Deposition.“ In: *Thin Solid Films* 227.1 (May 5, 1993), pp. 100–104. ISSN: 0040-6090. DOI: 10.1016/0040-6090(93)90192-R.

[69] M. J Hordon and B. L Averbach. „X-Ray Measurements of Dislocation Density in Deformed Copper and Aluminum Single Crystals.“ In: *Acta Metallurgica* 9.3 (Mar. 1, 1961), pp. 237–246. ISSN: 0001-6160. DOI: 10.1016/0001-6160(61)90073-6.

[70] H. J. Hovel and J. J. Urgell. „Switching and Memory Characteristics of ZnSe - Ge Heterojunctions.“ In: *Journal of Applied Physics* 42.12 (Nov. 1, 1971), pp. 5076–5083. ISSN: 0021-8979. DOI: 10.1063/1.1659895.

[71] Yi-Jen Huang, Shih-Chun Chao, Der-Hsien Lien, Cheng-Yen Wen, Jr-Hau He, and Si-Chen Lee. „Dual-Functional Memory and Threshold Resistive Switching Based on the Push-Pull Mechanism of Oxygen Ions." In: *Scientific Reports* 6.1 (1 Apr. 7, 2016), p. 23945. ISSN: 2045-2322. DOI: 10.1038/srep23945.

[72] M. Itoh, R. Wang, Y. Inaguma, T. Yamaguchi, Y-J. Shan, and T. Nakamura. „Ferroelectricity Induced by Oxygen Isotope Exchange in Strontium Titanate Perovskite." In: *Physical Review Letters* 82.17 (Apr. 26, 1999), pp. 3540–3543. ISSN: 0031-9007, 1079-7114. DOI: 10.1103/PhysRevLett.82.3540.

[73] H. W. Jang et al. „Ferroelectricity in Strain-Free $SrTiO_3$ Thin Films." In: *Physical Review Letters* 104.19 (May 13, 2010), p. 197601. ISSN: 0031-9007, 1079-7114. DOI: 10.1103/PhysRevLett.104.197601.

[74] R. F. Janninck and D. H. Whitmore. „Electrical Conduction in Nonstoichiometric A-Nb_2O_5." In: *The Journal of Chemical Physics* 37.12 (Dec. 15, 1962), pp. 2750–2754. ISSN: 0021-9606. DOI: 10.1063/1.1733100.

[75] R.F. Janninck and D.H. Whitmore. „Electrical Conductivity and Thermoelectric Power of Niobium Dioxide." In: *Journal of Physics and Chemistry of Solids* 27.6-7 (June 1966), pp. 1183–1187. ISSN: 00223697. DOI: 10.1016/0022-3697(66)90094-1.

[76] Anderson Janotti, Joel B. Varley, Minseok Choi, and Chris G. Van de Walle. „Vacancies and Small Polarons in SrTiO 3." In: *Physical Review B* 90.8 (Aug. 18, 2014). ISSN: 1098-0121, 1550-235X. DOI: 10.1103/PhysRevB.90.085202.

[77] Peter Uhd Jepsen, Bernd M. Fischer, Andreas Thoman, Hanspeter Helm, J. Y. Suh, Rene Lopez, and R. F. Haglund. „Metal-Insulator Phase Transition in a VO_2 Thin Film Observed with Terahertz Spectroscopy." In: *Physical Review B* 74.20 (Nov. 2006), p. 205103. ISSN: 2469-9950. DOI: 10.1103/PhysRevB.74.205103.

[78] X. L. Jiang, Y. G. Zhao, X. Zhang, M. H. Zhu, H. Y. Zhang, D. S. Shang, and J. R. Sun. „Trap State Controlled Bipolar Resistive Switching Effect and Electronic Transport in LaAlO $_3$ /Nb:SrTiO $_3$ Heterostructures." In: *Applied Physics Letters* 102.23 (June 10, 2013), p. 233501. ISSN: 0003-6951, 1077-3118. DOI: 10.1063/1.4809948.

[79] Toyanath Joshi, Tess R. Senty, Pavel Borisov, Alan D. Bristow, and David Lederman. „Preparation, Characterization, and Electrical Properties of Epitaxial NbO_2 Thin Film Lateral Devices." In: *Journal of Physics D: Applied Physics* 48.33 (July 2015), p. 335308. ISSN: 0022-3727. DOI: 10.1088/0022-3727/48/33/335308.

[80] Antti Karjalainen, Vera Prozheeva, Ilja Makkonen, Christo Guguschev, Toni Markurt, Matthias Bickermann, and Filip Tuomisto. „TiSr Antisite: An Abundant Point Defect in SrTiO3." In: *Journal of Applied Physics* 127.24 (June 22, 2020), p. 245702. ISSN: 0021-8979. DOI: 10.1063/5.0010304.

[81] Heungsoo Kim, Kwok Cheung, Raymond C. Y. Auyeung, Donald E. Wilson, Kristin M. Charipar, Alberto Piqué, and Nicholas A. Charipar. „VO_2-Based Switchable Radiator for Spacecraft Thermal Control." In: *Scientific Reports* 9.1 (1 Aug. 5, 2019), p. 11329. ISSN: 2045-2322. DOI: 10.1038/s41598-019-47572-z.

[82] Seonghyun Kim, Jubong Park, Jiyong Woo, Chunhum Cho, Wootae Lee, Jungho Shin, Godeuni Choi, Sangsu Park, Daeseok Lee, Byoung Hun Lee, and Hyunsang Hwang. „Threshold-Switching Characteristics of a Nanothin-NbO_2-Layer-Based Pt/NbO_2/Pt Stack for Use in Cross-Point-Type Resistive Memories." In: *Microelectronic Engineering* 107 (July 1, 2013), pp. 33–36. ISSN: 0167-9317. DOI: 10.1016/j.mee.2013.02.084.

[83] Wan Gee Kim et al. „NbO_2-Based Low Power and Cost Effective 1S1R Switching for High Density Cross Point ReRAM Application." In: *2014 Symposium on VLSI Technology (VLSI-Technology): Digest of Technical Papers*. June 2014, pp. 1–2. DOI: 10.1109/VLSIT.2014.6894405.

[84] Charles Kittel. *Introduction to Solid State Physics*. 8th ed. Hoboken, NJ: Wiley, 2005. 680 pp. ISBN: 978-0-471-41526-8.

[85] Konstantin Klyukin and Vitaly Alexandrov. „Effect of Intrinsic Point Defects on Ferroelectric Polarization Behavior of $SrTiO_3$." In: *Physical Review B* 95.3 (Jan. 4, 2017), p. 035301. DOI: 10.1103/PhysRevB.95.035301.

[86] Konstantin Klyukin, L. L. Tao, Evgeny Y. Tsymbal, and Vitaly Alexandrov. „Defect-Assisted Tunneling Electroresistance in Ferroelectric Tunnel Junctions." In: *Physical Review Letters* 121.5 (Aug. 3, 2018), p. 056601. DOI: 10.1103/PhysRevLett.121.056601.

[87] Shunsuke Kobayashi, Yuki Mizumukai, Tsuyoshi Ohnishi, Naoya Shibata, Yuichi Ikuhara, and Takahisa Yamamoto. „High Electron Mobility of Nb-Doped $SrTiO_3$ Films Stemming from Rod-Type Sr Vacancy Clusters." In: *ACS Nano* 9.11 (Nov. 24, 2015), pp. 10769–10777. ISSN: 1936-0851, 1936-086X. DOI: 10.1021/acsnano.5b05720.

[88] Dirk J. Kok, Klaus Irmscher, Martin Naumann, Christo Guguschev, Zbigniew Galazka, and Reinhard Uecker. „Temperature-Dependent Optical Absorption of $SrTiO_3$." In: *physica status solidi (a)* 212.9 (Sept. 2015), pp. 1880–1887. ISSN: 18626300. DOI: 10.1002/pssa.201431836.

[89] Yu G. Kriger, N. F. Yudanov, I. K. Igumenov, and S. B. Vashchenko. „Study of Test Structures of a Molecular Memory Element." In: *Journal of Structural Chemistry* 34.6 (1993), pp. 966–970.

[90] A. D. Kurtz, S. A. Kulin, and B. L. Averbach. „Effect of Dislocations on the Minority Carrier Lifetime in Semiconductors." In: *Physical Review* 101.4 (Feb. 15, 1956), pp. 1285–1291. DOI: 10.1103/PhysRev.101.1285.

[91] S. K. Kurtz. In: *Trans. Am. Crystallogr. Assoc.* 2.63 (1975).

[92] Deok-Hwang Kwon et al. „Unraveling the Origin and Mechanism of Nanofilament Formation in Polycrystalline SrTiO3 Resistive Switching Memories." In: *Advanced Materials* 31.28 (2019), p. 1901322. ISSN: 1521-4095. DOI: 10.1002/adma.201901322.

[93] Miguel Angel Lastras-Montano, Amirali Ghofrani, and Kwang-Ting Cheng. „A Low-Power Hybrid Reconfigurable Architecture for Resistive Random-Access Memories." In: *2016 IEEE International Symposium on High Performance Computer Architecture (HPCA)*. 2016 IEEE International Symposium on High Performance Computer Architecture (HPCA). Barcelona, Spain: IEEE, Mar. 2016, pp. 102–113. ISBN: 978-1-4673-9211-2. DOI: 10.1109/HPCA.2016.7446057.

[94] R. B. Laughlin. „Introduction to the Physics of Energy.“ Stanford University, Aut. 2018.

[95] Che-Hui Lee et al. „Effect of Stoichiometry on the Dielectric Properties and Soft Mode Behavior of Strained Epitaxial SrTiO3 Thin Films on DyScO3 Substrates.“ In: *Applied Physics Letters* 102.8 (Feb. 25, 2013), p. 082905. ISSN: 0003-6951. DOI: 10.1063/1.4793649.

[96] D. Lee et al. „Emergence of Room-Temperature Ferroelectricity at Reduced Dimensions.“ In: *Science* 349.6254 (Sept. 18, 2015), pp. 1314–1317. ISSN: 0036-8075, 1095-9203. DOI: 10.1126/science.aaa6442. pmid: 26383947.

[97] J. C. Lee and W. W. Durand. „Electrically Stimulated Optical Switching of NbO ₂ Thin Films.“ In: *Journal of Applied Physics* 56.11 (Dec. 1984), pp. 3350–3352. ISSN: 0021-8979, 1089-7550. DOI: 10.1063/1.333863.

[98] J. C. Lee and W. W. Durand. „Electrically Stimulated Optical Switching of NbO_2 Thin Films.“ In: *Journal of Applied Physics* 56.11 (Dec. 1, 1984), pp. 3350–3352. ISSN: 0021-8979. DOI: 10.1063/1.333863.

[99] Jian Yong Li, Takeshi Ohgaki, Ryota Matsuoka, Hideyo Okushi, and Naoki Ohashi. „Electrical Properties of Pt/Nb-Doped $SrTiO_3$ Schottky Junctions.“ In: *Key Engineering Materials* 421-422 (Dec. 2009), pp. 463–466. ISSN: 1662-9795. DOI: 10.4028/www.scientific.net/KEM.421-422.463.

[100] M. Lippmaa, N. Nakagawa, M. Kawasaki, S. Ohashi, Y. Inaguma, M. Itoh, and H. Koinuma. „Step-Flow Growth of SrTiO3 Thin Films with a Dielectric Constant Exceeding 104.“ In: *Applied Physics Letters* 74.23 (May 26, 1999), pp. 3543–3545. ISSN: 0003-6951. DOI: 10.1063/1.124155.

[101] Haidong Lu et al. „Tunneling Hot Spots in Ferroelectric SrTiO ₃.“ In: *Nano Letters* 18.1 (Jan. 10, 2018), pp. 491–497. ISSN: 1530-6984, 1530-6992. DOI: 10.1021/acs.nanolett.7b04444.

[102] Farrel W. Lytle. „X-Ray Diffractometry of Low-Temperature Phase Transformations in Strontium Titanate.“ In: *Journal of Applied Physics* 35.7 (July 1964), pp. 2212–2215. ISSN: 0021-8979, 1089-7550. DOI: 10.1063/1.1702820.

[103] Peter Mark and Wolfgang Helfrich. „Space-Charge-Limited Currents in Organic Crystals.“ In: (), p. 12.

[104] Stephan Menzel, Matthias Waters, Astrid Marchewka, Ulrich Böttger, Regina Dittmann, and Rainer Waser. „Origin of the Ultra-Nonlinear Switching Kinetics in Oxide-Based Resistive Switches.“ In: *Advanced Functional Materials* 21.23 (2011), pp. 4487–4492. ISSN: 1616-3028. DOI: 10.1002/adfm.201101117.

[105] Walter J. Merz. „The Electric and Optical Behavior of BaTi${\mathrm{O}}_{3}$ Single-Domain Crystals.“ In: *Physical Review* 76.8 (Oct. 15, 1949), pp. 1221–1225. DOI: 10.1103/PhysRev.76.1221.

[106] Herbert B. Michaelson. „The Work Function of the Elements and Its Periodicity.“ In: *Journal of Applied Physics* 48.11 (Nov. 1, 1977), pp. 4729–4733. ISSN: 0021-8979. DOI: 10.1063/1.323539.

[107] Evgeny Mikheev, Brian D. Hoskins, Dmitri B. Strukov, and Susanne Stemmer. „Resistive Switching and Its Suppression in Pt/Nb:SrTiO3 Junctions." In: *Nature Communications* 5 (June 2, 2014). ISSN: 2041-1723. DOI: 10.1038/ncomms4990. pmid: 24886761.

[108] T. Mikolajick, C. Dehm, W. Hartner, I. Kasko, M.J. Kastner, N. Nagel, M. Moert, and C. Mazure. „FeRAM Technology for High Density Applications." In: *Microelectronics Reliability* 41.7 (July 2001), pp. 947–950. ISSN: 00262714. DOI: 10.1016/S0026-2714(01)00049-X.

[109] Shahin A. Mojarad, Kelvin S. K. Kwa, Jonathan P. Goss, Zhiyong Zhou, Nikhil K. Ponon, Daniel J. R. Appleby, Raied A. S. Al-Hamadany, and Anthony O'Neill. „A Comprehensive Study on the Leakage Current Mechanisms of Pt/SrTiO3/Pt Capacitor." In: *Journal of Applied Physics* 111.1 (Jan. 1, 2012), p. 014503. ISSN: 0021-8979. DOI: 10.1063/1.3673574.

[110] K. Momma and F. Izumi. „VESTA 3 for Three-Dimensional Visualization of Crystal, Volumetric and Morphology Data." In: *Journal of Applied Crystallography* 44.6 (6 Dec. 1, 2011), pp. 1272–1276. ISSN: 0021-8898. DOI: 10.1107/S0021889811038970.

[111] R. Moos, W. Menesklou, and K. H. Härdtl. „Hall Mobility of Undoped N-Type Conducting Strontium Titanate Single Crystals between 19 K and 1373 K." In: *Applied Physics A: Materials Science & Processing* 61.4 (1995), pp. 389–395.

[112] N. F. MOTT. „Metal-Insulator Transition." In: *Reviews of Modern Physics* 40.4 (Oct. 1, 1968), pp. 677–683. DOI: 10.1103/RevModPhys.40.677.

[113] Hans Mueller. „Properties of Rochelle Salt. III." In: *Physical Review* 58.6 (Sept. 15, 1940), pp. 565–573. ISSN: 0031-899X. DOI: 10.1103/PhysRev.58.565.

[114] K. A. Müller and H. Burkard. „$SrTiO_3$: An Intrinsic Quantum Paraelectric below 4 K." In: *Physical Review B* 19.7 (Apr. 1, 1979), pp. 3593–3602. DOI: 10.1103/PhysRevB.19.3593.

[115] Y. Muraoka and Z. Hiroi. „Metal-Insulator Transition of VO_2 Thin Films Grown on TiO_2 (001) and (110) Substrates." In: *Applied Physics Letters* 80.4 (Jan. 28, 2002), pp. 583–585. ISSN: 0003-6951. DOI: 10.1063/1.1446215.

[116] Shoichiro Nakao, Hideyuki Kamisaka, Yasushi Hirose, and Tetsuya Hasegawa. „Structural, Electrical, and Optical Properties of Polycrystalline NbO_2 Thin Films Grown on Glass Substrates by Solid Phase Crystallization." In: *physica status solidi (a)* 214.3 (2017), p. 1600604. ISSN: 1862-6319. DOI: 10.1002/pssa.201600604.

[117] Sanjoy Kumar Nandi, Xinjun Liu, Dinesh Kumar Venkatachalam, and Robert Glen Elliman. „Self-Assembly of an NbO_2 Interlayer and Configurable Resistive Switching in Pt/Nb/HfO_2/Pt Structures." In: *Applied Physics Letters* 107.13 (Sept. 28, 2015), p. 132901. ISSN: 0003-6951. DOI: 10.1063/1.4932096.

[118] Sanjoy Kumar Nandi, Xinjun Liu, Dinesh Kumar Venkatachalam, and Robert Glen Elliman. „Threshold Current Reduction for the Metal–Insulator Transition in NbO_{2-x}-Selector Devices: The Effect of ReRAM Integration." In: *Journal of Physics D: Applied Physics* 48.19 (Mar. 2015), p. 195105. ISSN: 0022-3727. DOI: 10.1088/0022-3727/48/19/195105.

[119] David Nečas and Petr Klapetek. „Gwyddion: An Open-Source Software for SPM Data Analysis." In: *Open Physics* 10.1 (2011), pp. 181–188. ISSN: 2391-5471. DOI: 10.2478/s11534-011-0096-2.

[120] R. C. Neville, B. Hoeneisen, and C. A. Mead. „Permittivity of Strontium Titanate." In: *Journal of Applied Physics* 43.5 (May 1972), pp. 2124–2131. ISSN: 0021-8979, 1089-7550. DOI: 10.1063/1.1661463.

[121] C. Nico, T. Monteiro, and M. P. F. Graça. „Niobium Oxides and Niobates Physical Properties: Review and Prospects." In: *Progress in Materials Science* 80 (July 1, 2016), pp. 1–37. ISSN: 0079-6425. DOI: 10.1016/j.pmatsci.2016.02.001.

[122] Dimin Niu, Cong Xu, Naveen Muralimanohar, Norman P. Jouppi, and Yuan Xie. „Design of Cross-Point Metal-Oxide ReRAM Emphasizing Reliability and Cost." In: *2013 IEEE/ACM International Conference on Computer-Aided Design (ICCAD)*. 2013 IEEE/ACM International Conference on Computer-Aided Design (ICCAD). San Jose, CA: IEEE, Nov. 2013, pp. 17–23. ISBN: 978-1-4799-1071-7. DOI: 10.1109/ICCAD.2013.6691092.

[123] Lindsey E. Noskin, Ariel Seidner H, and Darrell G. Schlom. „Growth of NbO_2 by Molecular-Beam Epitaxy and Characterization of Its Metal-Insulator Transition." In: *MRS Advances* 2.52 (2017/ed), pp. 3031–3036. ISSN: 2059-8521. DOI: 10.1557/adv.2017.505.

[124] Andrew O'Hara and Alexander A. Demkov. „Nature of the Metal-Insulator Transition in NbO_2." In: *Physical Review B* 91.9 (Mar. 20, 2015), p. 094305. DOI: 10.1103/PhysRevB.91.094305.

[125] Andrew O'Hara, Timothy N. Nunley, Agham B. Posadas, Stefan Zollner, and Alexander A. Demkov. „Electronic and Optical Properties of NbO_2." In: *Journal of Applied Physics* 116.21 (Dec. 3, 2014), p. 213705. ISSN: 0021-8979. DOI: 10.1063/1.4903067.

[126] K. P. O'Donnell and X. Chen. „Temperature Dependence of Semiconductor Band Gaps." In: *Applied Physics Letters* 58.25 (June 24, 1991), pp. 2924–2926. ISSN: 0003-6951, 1077-3118. DOI: 10.1063/1.104723.

[127] Naoki Ohashi, Hideki Yoshikawa, Yoshiyuki Yamashita, Shigenori Ueda, Jianyong Li, Hideyo Okushi, Keisuke Kobayashi, and Hajime Haneda. „Determination of Schottky Barrier Profile at Pt/$SrTiO_3$:Nb Junction by x-Ray Photoemission." In: *Applied Physics Letters* 101.25 (Dec. 17, 2012), p. 251911. ISSN: 0003-6951, 1077-3118. DOI: 10.1063/1.4772628.

[128] A.E. Paladino, L.G. Rubin, and J.S. Waugh. „Oxygen Ion Diffusion in Single Crystal SrTiO3." In: *Journal of Physics and Chemistry of Solids* 26.2 (Feb. 1965), pp. 391–397. ISSN: 00223697. DOI: 10.1016/0022-3697(65)90168-X.

[129] Jinho Park, Deok-Hwang Kwon, Hongwoo Park, C. U. Jung, and M. Kim. „Role of Oxygen Vacancies in Resistive Switching in Pt/Nb-Doped $SrTiO_3$." In: *Applied Physics Letters* 105.18 (Nov. 3, 2014), p. 183103. ISSN: 0003-6951, 1077-3118. DOI: 10.1063/1.4901053.

[130] R. Pässler. „Temperature Dependence of Fundamental Band Gaps in Group IV, III–V, and II–VI Materials via a Two-Oscillator Model.“ In: *Journal of Applied Physics* 89.11 (June 2001), pp. 6235–6240. ISSN: 0021-8979, 1089-7550. DOI: 10.1063/1.1369407.

[131] Rohana Perera, Akihiro Ikeda, Reiji Hattori, and Yukinori Kuroki. „Trap Assisted Leakage Current Conduction in Thin Silicon Oxynitride Films Grown by Rapid Thermal Oxidation Combined Microwave Excited Plasma Nitridation.“ In: *Microelectronic Engineering* 65.4 (May 2003), pp. 357–370. ISSN: 01679317. DOI: 10.1016/S0167-9317(02)01025-0.

[132] C. H. Perry, Jeanne H. Fertel, and T. F. McNelly. „Temperature Dependence of the Raman Spectrum of $SrTiO_3$ and $KTaO_3$.“ In: *The Journal of Chemical Physics* 47.5 (Sept. 1967), pp. 1619–1625. ISSN: 0021-9606, 1089-7690. DOI: 10.1063/1.1712142.

[133] Bach Thang Phan, Taekjib Choi, A. Romanenko, and Jaichan Lee. „Hopping and Trap Controlled Conduction in Cr-Doped SrTiO3 Thin Films.“ In: *Solid-State Electronics* 75 (Sept. 2012), pp. 43–47. ISSN: 00381101. DOI: 10.1016/j.sse.2012.05.007.

[134] Bach Thang Phan, Chulho Jung, and Taekjib Choi and Jaichan Lee. „Trap-Controlled Space-Charge-Limited Current Conduction in the Cr-Doped SrTiO3 Thin Films Deposited by Using Pulsed Laser Deposition.“ In: *Journal of the Korean Physical Society* 51.9 (Aug. 14, 2007), pp. 664–668. DOI: 10.3938/jkps.51.664.

[135] Pankaj Poddar, Tcipi Fried, and Gil Markovich. „First-Order Metal-Insulator Transition and Spin-Polarized Tunneling in Fe_3O_4 Nanocrystals.“ In: *Physical Review B* 65.17 (Apr. 16, 2002), p. 172405. DOI: 10.1103/PhysRevB.65.172405.

[136] Agham B. Posadas, Andrew O'Hara, Sylvie Rangan, Robert A. Bartynski, and Alexander A. Demkov. „Band Gap of Epitaxial In-Plane-Dimerized Single-Phase NbO_2 Films.“ In: *Applied Physics Letters* 104.9 (Mar. 3, 2014), p. 092901. ISSN: 0003-6951, 1077-3118. DOI: 10.1063/1.4867085.

[137] *Probing the Oxygen Vacancy Distribution in Resistive Switching Fe-SrTiO3 Metal-Insulator-Metal-Structures by Micro-x Ray Absorption near-Edge Structure: Journal of Applied Physics: Vol 111, No 7*. URL: https://aip.scitation.org/doi/full/10.1063/1.3699315 (visited on 03/21/2021).

[138] R. Pynn, J. D. Axe, and R. Thomas. „Structural Distortions in the Low-Temperature Phase of NbO_2.“ In: *Physical Review B* 13.7 (Apr. 1, 1976), pp. 2965–2975. DOI: 10.1103/PhysRevB.13.2965.

[139] M. M. Qazilbash, M. Brehm, Byung-Gyu Chae, P.-C. Ho, G. O. Andreev, Bong-Jun Kim, Sun Jin Yun, A. V. Balatsky, M. B. Maple, F. Keilmann, Hyun-Tak Kim, and D. N. Basov. „Mott Transition in VO_2 Revealed by Infrared Spectroscopy and Nano-Imaging.“ In: *Science* 318.5857 (Dec. 14, 2007), pp. 1750–1753. ISSN: 0036-8075. DOI: 10.1126/science.1150124.

[140] Mengdi Qian, Ignasi Fina, Florencio Sánchez, and Josep Fontcuberta. „Asymmetric Resistive Switching Dynamics in $BaTiO_3$ Tunnel Junctions.“ In: *Advanced Electronic Materials* 5.1 (Jan. 2019), p. 1800407. ISSN: 2199160X. DOI: 10.1002/aelm.201800407.

[141] Hannes Raebiger, Antonio Claudio M. Padilha, Alexandre Reily Rocha, and Gustavo M. Dalpian. „Electronic Mechanism for Resistive Switching in Metal/Insulator/Metal Nanodevices." In: *Journal of Physics D: Applied Physics* 53.29 (May 2020), p. 295302. ISSN: 0022-3727. DOI: 10.1088/1361-6463/ab7a58.

[142] Rakesh Rana, J. Michael Klopf, Jörg Grenzer, Harald Schneider, Manfred Helm, and Alexej Pashkin. „Nonthermal Nature of Photoinduced Insulator-to-Metal Transition in NbO_2." In: *Physical Review B* 99.4 (Jan. 2, 2019), p. 041102. DOI: 10.1103/PhysRevB.99.041102.

[143] K. V. K. Rao, S. V. N. Naidu, and P. L. N. Setty. „Thermal Expansion of Magnesium Fluoride." In: *Acta Crystallographica* 15.6 (June 10, 1962), pp. 528–530. ISSN: 0365-110X. DOI: 10.1107/S0365110X6200136X.

[144] S. Raoux, G. W. Burr, M. J. Breitwisch, C. T. Rettner, Y.- Chen, R. M. Shelby, M. Salinga, D. Krebs, S.- Chen, H.- Lung, and C. H. Lam. „Phase-Change Random Access Memory: A Scalable Technology." In: *IBM Journal of Research and Development* 52.4.5 (July 2008), pp. 465–479. ISSN: 0018-8646. DOI: 10.1147/rd.524.0465.

[145] K. V. Reich, M. Schecter, and B. I. Shklovskii. „Accumulation, Inversion, and Depletion Layers in SrTiO 3." In: *Physical Review B* 91.11 (Mar. 6, 2015). ISSN: 1098-0121, 1550-235X. DOI: 10.1103/PhysRevB.91.115303.

[146] David Reinsel, John Gantz, and John Rydning. „The Digitization of the World from Edge to Core." In: (2018), p. 28.

[147] J. Robertson. „Schottky Barrier Heights of Tantalum Oxide, Barium Strontium Titanate, Lead Titanate, and Strontium Bismuth Tantalate." In: *Applied Physics Letters* 74.8 (Feb. 18, 1999), pp. 1168–1170. ISSN: 0003-6951. DOI: 10.1063/1.123476.

[148] C. Rossel, G. I. Meijer, D. Brémaud, and D. Widmer. „Electrical Current Distribution across a Metal–Insulator–Metal Structure during Bistable Switching." In: *Journal of Applied Physics* 90.6 (Sept. 15, 2001), pp. 2892–2898. ISSN: 0021-8979, 1089-7550. DOI: 10.1063/1.1389522.

[149] D. Sacchetto, P. Gaillardon, M. Zervas, S. Carrara, G. De Micheli, and Y. Leblebici. „Applications of Multi-Terminal Memristive Devices: A Review." In: *IEEE Circuits and Systems Magazine* 13.2 (Secondquarter 2013), pp. 23–41. ISSN: 1558-0830. DOI: 10.1109/MCAS.2013.2256258.

[150] Yoshio Sakai, Nobuo Tsuda, and Tamio Sakata. „Electrical Properties of Semiconducting NbO_2." In: *Journal of the Physical Society of Japan* 54.4 (Apr. 15, 1985), pp. 1514–1518. ISSN: 0031-9015, 1347-4073. DOI: 10.1143/JPSJ.54.1514.

[151] Kimiko Sakata. „Note on the Phase Transition in NbO_2." In: *Journal of the Physical Society of Japan* 26.2 (Feb. 15, 1969), pp. 582–582. ISSN: 0031-9015, 1347-4073. DOI: 10.1143/JPSJ.26.582.

[152] Toshiyuki Sakuma, Shintaro Yamamichi, Shogo Matsubara, Hiromu Yamaguchi, and Yoichi Miyasaka. „Barrier Layers for Realization of High Capacitance Density in $SrTiO_3$ Thin-film Capacitor on Silicon." In: *Applied Physics Letters* 57.23 (Dec. 3, 1990), pp. 2431–2433. ISSN: 0003-6951, 1077-3118. DOI: 10.1063/1.103867.

[153] Etsuro Sawaguchi, Atsushi Kikuchi, and Yōichi Kodera. „Dielectric Constant of Strontium Titanate at Low Temperatures." In: *Journal of the Physical Society of Japan* 17.10 (Oct. 15, 1962), pp. 1666–1667. ISSN: 0031-9015, 1347-4073. DOI: 10.1143/JPSJ.17.1666.

[154] Harald Schäfer, R. Gruehn, and F. Schulte. „The Modifications of Niobium Pentoxide." In: *Angewandte Chemie International Edition in English* 5.1 (Jan. 1, 1966), pp. 40–52. ISSN: 1521-3773. DOI: 10.1002/anie.196600401.

[155] Hans J Scheel. „Historical Aspects of Crystal Growth Technology." In: *Journal of Crystal Growth* 211.1-4 (Apr. 2000), pp. 1–12. ISSN: 00220248. DOI: 10.1016/S0022-0248(99)00780-0.

[156] M. Schmidbauer, A. Kwasniewski, and J. Schwarzkopf. „High-Precision Absolute Lattice Parameter Determination of SrTiO3, DyScO3 and NdGaO3 Single Crystals." In: *Acta Crystallographica Section B: Structural Science* 68.1 (1 Feb. 1, 2012), pp. 8–14. ISSN: 0108-7681. DOI: 10.1107/S0108768111046738.

[157] Dieter K. Schröder. *Semiconductor Material and Device Characterization*. Hoboken, NJ, USA: John Wiley & Sons, Inc., Oct. 21, 2005. ISBN: 978-0-471-74909-7 978-0-471-73906-7. DOI: 10.1002/0471749095; http://web.archive.org/web/20200921191933/https://onlinelibrary.wiley.com/doi/book/10.1002/0471749095.

[158] D. B. Schwarz and H. U. Anderson. „Determination of Oxygen Chemical Diffusion Coefficients in Single Crystal $SrTiO_3$ by Capacitance Manometry." In: *Journal of The Electrochemical Society* 122.5 (May 1, 1975), p. 707. ISSN: 1945-7111. DOI: 10.1149/1.2134297.

[159] J. Schwarzkopf and R. Fornari. „Epitaxial Growth of Ferroelectric Oxide Films." In: *Progress in Crystal Growth and Characterization of Materials* 52.3 (Sept. 1, 2006), pp. 159–212. ISSN: 0960-8974. DOI: 10.1016/j.pcrysgrow.2006.06.001.

[160] Marisa Scrocco. „Electron-Energy-Loss and x-Ray Photoelectron Spectra of MgF_2." In: *Physical Review B* 33.10 (May 15, 1986), pp. 7228–7231. DOI: 10.1103/PhysRevB.33.7228.

[161] Katsuo Seta and Keiji Naito. „Calorimetric Study of the Phase Transition in NbO_2." In: *The Journal of Chemical Thermodynamics* 14.10 (Oct. 1, 1982), pp. 921–935. ISSN: 0021-9614. DOI: 10.1016/0021-9614(82)90002-7.

[162] Arman Shehabi, Sarah Smith, Dale Sartor, Richard Brown, Magnus Herrlin, Jonathan Koomey, Eric Masanet, Nathaniel Horner, Inês Azevedo, and William Lintner. *United States Data Center Energy Usage Report*. LBNL–1005775, 1372902. June 1, 2016, LBNL–1005775, 1372902. DOI: 10.2172/1372902.

[163] S. H. Shin, T. Halpern, and P. M. Raccah. „High-speed High-current Field Switching of NbO_2." In: *Journal of Applied Physics* 48.7 (July 1, 1977), pp. 3150–3153. ISSN: 0021-8979. DOI: 10.1063/1.324047.

[164] A A Sirenko, C Bernhard, A Golnik, Anna M Clark, Jianhua Hao, Weidong Si, and X X Xi. „Soft-Mode Hardening in $SrTiO_3$ Thin Films." In: 404.6776 (2000), p. 4.

[165] S. Slesazeck, H. Mähne, H. Wylezich, A. Wachowiak, J. Radhakrishnan, A. Ascoli, R. Tetzlaff, and T. Mikolajick. „Physical Model of Threshold Switching in NbO_2 Based Memristors." In: *RSC Adv.* 5.124 (2015), pp. 102318–102322. ISSN: 2046-2069. DOI: 10.1039/C5RA19300A.

[166] Z. Sroubek. „Electron Tunneling and Band Structure of SrTi O 3 and KTa O 3." In: *Physical Review B* 2.8 (1970), p. 3170.

[167] G. Stefanovich, A. Pergament, and D. Stefanovich. „Electrical Switching and Mott Transition in VO_2." In: *Journal of Physics: Condensed Matter* 12.41 (Sept. 2000), pp. 8837–8845. ISSN: 0953-8984. DOI: 10.1088/0953-8984/12/41/310.

[168] S. Stille, Ch. Lenser, R. Dittmann, A. Koehl, I. Krug, R. Muenstermann, J. Perlich, C. M. Schneider, U. Klemradt, and R. Waser. „Detection of Filament Formation in Forming-Free Resistive Switching $SrTiO_3$ Devices with Ti Top Electrodes." In: *Applied Physics Letters* 100.22 (May 28, 2012), p. 223503. ISSN: 0003-6951, 1077-3118. DOI: 10.1063/1.4724108.

[169] Julian Stoever, Jos E. Boschker, Saud Bin Anooz, Martin Schmidbauer, Peter Petrik, Jutta Schwarzkopf, Martin Albrecht, and Klaus Irmscher. „Approaching the High Intrinsic Electrical Resistivity of NbO_2 in Epitaxially Grown Films." In: *Applied Physics Letters* 116.18 (May 4, 2020), p. 182103. ISSN: 0003-6951. DOI: 10.1063/5.0005523.

[170] S.M. Sze. *Physics of Semiconductor Devices*. Bell Telephone Laboratories, Incorporated Murray Hill, New Jersey: WILEY-INTERSCIENCE, 1969.

[171] K. Szot, R. Dittmann, W. Speier, and R. Waser. „Nanoscale Resistive Switching in SrTiO3 Thin Films." In: *physica status solidi (RRL) – Rapid Research Letters* 1.2 (2007), R86–R88. ISSN: 1862-6270. DOI: 10.1002/pssr.200701003.

[172] Krzysztof Szot, Wolfgang Speier, Gustav Bihlmayer, and Rainer Waser. „Switching the Electrical Resistance of Individual Dislocations in Single-Crystalline SrTiO3." In: *Nature Materials* 5.4 (Apr. 2006), pp. 312–320. ISSN: 1476-1122, 1476-4660. DOI: 10.1038/nmat1614.

[173] S. Tehrani, B. Engel, J. M. Slaughter, E. Chen, M. DeHerrera, M. Durlam, P. Naji, R. Whig, J. Janesky, and J. Calder. „Recent Developments in Magnetic Tunnel Junction MRAM." In: *IEEE Transactions on Magnetics* 36.5 (Sept. 2000), pp. 2752–2757. ISSN: 1941-0069. DOI: 10.1109/20.908581.

[174] D. A. Tenne, A. K. Farrar, C. M. Brooks, T. Heeg, J. Schubert, H. W. Jang, C. W. Bark, C. M. Folkman, C. B. Eom, and D. G. Schlom. „Ferroelectricity in Nonstoichiometric $SrTiO_3$ Films Studied by Ultraviolet Raman Spectroscopy." In: *Applied Physics Letters* 97.14 (Oct. 4, 2010), p. 142901. ISSN: 0003-6951. DOI: 10.1063/1.3499273.

[175] D. A. Tenne, A. Soukiassian, M. H. Zhu, A. M. Clark, X. X. Xi, H. Choosuwan, Qi He, R. Guo, and A. S. Bhalla. „Raman Study of $Ba_xSr_{1-x}TiO_3$ Films: Evidence for the Existence of Polar Nanoregions." In: *Physical Review B* 67.1 (Jan. 31, 2003), p. 012302. ISSN: 0163-1829, 1095-3795. DOI: 10.1103/PhysRevB.67.012302.

[176] Kheamrutai Thamaphat, Pichet Limsuwan, and Boonlaer Ngotawornchai. „Phase Characterization of TiO2 Powder by XRD and TEM." In: *Agriculture and Natural Resources* 42.5 (5 Dec. 31, 2008), pp. 357–361. ISSN: 2452-316X.

[177] J. Thomas, G. Stephan, J. C. Lemonnier, M. Nisar, and S. Robin. „Optical Anisotropy of MgF, in Its UV Absorption Region." In: *physica status solidi (b)* 56.1 (1973), pp. 163–170. ISSN: 1521-3951. DOI: 10.1002/pssb.2220560115.

[178] A. Tkach, P.M. Vilarinho, A.M.R. Senos, and A.L. Kholkin. „Effect of Nonstoichiometry on the Microstructure and Dielectric Properties of Strontium Titanate Ceramics." In: *Journal of the European Ceramic Society* 25.12 (Jan. 2005), pp. 2769–2772. ISSN: 09552219. DOI: 10.1016/j.jeurceramsoc.2005.03.137.

[179] Y. Tokuda, S. Kobayashi, T. Ohnishi, T. Mizoguchi, N. Shibata, Y. Ikuhara, and T. Yamamoto. „Strontium Vacancy Clustering in Ti-Excess SrTiO3 Thin Film." In: *Applied Physics Letters* 99.3 (July 18, 2011), p. 033110. ISSN: 0003-6951. DOI: 10.1063/1.3616136.

[180] T Toyoda and M Yabe. „The Temperature Dependence of the Refractive Indices of $SrTiO_3$ and TiO_2." In: *Journal of Physics D: Applied Physics* 16.12 (Dec. 14, 1983), pp. L251–L255. ISSN: 0022-3727, 1361-6463. DOI: 10.1088/0022-3727/16/12/002.

[181] L. J. Van der Pauw. „A Method of Measuring Specific Resistivity and Hall Effect of Discs of Arbitrary Shapes." In: *Philips Research Reports* 13 (1958), pp. 1–9.

[182] J. B. Varley, A. Janotti, and C. G. Van de Walle. „Hydrogenated Vacancies and Hidden Hydrogen in SrTiO 3." In: *Physical Review B* 89.7 (Feb. 4, 2014). ISSN: 1098-0121, 1550-235X. DOI: 10.1103/PhysRevB.89.075202.

[183] Jeffrey S. Vetter and Sparsh Mittal. „Opportunities for Nonvolatile Memory Systems in Extreme-Scale High-Performance Computing." In: *Computing in Science & Engineering* 17.2 (Mar. 2015), pp. 73–82. ISSN: 1521-9615. DOI: 10.1109/MCSE.2015.4.

[184] G. Vidal-Valat, J.-P. Vidal, C. M. E. Zeyen, and K. Kurki-Suonio. „Neutron Diffraction Study of Magnesium Fluoride Single Crystals." In: *Acta Crystallographica Section B Structural Crystallography and Crystal Chemistry* 35.7 (July 1, 1979), pp. 1584–1590. ISSN: 0567-7408. DOI: 10.1107/S0567740879007184.

[185] D. Viehland, M. Wuttig, and L. E. Cross. „The Glassy Behavior of Relaxor Ferroelectrics." In: *Ferroelectrics* 120.1 (Aug. 1991), pp. 71–77. ISSN: 0015-0193, 1563-5112. DOI: 10.1080/00150199108216802.

[186] Dwight Viehland, S. J. Jang, L. Eric Cross, and Manfred Wuttig. „Freezing of the Polarization Fluctuations in Lead Magnesium Niobate Relaxors." In: *Journal of Applied Physics* 68.6 (Sept. 15, 1990), pp. 2916–2921. ISSN: 0021-8979, 1089-7550. DOI: 10.1063/1.346425.

[187] Matthew J. Wahila et al. „Evidence of a Second-Order Peierls-Driven Metal-Insulator Transition in Crystalline NbO_2." In: *Physical Review Materials* 3.7 (July 16, 2019), p. 074602. DOI: 10.1103/PhysRevMaterials.3.074602.

[188] J. J. Wang, F. Y. Meng, X. Q. Ma, M. X. Xu, and L. Q. Chen. „Lattice, Elastic, Polarization, and Electrostrictive Properties of BaTiO3 from First-Principles." In: *Journal of Applied Physics* 108.3 (Aug. 1, 2010), p. 034107. ISSN: 0021-8979. DOI: 10.1063/1.3462441.

[189] Tian Xi Wang and Wen Wen Chen. „Solid Phase Preparation of Submicron-Sized SrTiO3 Crystallites from SrO2 Nanoparticles and TiO2 Powders.“ In: *Materials Letters* 62.17 (June 30, 2008), pp. 2865–2867. ISSN: 0167-577X. DOI: 10.1016/j.matlet.2008.01.062.

[190] Y. H. Wang, K. H. Zhao, X. L. Shi, G. L. Xie, S. Y. Huang, and L. W. Zhang. „Investigation of the Resistance Switching in Au/SrTiO $_3$:Nb Heterojunctions.“ In: *Applied Physics Letters* 103.3 (July 15, 2013), p. 031601. ISSN: 0003-6951, 1077-3118. DOI: 10.1063/1.4813622.

[191] Yuhan Wang, Ryan B. Comes, Salinporn Kittiwatanakul, Stuart A. Wolf, and Jiwei Lu. „Epitaxial Niobium Dioxide Thin Films by Reactive-Biased Target Ion Beam Deposition.“ In: *Journal of Vacuum Science & Technology A: Vacuum, Surfaces, and Films* 33.2 (Jan. 16, 2015), p. 021516. ISSN: 0734-2101. DOI: 10.1116/1.4906143.

[192] Rainer Waser and Masakazu Aono. „Nanoionics-Based Resistive Switching Memories.“ In: *Nature Materials* 6.11 (Nov. 2007), p. 833. ISSN: 1476-4660. DOI: 10.1038/nmat2023.

[193] Rainer Waser, Regina Dittmann, Georgi Staikov, and Kristof Szot. „Redox-Based Resistive Switching Memories - Nanoionic Mechanisms, Prospects, and Challenges.“ In: *Advanced Materials* 21.25-26 (July 13, 2009), pp. 2632–2663. ISSN: 09359648. DOI: 10.1002/adma.200900375.

[194] H.E. Weaver. „Dielectric Properties of Single Crystals of SrTiO3 at Low Temperatures.“ In: *Journal of Physics and Chemistry of Solids* 11.3-4 (Oct. 1959), pp. 274–277. ISSN: 00223697. DOI: 10.1016/0022-3697(59)90226-4.

[195] Zhang Weibin, Wu Weidong, Wang Xueming, Cheng Xinlu, Yan Dawei, Shen Changle, Peng Liping, Wang Yuying, and Bai Li. „The Investigation of NbO $_2$ and Nb $_2$ O $_5$ Electronic Structure by XPS, UPS and First Principles Methods: The Investigation of NbO2 and Nb2O5 Electronic Structure.“ In: *Surface and Interface Analysis* 45.8 (Aug. 2013), pp. 1206–1210. ISSN: 01422421. DOI: 10.1002/sia.5253.

[196] Moritz von Witzleben, Karsten Fleck, Carsten Funck, Brigitte Baumkötter, Milena Zuric, Alexander Idt, Thomas Breuer, Rainer Waser, Ulrich Böttger, and Stephan Menzel. „Investigation of the Impact of High Temperatures on the Switching Kinetics of Redox-Based Resistive Switching Cells Using a High-Speed Nanoheater.“ In: *Advanced Electronic Materials* 3.12 (2017), p. 1700294. ISSN: 2199-160X. DOI: 10.1002/aelm.201700294.

[197] Franklin J. Wong, Nina Hong, and Shriram Ramanathan. „Orbital Splitting and Optical Conductivity of the Insulating State of NbO_2.“ In: *Physical Review B* 90.11 (Sept. 22, 2014), p. 115135. DOI: 10.1103/PhysRevB.90.115135.

[198] Y. Wu, C. Chiu, C. Chang, P. Yu, and H. Kuo. „Size-Dependent Strain Relaxation and Optical Characteristics of InGaN/GaN Nanorod LEDs.“ In: *IEEE Journal of Selected Topics in Quantum Electronics* 15.4 (July 2009), pp. 1226–1233. ISSN: 1558-4542. DOI: 10.1109/JSTQE.2009.2015583.

[199] Yuh-Renn Wu and Jasprit Singh. „Metal Piezoelectric Semiconductor Field Effect Transistors for Piezoelectric Strain Sensors.“ In: *Applied Physics Letters* 85.7 (Aug. 10, 2004), pp. 1223–1225. ISSN: 0003-6951. DOI: 10.1063/1.1784039.

[200] Yuh-Renn Wu, Madhusudan Singh, and Jasprit Singh. „Gate Leakage Suppression and Contact Engineering in Nitride Heterostructures." In: *Journal of Applied Physics* 94.9 (Oct. 23, 2003), pp. 5826–5831. ISSN: 0021-8979. DOI: 10.1063/1.1618926.

[201] Ruijuan Xu et al. „Strain-Induced Room-Temperature Ferroelectricity in SrTiO 3 Membranes." In: *Nature Communications* 11.1 (1 June 19, 2020), p. 3141. ISSN: 2041-1723. DOI: 10.1038/s41467-020-16912-3.

[202] Yasuhiro Yamada and Yoshihiko Kanemitsu. „Band-to-Band Photoluminescence in SrTiO 3." In: *Physical Review B* 82.12 (Sept. 17, 2010). ISSN: 1098-0121, 1550-235X. DOI: 10.1103/PhysRevB.82.121103.

[203] Shintaro Yamamichi, Toshiyuki Sakuma, Koichi Takemura, and Yoichi Miyasaka. „SrTiO3 Thin Film Preparation by Ion Beam Sputtering and Its Dielectric Properties." In: *Japanese Journal of Applied Physics* 30 (9S Sept. 1991), p. 2193. ISSN: 1347-4065. DOI: 10.1143/JJAP.30.2193.

[204] Tetsuya Yamamoto. „Effect of the Field Dependent Permittivity and Interfacial Layer on Ba1-xKxBiO3/Nb-Doped SrTiO3 Schottky Junctions." In: *Japanese Journal of Applied Physics* 36 (4A Apr. 1997), p. L390. ISSN: 1347-4065. DOI: 10.1143/JJAP.36.L390.

[205] Tetsuya Yamamoto, Seiji Suzuki, Kenichi Kawaguchi, and Kazuhiko Takahashi. „Temperature Dependence of the Ideality Factor of Ba1-xKxBiO3/Nb-Doped SrTiO3 All-Oxide-Type Schottky Junctions." In: *Japanese Journal of Applied Physics* 37 (9R Sept. 1998), p. 4737. ISSN: 1347-4065. DOI: 10.1143/JJAP.37.4737.

[206] J. R. Yeargan and H. L. Taylor. „The Poole-Frenkel Effect with Compensation Present." In: *Journal of Applied Physics* 39.12 (Nov. 1968), pp. 5600–5604. ISSN: 0021-8979, 1089-7550. DOI: 10.1063/1.1656022.

[207] Peter Y. Yu and Manuel Cardona. *Fundamentals of Semiconductors: Physics and Materials Properties*. Graduate Texts in Physics. Berlin: Springer, 2010. ISBN: 978-3-642-00710-1 978-3-642-00709-5.

[208] X. T. Zhang, Q. X. Yu, Y. P. Yao, and X. G. Li. „Ultrafast Resistive Switching in SrTiO3:Nb Single Crystal." In: *Applied Physics Letters* 97.22 (Nov. 29, 2010), p. 222117. ISSN: 0003-6951. DOI: 10.1063/1.3524216.

[209] C. Zhou and D. M. Newns. „Intrinsic Dead Layer Effect and the Performance of Ferroelectric Thin Film Capacitors." In: *Journal of Applied Physics* 82.6 (Sept. 15, 1997), pp. 3081–3088. ISSN: 0021-8979, 1089-7550. DOI: 10.1063/1.366147.

APPENDIX

A LIST OF FIGURES

Figure 2.1 Band model of a Schottky diode for a n-type semiconductor (e.g. $SrTiO_3$). Adapted from reference [170]. . . . 6

Figure 2.2 Schematic drawings of different transport mechanism which can occur in insulating thin films. . . . 7

Figure 2.3 Susceptibility χ over the frequency ω. Graphic adapted from Kittel (ref. [84] p.485). . . . 10

Figure 2.4 (a) Different polarizations in the perovskite structure. (b) A double potential well (ϕ) maintains the off-center position (x) of the central atom. (c) The central atom can be switched by an external force, e.g. an electric field. . . . 11

Figure 2.5 The symmetry of the crystal can influence the dielectric properties. Only non-centrosymmetric crystals can show an intrinsic ferroelectricity. Adapted from Haertling[64]. . . . 11

Figure 2.6 Dependency of permittivity ϵ to the temperature T in a relaxor ferroelectric. The maximum at T_M is dependent on the measurement frequency f. In the low temperature range, the PNRs are frozen, and the regions is called non-ergodic relaxor (NR). In the intermediate temperature region above T_f, the PNRs are mobile and ergodic, thus the phase is called ergodic relaxor (ER). Above the Burns temperature T_B, the dielectric phase is paraelectric (PE). Adapted from Dittmer[41]. . . . 12

Figure 2.7 Filament model for resistive switching with its three states. A forming pulse is applied to an insulating thin film. Afterwards the layer is in the LRS. With reverse biasing the device, the filament can be ruptured again and the device is in the HRS. . . . 14

Figure 2.8 Valence change model, based on accumulation (LRS) and redistribution (HRS) of V_O by an electric field. The band model shows, that the accumulation near the metal interface leads to a reduced space charge region and thus higher transmission probability of charge carriers. . . . 15

Figure 2.9 Schematic band diagram of ferroelectric tunnel junction. Adapted from Garcia et al.[58] . . . 15

Figure 3.1 Resistivity measurement of thin films in 4-probe setup. A constant current is supplied over the blue contacts and the potential drop is measured over the red contacts. In this case, the measurement is performed in Van-der-Pauw geometry. . . . 17

Figure 3.2 Schematic setup of the `Fraunhofer HT` 1100 K hall system for high temperature hall effect measurements in controlled atmosphere. The sample holder, placed within a gas chamber, is moved between three positions, the zero-field position and two positions between permanent magnet pairs with opposite polarity with a field strength of ± 0.5 T. 19
Figure 3.3 Schematic setup of the `Perkin-Elmer Lambda 1050` for optical absorption spectroscopy. 22
Figure 4.1 (a) ReRAM crossbar array without selector device. The dots represent cells s_{ij}. To probe the state of cell s_{11}, a voltage U_P is applied on WL1 and the current is probed on BL1. The state of cell s_{11} is 0 (red), but since the current can pass through the parasitic path $s_{14} - s_{34} - s_{31}$, a state of 1 (green) is measured. (b) In this device design, each cell has a NbO_2 selector layer integrated. If the probe voltage $U_P \sim U_T$ of the NbO_2 layer, the parasitic path is effectively blocked, since the voltage is dropping by $U_P/3$ ($n = 3$) and $U_P/3 < U_T$, thus the NbO_2 layer is in its insulating phase. (c) Stacked structure with selector layer (NbO_2) and resistive switching layer (Nb_2O_5) suggested by Nandi et al.[118] 25
Figure 4.2 Crystal structure of NbO_2. (a) Above 1080 K, NbO_2 is in its metallic (tetragonal) rutile phase. (b) Below that phase transition, NbO_2 is in a distorted body-centered tetragonal phase. Since this phase deviates just slightly from the rutile structure by a shift of the Nb-atoms, it is also commonly referred as the distorted rutile phase.[138] The shift of the Nb-atoms leads a the formation of a band gap and thus the semiconducting/insulating phase. Created with [110]. . . . 26
Figure 4.4 Schematic drawing of a high vacuum PLD chamber. A laser beam is focused through an aperture on a sintered, ceramic target and ablating molecules or molecule clusters from it. A process gas can be added to the growth atmosphere. The sample, attached to a rotating sample holder, is backside heated by a resistive heater. 29
Figure 4.3 (a) The reciprocal space map around the NbO_2 (404) reflection of an as-grown sample reveals the relaxation of the layers. $q_\perp$ and $q_\parallel$ are the reciprocal lattice parameter out-of-plane and in-plane, respectively. (b) X-ray diffraction patterns around the MgF_2 (002) diffraction peak for as-grown and annealed NbO_2 samples, proving that a c-plane NbO_2 film was grown on the c-plane MgF_2 substrate. The dashed linemarks the position of the (004) diffraction peak of unstrained NbO_2. (published in reference [169]) 30
Figure 4.5 Epitaxial thin film growth with PLD of NbO_2 on MgF_2 (001) substrates. 30
Figure 4.6 Temperature profile of NbO_2 thin film deposition with and without post-growth annealing step. 30

Figure 4.7 Atomic force micrographs showing the topography of $NbO_2(001)$ on $MgF_2(001)$. (a) shows an unannealed epitaxial layer of 100 nm thickness. The surface contain grains/islands of small size. In contrast, (b) shows an increased grain size after annealing for 1 h at 880 °C. (published in ref. [169]) 32
Figure 4.8 (a) Azimuthal φ-scan of the NbO_2 (222) reflex as an measurement of the in-plane misalignment of grains. The peak of the post-growth annealed sample is sharper compared to the as-grown layer, indicating smaller misalignment between the grains. (b) The rocking curves of the as-grown and post-growth annealed sample do not show a significant difference. (published in reference [169]) 33
Figure 4.9 RHEED image of an post-growth annealed sample after cooldown for the <100> (a) and <110> (b) direction. Spotty RHEED transmission spots are visible as well as elongated surface diffraction spots. This is in agreement with an terraced 3D surface with transmission through the grains. 34
Figure 4.10 PLD-grown layers NbO_2 on MgF_2 substrates for Hall effect and resistivity measurements. 34
Figure 4.11 The mean grain size over the resistivity of post-growth annealed NbO_2 epitaxial layers. The grain size were determined from the AFM images. Samples having large grains also show an increased resistivity. (published in reference [169]) 36
Figure 4.12 NbO_2 on MgF_2 substrates for temperature-dependent resistivity measurements. 36
Figure 4.13 Arrhenius plot of the resistivity over the temperature. Three slopes were identified and linearly interpolated, the inset shows the magnified high temperature region. Using $\rho \propto \exp(E_i/k_BT)$, activation energies was calculated from the slopes. The high temperature slope were extrapolated to the room-temperature resistivity value. (published in ref. [169]) 37
Figure 4.14 The refractive and the extinction indices of post-growth annealed NbO_2 epitaxial layers. (published in ref. [169]) 40
Figure 4.15 Schematic drawing of spectroscopic ellipsometry. Polarized light is reflected at the NbO_2/MgF_2 stack, which causes a change in polarization. This is analyzed by the rotating the analyzer and detecting the light intensity. 40
Figure 4.16 Determination of the optical band gap (a) transmission spectroscopy and (b) spectroscopic ellipsometry. In case of indirect allowed optical transitions, the band gap is absorption coefficient is proportional to the square root of the photon energy. The intercept with the x-axis give the photon energy of the transition. (published in ref. [169]) 41
Figure 4.17 Using the method from figure 4.16, temperature dependent measurements of the optical band gap were performed. The fitted line (published in ref. [169]) 43

Figure 5.1 Schematic drawing of liquid delivery metal-organic vapor phase epitaxy for the deposition of $SrTiO_3$. The precursor solvent mixture is pumped via a peristaltic pump to the flash evaporator. The solution is dropped on a hot plate and evaporated. The vapor is then transferred via heated lines to the shower head reactor, where it is mixed with additional process gases. A fast spinning susceptor is used to achieve laminar gas flow in the reactor chamber. The graphic was created by Aykut Baki. 46

Figure 5.2 HRXRD patterns of (a) thin films grown under various substrate temperatures T_S from 550 °C to 750 °C on $DyScO_3$ (110), and (b) $SrTiO_3$ films grown with various precursors concentration ratios in the liquid sources $(Sr/Ti)_{liq}$ grown on $SrTiO_3$:Nb (100) in a 2θ range between 20° to 50°. (c) The same HRXRD scans from (b) with higher magnification in the vicinity of the $SrTiO_3$:Nb (200) substrate peak (the film peak position is illustrated by blue arrows) with increasing $(Sr/Ti)_{liq}$. (d) Vertical lattice parameter $d_\perp$ as a function of $(Sr/Ti)_{liq}$. (e) Reciprocal space maps of the films with $(Sr/Ti)_{liq} = 2.6$ in the vicinity of the (204) Bragg peak of bulk $SrTiO_3$. (f) In-situ HRXRD patterns at different temperature of post-annealed $SrTiO_3$ sample with $(Sr/Ti)_{liq} = 3.0$ in pure oxygen at ambient pressure up to 950 °C. (figure including description taken from Baki et al.[8]) 47

Figure 5.3 AFM image of (a) pre-deposited $SrTiO_3$:Nb substrate after etching and annealing (roughness is 0.4 nm) (b) $SrTiO_3$ thin film on $SrTiO_3$:Nb substrate with $(Sr/Ti)_{liq} = 3.2$ annealing (roughness 0.6 nm). (Measurement by Aykut Baki) 48

Figure 5.4 STEM LAADF and HAADF images of an off-stoichiometric $SrTiO_3$ layer with $(Sr/Ti)_{liq} = 3.2$ for camera lengths of (a) 130 mm (HAADF) and (b) 300 mm (LAADF). Measurements and graphics by Tobias Schulz 50

Figure 5.5 STEM high-angle annular dark-field images for precursor supply ratios $(Sr/Ti)_{liq}$ of 2.6 (a), 3.2. and 3.6 (c). (a) is a strongly off-stoichiometric film and (c) a nearly stoichiometric one. The thin film with a stoichiometric composition is more homogeneous with less diffuse scattering. Measurements and graphics by Tobias Schulz. 51

Figure 5.7 (a) Permittivity of different substrates over the temperatures compared to literature values,[120] measured in a plate capacitor setup. Only the EFG substrates reaches as high values as the reference at low temperatures. (b) The reciprocal permittivity shows a linear increase with temperature, as it is expected from equation 5.1. However, the Verneuil grown samples show a deviation to high permittivity values at room temperature. The Verneuil #1 substrate, which is used in this study, shows a Curie temperature of 28 K and a (interpolated) room-temperature permittivity of 330, which is in agreement with literature values.[120] 54

Figure 5.6 Plate capacitor structures based on $SrTiO_3$ single-crystal substrates. To get concentrically oriented contacts for a homogeneous electric field inside the substrate, a special clamping shadow mask was used. The sample is clamped in the holder. In a two step process, both sides of the substrate were deposited with 50 nm titanium and 50 nm gold. 54
Figure 5.8 (a) Room-temperature field dependence of the permittivity, measured on a PLD grown $SrTiO_3$ thin film of 1 µm thickness. The zero-field permittivity is around 260. The Landau-Devonshire model was fitted to the field-dependent permittivity. (b) Current-voltage measurement to determine leakage currents. (c) Double logarithmic plot to determine the origin of the increase current for negative bias. 57
Figure 5.10 Measurement of the permittivity of the PLD layer in a temperature range of 20 K to 534 K and a electric field strength of up to 1 MV cm^{-1} to determine $\epsilon_r(T, E)$ for transport models in resistive switching devices. 58
Figure 5.9 Ideal model of the band structure of an $SrTiO_3$ on $SrTiO_3$ metal-insulator-semiconductor structure. The built-in voltage V_{bi} comes from a different alignment of the Fermi level within the insulating and doped $SrTiO_3$ film and substrate, respectively. Due to that, a space charge region can form in the substrate. (adapted from reference [170]) 58
Figure 5.11 Temperature dependence of substrate capacitance and layer capacitance. The capacitance of the layer is weakly temperature dependent, unlike the substrate capacitance. Interface charges, if low, can lead to an underestimation of the permittivity. 60
Figure 5.12 Modeling the temperature and field-dependence with the Landau-Ginzburg model by using the permittivity data presented in figure 5.10. Barretts formula and the Curie Weiss law are then applied on the obtained coefficients χ and ξ. 61
Figure 5.13 (a) Dependency of the permittivity for MOVPE grown $SrTiO_3$ on the lattice parameter and thus the tetragonal distortion. Additionally, it correlates with the Sr/Ti precursor ratio, which is an indication of stoichiometry control in the thin films. (b) The permittivity over temperature plots for some a selection of the grown thin films. The temperature dependence is weak. Beside of that, a damping of the permittivity at low temperature is seen, which is an indication of strong polarization. 63
Figure 5.14 Schematic layout of the device structure 63
Figure 5.15 Curie-Weiss law fitted to the permittivity over temperature of MOVPE grown samples grown under different Sr/Ti precursor ratios. 64
Figure 5.16 Schematic layout of the $SrTiO_3$ resistive switching device. 67
Figure 5.18 Hysteresis current-voltage curve an off-stoichiometric $SrTiO_3$ thin film. Each branch of the curve were fitted with appropriate electrical transport models. In negative voltage region for the LRS, a parallel current of trap-assisted tunneling and Schottky emission was found. 68

Figure 5.17 Band structures of MIS devices. (a) A negative bias leads to a depletion zone at the insulator semiconductor interface. (b) A positive bias leads to an accumulation of charge carrier at the interface. . . . 68
Figure 5.19 Band structure of the $SrTiO_3$ thin film in the LRS. 69
Figure 5.20 Current-voltage characteristics of $SrTiO_3$ thin film at 10 K. Several IV curves with different voltage ranges were recorded. Sweeps #1, #2, and #3 show reproducible (overlapping) IV characteristics. No hysteresis is found. The voltage range in sweep #4 is extended, so that the sweep has Sweep #4 voltage range is extended to negative and positive range and part of the sweep is above a threshold voltage U_4. As a result, the thin film is switching between HRS and LRS. The HRS curve shows a current below the initial, non-switching sweeps, the LRS an higher current. Sweep #5 has an even extended voltage range, increasing the difference between LRS and HRS. 71
Figure 5.21 Ratio between LRS and HRS of hysteresis sweep #5 in figure 5.20. The maximum ratio between the states is 2.1×10^7 at -0.3 V and 4.1×10^5 at 0.75 V. 71
Figure 5.22 Pulsed IV measurements of $SrTiO_3$ thin film at 10 K. The U_{HRS} was set to -4 V. The U_{LRS} was varied between 1.25 V to 2 V. The readout voltage was set to $U_{ro} = -0.1$ V. The pulse length was set to 100 ms for all pulses. On the top, the voltage pulse pattern over time is shown. On the bottom, the corresponding current is shown. It is seen, that the LRS current increases with pulse U_{HRS} and no switching is observed below the threshold voltage $U_{threshold}$. 72
Figure 5.23 Measurement of the threshold voltage for resistive switching at different temperatures. The sample was pulsed with the pulse pattern shown in figure 5.22. Each horizontal line represent the average current measured at LRS after each of the three LRS pulses. The black circle represents the average of the three average LRS current values. For low temperature, the threshold voltage is at around $U_{threshold} = 1.2$ V to 1.4 V and the LRS current is exponentially increasing with U_{LRS}. At 300 K, still a threshold at around 0.7 V to 0.8 V can be measured. In contrast to the low temperature measurements, the current at lower pulse voltages is limited by the increased HRS current and to the top by saturation. 73
Figure 5.24 Linearized current - voltage relations for a) Schottky emission and b) trap-assisted tunneling. A linear slope indicates a good agreement with the corresponding model. The dashed vertical line indicates the threshold voltage U_T, for which the switching between the LRS and HRS occurs. For the HRS in the Schottky emission model, the permittivity is increasing the more the state is pronounced. . . . 74
Figure 5.25 Linearized current - voltage relations for a) Schottky emission and b) thermionic emission. A linear slope indicates a good agreement with the corresponding model. The dashed vertical line indicates the threshold voltage U_T, for which the switching between the LRS and HRS occurs. 75

Figure 5.26 Temperature dependence of the current through the $SrTiO_3$ thin film. The low-resistive state in the LRS is temperature independent, indicating a tunneling current. The HRS in the negative voltage region decreases until cooling to 200 K, and increases again by further cooling the sample to 10 K. The positive bias region is temperature dependent and thus indicating a emission current. 76
Figure 5.27 Resistive switching for three samples with differences in Sr deficiency measured at room-temperature. The Sr/Ti precursor ratios were (a) 2.7, (b) 2.9 and (c) 3.6. The ratio between low and HRS is higher for strong Sr deficiency and gets low for almost stoichiometric samples (c). The stoichiometric sample still shows a hysteresis, indicating some residual defect concentration. 77
Figure 5.28 Pulsed measurement of a Sr deficient sample (left) and an almost stoichiometric sample. The off-stoichiometric sample shows a high ratio between low and HRS of 1×10^3, the stoichiometric sample only by a factor of 2. 78
Figure 5.29 Current-voltage curves of a stoichiometric sample (Sr/Ti precursor ratio 3.6). The voltage range was gradually increased, which leads to an increased current the formation of the hysteresis 79
Figure 5.30 Decrease of conductivity of a stoichiometric $SrTiO_3$ thin film over time after performing resistive switching sweeps. 79
Figure 5.31 Schematic band diagram of the trap-assisted ferroelectric tunnel junction. $|U| < |U_T|$ is the state below the threshold voltage, $|U| < |U_T|$ the state above the threshold voltage. The polarization leads to either a accumulation or depletion at the interface between thin film and substrate. The depletion leads to an additional barrier, which is blocking the charge carriers and thus increasing the resistivity. In the low-resistive state, the current is dominated by trap-assisted tunneling, which has a small barrier height. 88
Figure 5.32 (a) Simulated band structure of the suggest trap-assisted ferroelectric tunnel junction in low and high resistive state. The Fermi level is at 0 eV. The vertical dashed line represents the interface of thin film and substrate. (b) The corresponding charge carrier concentration. The hole concentration is negligible. 90
Figure 5.33 (a) Simulated band structure at −5 V of the suggest trap-assisted ferroelectric tunnel junction in low and high resistive state. The vertical dashed line represents the interface of thin film and substrate. (b) The corresponding charge carrier concentration. The hole concentration is negligible. 91
Figure 5.34 (a) Simulated band structure at 5 V of the suggest trap-assisted ferroelectric tunnel junction in low and high resistive state. The vertical dashed line represents the interface of thin film and substrate. (b) The corresponding charge carrier concentration. The hole concentration is negligible. 92

B LIST OF TABLES

Table 4.1 Structural parameter for NbO_2 and the substrate material MgF_2. a and c are the lattice parameter in the tetragonal crystal structure, α is the thermal expansion coefficient at 300 K 29

Table 4.2 Calculated thermal strain S for NbO_2 (001) grown on MgF_2 (001) and the corresponding calculated and measured reciprocal vertical lattice parameter $q_\perp$ 31

Table 4.3 Influence of the growth parameter temperature T, pressure p and laser pulse energy P on the growth of as-grown and annealed samples. All growth processes started with the nucleation at $T = 350\,°C$ with a continuous temperature ramp to the final growth temperature T to prevent substrate degradation. All layers were around 100 nm thick by using 18 000 pulses. 35

Table 5.1 Growth parameter for the $SrTiO_3$ MOVPE process. 46

Table 5.2 Three different types of substrates were compared, two commercial Verneuil grown substrates and an in-house grown EFG substrate. All substrates have comparable thickness t. Both Verneuil substrates show a too low permittivity ϵ_r compared to values reported by Neville et al.,[120] as well as a comparably low Curie temperature T_C.[114] In figure 5.7 is also a deviation from the Curie-Weiss law visible. EFG substrates, grown at IKZ, show Curie-Weiss behaviour up to room-temperature and the permittivity and Cure temperature values are comparably to literature. 55

Table 5.3 Material parameter used for simulating trap-assisted FTJ. 90

C PUBLICATIONS

PUBLICATIONS

[1] Aykut Baki, Julian Stöver, Tobias Schulz, Toni Markurt, Carsten Richter, Klaus Irmscher, Martin Albrecht, and Jutta Schwarzkopf. „Stoichiometry Control for Electrical Properties of MOVPE Grown $SrTiO_3$ Thin Films." In: *Scientific Reports* under review (Oct. 27, 2020).

[2] Nazir Jaber, Julian Stöver, Johannes Feldl, Manfred Ramsteiner, Klaus Irmscher, Martin Albrech, and Jutta Schwarzkopf. „Influence of PLD Growth Temperature on the Electrical Resistivity of NbO_2 Thin Films." In: *Thin Solid Films* to be submitted in April 2021 (Apr. 1, 2021).

[3] Julian Stöver, Aykut Baki, Tobias Schulz, Jutta Schwarzkopf, Klaus Irmscher, and Martin Albrecht. „Verfahren Zum Herstellen Eines Oxidkristalls Mit Perowskitstruktur." Pat. patent pending.

[4] Julian Stoever, Jos E. Boschker, Saud Bin Anooz, Martin Schmidbauer, Peter Petrik, Jutta Schwarzkopf, Martin Albrecht, and Klaus Irmscher. „Approaching the High Intrinsic Electrical Resistivity of NbO_2 in Epitaxially Grown Films." In: *Applied Physics Letters* 116.18 (May 4, 2020), p. 182103. ISSN: 0003-6951. DOI: 10.1063/5.0005523.

[5] Julian Stöver, Aykut Baki, Tobias Schulz, Houari Amari, Toni Markurt, Carsten Richter, Jens Martin, Klaus Irmscher, Martin Albrecht, and Jutta Schwarzkopf. „Ti Antisite Defect as the Origin of Ferroelectric Resistive Switching in $SrTiO_3$." In: *Nature Materials* to be submitted in April 2021 (Apr. 1, 2020).

[6] Eldad Bahat Treidel, Oliver Hilt, Julian Stöver, Veit Hoffmann, Frank Brunner, Karina Ickert, Stefan Hochheim, Franziska Naumann, Hassan Gargouri, Bryan Martinez, Markus Weyers, and Joachim Würfl. „GaN-Based Vertical n-Channel MISFETs on Free Standing Ammonothermal GaN Substrates." In: *physica status solidi (a)* 215.8 (2018), p. 1700422. ISSN: 1862-6319. DOI: 10.1002/pssa.201700422.

CONFERENCES

[1] Julian Stöver. „Characterization of ReRam Materials." Poster (GraFOx Summer School, Menaggio, Italy). 2019.

[2] Julian Stöver, Andreas Fiedler, and Klaus Irmscher. „Deep-Level Transient Spectroscopy." Talk (GraFOx Summer School, Menaggio, Italy). 2019.

[3] Julian Stöver, Laura Bogula, Aykut Baki, Jos E. Boschker, Toni Markurt, Jutta Schwarzkopf, Martin Albrecht, and Klaus Irmscher. „Permittivity of $SrTiO_3$ in High Electric Fields and Its Temperature Dependence.“ Talk (E-MRS Fall Meeting, Warsaw, Poland). 2018.

[4] Julian Stöver, Jos E. Boschker, Nazir Jaber, Saud bin Anooz, Martin Schmidbauer, Jutta Schwarzkopf, Martin Albrecht, and Klaus Irmscher. „High Resistive NbO_2 Thin-Films for Phase-Change Switching Applications.“ talk (DPG Spring Meeting). 2020, conference cancelled.

[5] Julian Stöver, Laura Bogula, Jos E. Boschker, Toni Markurt, Jutta Schwarzkopf, Martin Albrecht, and Klaus Irmscher. „Temperature Dependence of the Permittivity in $SrTiO_3$ in High Electric Fields.“ Poster (Workshop on Dielectrics in Microelectronics, Berlin). 2018.

[6] Julian Stöver, Laura Bogula, Toni Markurt, Jos E. Boschker, Jutta Schwarzkopf, Martin Albrecht, and Klaus Irmscher. „The Electric Field Dependence of the Permittivity of $SrTiO_3$.“ Talk (DPG Spring Meeting, Dresden). 2018.

[7] Julian Stöver, Nazir Jaber, Jos E. Boschker, Saud bin Anooz, Toni Markurt, Aykut Baki, Jutta Schwarzkopf, Klaus Irmscher, and Martin Albrecht. „Pulsed Laser Deposition of Single-Crystalline NbO_2 and Its Electrical and Optical Properties.“ Poster (26th International Workshop on Oxide Electronics, Kyoto, Japan). 2019.

D | ACKNOWLEDGMENTS

I would like to start by expressing my greatest thanks to Dr. Klaus Irmscher. You always took time to discuss and explain. Your skill and knowledge of the subject, as well as your standards for good scientific work, were inspiring and extremely instructive. Discussions with you were always very insightful and helpful.

I would like to express my sincere thanks to Prof. Ted Masselink for guiding me during my doctoral studies and for reviewing the present work. I would also like to express my gratitude to Prof. Thomas Schröder. The supervisory committees and discussions during GraFOx meetings helped me to keep the goal in mind and to develop answers to open questions.

Furthermore, I would like to thank Prof. Josep Fontcuberta for being an external reviewer of the present work. I would also like to thank Prof. Christoph Koch for his willingness to serve on the examining committee and Prof. Igor Sokolov for chairing it.

Without the excellent epitaxial layers of Aykut Baki, Dr. Jos Emil Boschker, Laura Bogula and Dr. Nazir Jaber, the present work would be a blank sheet. The countless hours you spent to optimize the layers piece by piece and then also had to respond to my special requests require a special thank to you.

I would also like to thank Dr. Tobias Schulz, Dr. Toni Markurt, Dr. Martin Albrecht, Dr. Saud Bin Anooz and Dr. Houari Amari for the excellent collaboration. Your experiments helped me a lot to understand the samples and measurements in their entirety. I would also like to express my sincere gratitude to Dr. Carsten Richter for his almost inexhaustible energy to push projects forward and for the opportunity to gain experience at a synchrotron. I would like to thank Dr. Jens Martin, Peter Petric and Christo Guguchev for their collaboration.

During my time at the IKZ I had many companions. I would like to thank my office colleagues, Dr. Andreas Fiedler, Owen Ernst and Felix Lange for the countless heated discussions and the many funny and nice moments. I would like to thank my lunch group, which includes Yujia Liu, Sebastian Walde, Simon Fleischmann, David Uebel, Andreas Popp, Stefan Kayser and Palvan Seyidov, for the daily search for the "culinary highlight". I would

like to thank Dr. Torsten Böck and Prof. Dr. Matthias Bickermann for always supporting the PhD students.

I would like to thank the whole institute, especially the technical services and the workshop, for the pleasant and collaborative working atmosphere. Also I would like thank my collaborators of the Leibniz GraFOx Science campus for the nice discussions, collaborations and the great GraFOx Summer School.

Finally, I would like to thank my friends and family for accompanying and supporting me on this path.

E STATEMENT OF AUTHORSHIP / SELBSTSTÄNDIGKEITSERKLÄRUNG

Ich erkläre, dass ich die Dissertation selbständig und nur unter Verwendung der von mir gemäß § 7 Abs. 3 der Promotionsordnung der Mathematisch-Naturwissenschaftlichen Fakultät, veröffentlicht im Amtlichen Mitteilungsblatt der Humboldt-Universität zu Berlin Nr. 42/2018 am 11.07.2018 angegebenen Hilfsmittel angefertigt habe.

SUPPORTING SOFTWARE TOOLS

This work was supported by a variety of supporting software tools. Data analysis were done using `Python` as well as several python libraries, especially `Numpy`, `Scipy`, `Matplotlib`. Further data analysis and visualization was performed with `Origin Lab`, `Gwyddion`, `Vesa` and `PhysTech DLTS`. 1D Poisson simulations were done using `1D-DDCC`. Drawings were created with `Gimp` and `Inkscape`. `Atom` was used for programming. `Zotero` was used for literature management. This document was typeset using `XeLaTeX` and a adjusted version of `classicthesis`.